Strongly Stable and Accurate Numerical Integration Schemes for Nonlinear Systems in Atmospheric Models

A THESIS SUBMITTED TO THE
FACULTY OF GRADUATE AND POSTDOCTORAL STUDIES
BY

Farshid Nazari

IN PARTIAL FULFIILMENT OF THE REQUIREMENTS FOR THE DEGREE OF
DOCTOR OF PHILOSOPHY IN CIVIL ENGINEERING

uOttawa
L'Université canadienne
Canada's university

Université d'Ottawa | University of Ottawa
Département de génie civil | Department of Civil Engineering

Acknowledgements

I would like to express my sincere and deep gratitude to my supervisor, Dr. Majid Mohammadian, for his constant support, guidance, and inspiration. It is a great honour for me to know and work with Dr. Mohammadian, since he is not only a great scientist, but also a very kind, reliable, and respectful person.

I would like to thank Drs. Martin Charron and Ayrton Zadra from the Numerical Weather Prediction Research Division of Environment Canada for their valuable collaboration and helpfulness.

The invaluable suggestions and comments received from the committee members, Drs. Colin Rennie, Ioan Nistor, Samuel Li, and Amir Hakami, are highly appreciated.

This research was supported financially by Environment Canada and the Natural Sciences and Engineering Research Council (NSERC) of Canada.

I extend my warmest appreciation and love to my family, specifically my parents, for their life-long dedication and support.

To my family
and Taraneh

Abstract

Nonlinearity accompanied with stiffness in atmospheric boundary layer physical parameterizations is a well-known concern in *numerical weather prediction* (NWP) models. Nonlinear diffusion equations, furthermore, are a class of equations which are extensively applicable in different fields of science and engineering. Numerical stability and accuracy is a common concern in this class of equation.

In the present research, a comprehensive effort has been made toward the temporal integration of such equations. The main goal is to find highly stable and accurate numerical methods which can be used specifically in atmospheric boundary layer simulations in weather and climate prediction models, and extensively in other models where nonlinear differential equations play an important role, such as magnetohydrodynamics and Navier-Stokes equations.

A *modified extended backward differentiation formula* (ME BDF) scheme is adapted and proposed at the first stage of this research. Various aspects of this scheme, including stability properties, linear stability analysis, and numerical experiments, are studied with regard to applications for the time integration of commonly used nonlinear damping and diffusive systems in atmospheric boundary layer models. A new temporal filter which leads to significant improvement of numerical results is proposed.

Nonlinear damping and diffusion in the turbulent mixing of the atmospheric boundary layer is dealt with in the next stage by using optimally stable *singly-diagonally-implicit Runge-Kutta* (SDIRK) methods, which have been proved to be effective and computationally efficient for the challenges mentioned in the literature. Numerical analyses are performed, and two schemes are modified to enhance their numerical features and stability.

Three-stage third-order *diagonally-implicit Runge-Kutta* (DIRK) scheme is introduced by optimizing the error and linear stability analysis for the aforementioned nonlinear diffusive system. The new scheme is stable for a wide range of time steps and is able to resolve different diffusive systems with diagnostic turbulence closures, or prognostic ones with a diagnostic length scale, with enhanced accuracy and stability compared to current schemes. The procedure implemented in this study is quite general and can be used in other diffusive systems as well.

As an extension of this study, high-order low-dissipation low-dispersion diagonally implicit Runge-Kutta schemes are analyzed and introduced, based on the optimization of amplification and phase errors for wave propagation, and various optimized schemes can be obtained. The new scheme shows no dissipation. It is illustrated mathematically and numerically that the new scheme preserves fourth-order accuracy. The numerical applications contain the wave equation with and without a stiff nonlinear source term. This shows that different optimized schemes can be investigated for the solution of systems where physical terms with different behaviours exist.

Contents

List of Figures

List of Tables

Glossary

θ potential temperature

q specific humidity

f Coriolis parameter

g gravitational acceleration

u, v, w velocity components

u_g, v_g geostrophic wind components

$\overline{u'w'}, \overline{v'w'}$ vertical turbulent momentum fluxes

$\overline{\theta'w'}, \overline{q'w'}$ vertical turbulent heat and moisture fluxes

c_p specific heat at constant pressure for air

Ri gradient Richardson number

u_* surface friction velocity

E turbulent kinetic energy

M Prandtl frequency

N Brunt-Vaisala frequency

κ von Karman's constant

p_r reference pressure

Re Reynolds number

R radiative heat flux

T temperature

K eddy diffusivity

l mixing length

z height

ρ density

A wave amplitude

m wave number

γ wave length

1. Introduction

The *atmospheric boundary layer* (ABL) is defined as the lowest part of the atmosphere, and it is directly influenced, with a time scale of about an hour, by the earth's surface processes such as heat transfer, evaporation and transpiration, frictional drag, pollutant emission, and terrain-induced flow modifications. This turbulent layer plays an important role in the land surface climate and the exchange of heat, momentum, moisture and natural (e.g., CO_2 and other greenhouse gases) and anthropogenic (e.g., pollutant emission) contaminants from the earth's surface to the free atmosphere. In addition to daily weather forecasts, the ABL is relevant for agriculture (e.g., minimum temperatures, surface frost, dew, fog), road traffic (e.g., fog and frost), air traffic (e.g., fog, low-level jets), and wind energy engineering (Steeneveld, 2007).

Transport of variables such as heat, moisture, momentum, and pollutants is dominated in the horizontal direction by the mean wind and in the vertical by turbulence. Mean wind is responsible for the horizontal advection, where the wind speed is 100 – 1000 times greater than its vertical magnitude. On the other hand, the relatively high occurrence of turbulence near the ground, which is a distinctive characteristic of the ABL, causes the vertical diffusion (Stull, 2009).

1.1 Research Scope

Currently, and likely for the foreseeable future, boundary-layer vertical transports of heat, moisture, and momentum by turbulent eddies of unresolved scales are often parameterized using a nonlinear diffusion representation in *numerical weather prediction* (NWP) and climate models (Teixeria, 1999; Girard and Delage, 1990; Diamantakis et al., 2006). Such schemes model the effects of turbulence as a diffusive process dependent on an exchange coefficient related to wind shear and static stability. This diffusive system is a well-known nonlinear partial differential equation. Due to the rapid change in the diffusion coefficient when turbulence is intense (e.g.,

daytime convective boundary layer), the diffusive system becomes stiff. The nonlinearity and stiffness associated with the ABL modeling is the source of many subsequent numerical problems (Nazari et al., 2013 & 2014; Diamantakis et al., 2006; Teixeira, 1999; Beljaars, 1991; Girard and Delage, 1990; Kalnay and Kanamitsu, 1988).

1.2 Research Significance

Numerical integrations of the above nonlinear systems in *numerical weather prediction* (NWP) and climate models need to be at least partially implicit; otherwise, impractically short time steps have to be used. This is due to the thinness of the layers typically required to account for the large flux gradients near the earth's surface. However, because the exchange coefficients are often nonlinearly dependent on the atmospheric state (and vary in space and time due to changing boundary layer characteristics), even partially implicit numerical schemes have limitations which can lead to oscillatory behaviour or instability (Diamantakis et al., 2006). With the increasing use of semi-implicit time schemes and semi-Lagrangian advection in models, even longer time steps are being used. This increases the likelihood of either oscillatory behaviour or instability associated with the boundary layer time scheme (Williamson, 1995, Diamantakis et al., 2006), and such behaviour is observed in both NWP and climate runs of the Canadian Global Environmental Multi-scale (GEM) and Meso-scale Compressible Community (MC2) models. In practice, the problem may cause a difference of 4 – 5 degrees between the predicted temperature and the actual one.

1.3 Research Objective

In this thesis, the focus is on temporal integration of nonlinear equations in the ABL, and extensively in atmospheric models. The final goal is to introduce strongly stable and highly accurate time integration schemes for such equations in order to be applied in NWP models and thus, improve weather predictions reliability.

The objective in Chapter 4 is to analyze the performance of a *modified* EBDF (ME BDF) scheme in the form of SDIRK schemes for nonlinear diffusion equations, with a

focus on the atmospheric boundary layer simulations as an application. The scheme will be adapted in this chapter in order to obtain a scheme which is highly stable and fairly accurate when there is a high degree of nonlinearity. The proposed scheme should use a semi-implicit approach which is computationally efficient to deal with nonlinear diffusion coefficients. Low sensitivity of the results to spatial and temporal resolution is another property of the proposed scheme the author is seeking for, which is very important, for instance, in studying atmospheric boundary layer properties.

The next chapter (Chapter 5) focuses on the performance of a class of Runge-Kutta methods which possess strong stability characteristics for the solution of nonlinear ordinary and partial differential equations. Optimal SDIRK methods of up to three stages will be studied and analyzed for the solution of nonlinear ordinary differential damping equations representing surface heat or moisture transfer, as well as nonlinear partial differential diffusion equations for velocity and temperature in the ABL.

In Chapter 6, an optimal multi-stage high-order DIRK scheme will be investigated for the solution of a typical nonlinear diffusive system in the ABL. The objective is to obtain a higher-order method which possesses the strengths of the previously proposed ME BDF scheme in Chapter 4 and can preferably gain an improvement in performance for high spatial resolutions and large time steps in comparison with available schemes, while retaining a comparable accuracy for low spatial resolutions. The final goal is to find and apply a new scheme on more realistic studies of the diffusive systems in the planetary boundary layer model, which is used in fully three-dimensional models such as the Canadian Global Environmental Multi-scale (GEM) and Meso-scale Compressible Community (MC2) models.

In Chapter 7, the study will be expanded to find a fourth-order low-dissipative low-dispersive three-stage DIRK scheme through optimized dissipation and dispersion. The selected scheme, along with the *implicit low-dissipation low-dispersion Runge-Kutta* (ILDDRK4) scheme and fourth-order three-stage SDIRK (SDIRK4) scheme, will be compared in terms of dissipation and dispersion and tested for the numerical approximation of systems of conservation laws with stiff nonlinear source terms, which are very common in CFD.

1.4 Thesis Outline

At the first step of this research, a *modified extended backward differentiation formula* (ME BDF) scheme in the form of a multi-stage Runge-Kutta (RK) scheme was investigated according to our knowledge regarding the nature of oscillations in ABL problems. The author found that by adding a temporal filter to the scheme, one is able to obtain highly stable and accurate solutions for specific equations of the ABL. This led to our first publication in the Journal of Computational Physics (Chapter 4). For further investigation of the temporal schemes currently used for stiff equations, the author continued to study optimally strongly stable (monotonic) *singly-diagonally-implicit* RK (SDIRK) schemes in the literature (see e.g., Ferracina and Spijker, 2008). It is shown that these schemes could not address our needs properly, so following the first experience the author tried to enhance the performance of such schemes by modifying them to ME BDF schemes (our publication in International Journal for Numerical Methods in Engineering [Chapter 5]). To this point, the proposed schemes were still first-order formally according to the RK order conditions (see Chapter 6 or Butcher, 2008 for more details). In order to enhance the accuracy while preserving stability, the author looked, through an optimization process, for a higher-order scheme which has similar stability properties to the previously proposed ME BDF scheme. This resulted in our second publication in the Journal of Computational Physics (Chapter 6). After the efforts to find a suitable scheme for the ABL nonlinear diffusion, in our next publication in the Journal of Computational Physics (Chapter 7) the author moved toward finding a high-order low-dissipation low-dispersion scheme. Such schemes are valuable for the solution of various equations, including wave equations (e.g., advection). This could be useful for further investigation into the application of optimized schemes to advection-diffusion combinations, e.g., in NWP models.

2. Theoretical Background

The ABL is generally turbulent, so the equations describing boundary layer behaviour consist of mean and fluctuating quantities. However, averaging the equations leads to a situation where the unknowns are more than equations; the so-called closure problem. The basic equations of flow and the evolution of mean and turbulent quantities are described first in this chapter. The set of equations forms the basis of any numerical model of the atmosphere. The governing equations for the mean and fluctuating quantities of wind velocity u, potential temperature θ, and humidity, and the simplified form of the mean equations in common use in the atmospheric boundary layer are explained. The challenge of turbulence closure may lead to consideration of the second-moment equations, with particular attention to the *turbulent kinetic energy* (TKE) equation and the introduction of the thermal stability (buoyancy) parameters. Some types of turbulence parameterizations that have been presented in the literature are reviewed. This review is not comprehensive and is meant only to introduce and explain in brief some turbulence closures which may be used in the ABL modeling.

The remainder of this chapter is an overview of the present literature about the numerical concerns and studies of ABL modeling along with related studies of the numerical methods for the solution of nonlinear ordinary and partial differential equations.

2.1 The Thermodynamic Equation: Conservation of Enthalpy

The conservation of enthalpy (or sensible heat) per unit mass, $c_{\mathrm{p}}\theta$, is derived from the first law of thermodynamics. The resulting equation for θ can be written as (Businger, 1982)

$$\frac{d(c_p\theta)}{dt} = \kappa_T \frac{\partial^2(c_p\theta)}{\partial x_j^2} + \rho^{-1}\frac{\partial R_j}{\partial x_j} \tag{2.1}$$

Here, R_j is the radiative heat flux, c_p is the specific heat at constant pressure for air, and κ_T is the molecular thermal diffusivity. Note that $\theta = T\left(\frac{p_r}{p}\right)^{R/c_p}$ in which T is the temperature and p_r is the reference pressure. This equation suggests that in the absence of any phase change and of radiative transfer, θ (since c_p can be taken as a constant) can be considered as a conservative property of the air.

Applying a Reynolds decomposition on the θ equation results in

$$\frac{\partial \bar{\theta}}{\partial t} + \bar{u}_j \frac{\partial \bar{\theta}}{\partial x_j} = -\frac{\partial (\overline{u_j' \theta'})}{\partial x_j} + \kappa_T \frac{\partial^2 \bar{\theta}}{\partial x_j^2} + (\rho c_p)^{-1} \frac{\partial \bar{R}_j}{\partial x_j} \tag{2.2}$$

, with terms such as $\bar{u}_j \frac{\partial \overline{\theta'}}{\partial x_j}$ and $\overline{\theta' \frac{\partial u_j'}{\partial x_j}}$ vanishing. Heat transport by the turbulence appears as the first term on the right-hand side.

2.2 The Humidity Equation: Conservation of Water Vapour

When no phase change occurs, conservation of water vapour can be written as

$$\frac{dq}{dt} = \kappa_V \frac{\partial^2 q}{\partial x_j^2} \tag{2.3}$$

, where q is the specific humidity. Water vapour is a conservative scalar quantity in the absence of phase transitions in the ABL. Similar to the θ decomposition, the mean q equation is

$$\frac{\partial \bar{q}}{\partial t} + \bar{u}_j \frac{\partial \bar{q}}{\partial x_j} = -\frac{\partial (\overline{u_j' q'})}{\partial x_j} + \kappa_V \frac{\partial^2 \bar{q}}{\partial x_j^2} \tag{2.4}$$

2.3 The Navier-Stokes Equations: Conservation of Momentum

The Navier-Stokes equations in a conservative form can be written in the form

$$\frac{du_i}{dt} = -\rho^{-1}\frac{\partial p}{\partial x_i} + \nu\nabla^2 u_i + F_i \tag{2.5}$$

, where F_i represents all external forces. Considering a constant viscosity along with the earth's rotation, the Navier-Stokes equation for the ABL in the incompressible form will be

$$\frac{du_i}{dt} = -\rho^{-1}\frac{\partial p}{\partial x_i} + \nu\nabla^2 u_i - g\delta_{i3} + f u_i \tag{2.6}$$

This equation gives the acceleration of the air in terms of several forces. The first term on the right-hand side represents the pressure gradient force. The second term stands for the viscous stresses. The third term reflects the effect of gravity. The last term describes the effect of the earth's rotation in the form of Coriolis forces. The Coriolis parameter is $= 2\Omega\sin\phi$, in which Ω is the angular velocity of the earth's rotation with the value of 7.29×10^{-5} rad s^{-1}, and ϕ is the latitude. f is positive in the northern hemisphere and negative in the southern.

Setting $u_i = \bar{u}_i + u_i'$ for the Reynolds decomposition leads to the mean velocity equation (the conservation of mean momentum) as

$$\frac{\partial \overline{u_\iota}}{\partial t} + \bar{u}_j\frac{\partial \overline{u_\iota}}{\partial x_j} = -\frac{\partial(\overline{u_j' u_\iota'})}{\partial x_j} - \rho^{-1}\frac{\partial \bar{p}}{\partial x_i} + \nu\frac{\partial^2 \overline{u_\iota}}{\partial x_j^2} - g\delta_{i3} + f\bar{u}_i \tag{2.7}$$

For the vertical velocity component, the terms $\frac{\partial \bar{p}}{\partial z}$ and ρg are dominant in the absence of strong vertical accelerations (Pielke, 2013). Assuming that the mean state is hydrostatic equilibrium, then

$$\frac{\partial \bar{p}}{\partial z} = -\rho g \tag{2.8}$$

This equation is also referred to as the *hydrostatic equation*, and is a reasonable representation of the mean pressure in the vertical direction, even under strongly turbulent conditions (e.g., in the daytime convective boundary layer or with a strong wind condition).

2.4 The Simplified Mean Equations

The terms $\frac{\partial(\overline{u_j'\theta'})}{\partial x_j}$, $\frac{\partial(\overline{u_j'q'})}{\partial x_j}$, and $\frac{\partial(\overline{u_j'u_i'})}{\partial x_j}$ arise in Eqs. (2.2), (2.4), and (2.7) for the mean quantities, respectively. These terms are called *fluxes*, in analogy with molecular transport (Garratt, 1994), so that $\overline{u_j'\theta'}$ represents the turbulent heat flux, $\overline{u_j'q'}$ represents the turbulent moisture flux, and $\overline{u_j'u_i'}$ represents the turbulent momentum flux or *Reynolds stresses*. These flux divergences act as source terms to change the mean concentrations. They are a direct result of the nonlinearity included in the terms $u_j \frac{\partial u_i}{\partial x_j}$, $u_j \frac{\partial \theta}{\partial x_j}$, and $u_j \frac{\partial q}{\partial x_j}$ appearing in the equations for the instantaneous quantities. The turbulent fluxes imply that the velocity, temperature, and humidity fluctuations are responsible for the transport of momentum, heat, and water vapour in a fluid across a surface, which illuminates the fundamental importance of the turbulent fluxes in air flow phenomena within the ABL.

Due to high Reynolds numbers (typically $Re \sim 10^7$) in the ABL, the turbulent terms in the conservation equations for mean variables are orders of magnitude greater than the molecular terms. For instance, in Eq. (2.7) for mean momentum, the viscous term can be written in scaled form as $Re^{-1}\left(v_s l_s \frac{\partial^2 \overline{u_i}}{\partial x_j^2}\right)$, where $Re = \frac{v_s l_s}{\nu}$. The term in the brackets is of the same order of magnitude as all the other terms in Eq. (2.7), so the viscous term with the factor of Re^{-1} is negligible.

As a result, the mean equations for the horizontally homogeneous ABL can be simplified to

$$\frac{\partial \bar{u}}{\partial t} = -\rho^{-1}\frac{\partial \bar{p}}{\partial x} + f\bar{v} - \frac{\partial(\overline{u'w'})}{\partial z} \tag{2.9}$$

$$\frac{\partial \bar{v}}{\partial t} = -\rho^{-1}\frac{\partial \bar{p}}{\partial y} - f\bar{u} - \frac{\partial(\overline{v'w'})}{\partial z} \tag{2.10}$$

$$\frac{\partial \bar{\theta}}{\partial t} = (\rho c_p)^{-1}\frac{\partial \bar{R}_N}{\partial z} - \frac{\partial(\overline{\theta'w'})}{\partial z} \tag{2.11}$$

$$\frac{\partial \bar{q}}{\partial t} = -\frac{\partial(\overline{q'w'})}{\partial z} \tag{2.12}$$

as a 1-D model. Above the ABL, the turbulence disappears and the flow can be considered as steady-state. Momentum Eqs. (2.9) and (2.10) are thus a simple two-force balance between the Coriolis and pressure gradient terms, and can be written as:

$$0 = -\rho^{-1}\frac{\partial \bar{p}}{\partial x} + f\overline{v_g} \tag{2.13}$$

$$0 = -\rho^{-1}\frac{\partial \bar{p}}{\partial y} - f\overline{u_g} \tag{2.14}$$

u_g and v_g are *geostrophic wind* components. Consequently, Eqs. (2.9) and (2.10) can be simplified to:

$$\frac{\partial \bar{u}}{\partial t} = f(\bar{v} - \overline{v_g}) - \frac{\partial(\overline{u'w'})}{\partial z} \tag{2.15}$$

$$\frac{\partial \bar{v}}{\partial t} = -f(\bar{u} - \overline{u_g}) - \frac{\partial(\overline{v'w'})}{\partial z} \tag{2.16}$$

, with the mean *ageostrophic wind* components $\bar{u} - \overline{u_g}$ and $\bar{v} - \overline{v_g}$. This proves that the mean ageostrophic winds in the one-dimensional steady-state ABL are the result of Reynolds stress vertical gradients. The simplified mean equations in this section are the basic equations used in our study of the ABL in the following chapters.

2.5 Turbulence Closure Schemes

As demonstrated in the previous section, the turbulent terms are added to the number of unknowns in the conservation equations. This is a continual problem in turbulence, where introducing more equations to solve the arising unknowns again results in new unknowns. This is called the *closure problem* in turbulence studies, which is associated with turbulence's nonlinear characteristic.

Closure approximations (local) relate the unknowns in a set of equations to the known quantities. The closure approximation is named after the highest-order moment retained in the equations. They start from zero-order and are extended to third-order schemes, but in this section a brief introduction to first- and one-and-a-half-order closure schemes is presented, as these are the commonly used models in ABL simulations, which is also the case in the following chapters.

2.5.1 First order

First-order closure retains the prognostic equations only for the mean quantities. As an example, an idealized case of a dry, horizontally homogeneous ABL consists of the simplified momentum Eqs. (2.15) and (2.16) accompanied by the temperature Eq. (2.11), which includes only the turbulent heat flux on the right-hand side. The unknowns in this set of equations are second-order moments: $\overline{u'w'}$, $\overline{v'w'}$, and $\overline{\theta'w'}$. In the first-order closures, the turbulent fluxes are related to the local mean gradient of the quantity being transferred through eddy transfer coefficients or diffusivities, K, in

analogy with laminar flows. Thus, the turbulent fluxes for any variable s can be written in terms of mean flux gradient as:

$$\overline{u_j' s'} = -K \frac{\partial \bar{s}}{\partial x_j} \tag{2.17}$$

K diffusivities ($m^2\ s^{-1}$) can have different values for different variables. The K unit implies that it can be a product of a turbulent velocity scale and an appropriate length scale such as the dominant eddy size. Various parameterizations have been proposed in the literature for the eddy diffusivity coefficients. The first-order closure K parameterization used in the following chapters is in the form:

$$K = l^2 \left| \frac{\partial \mathbf{V}}{\partial z} \right| f_s(Ri) \tag{2.18}$$

, where l is the mixing length and Ri is the Richardson number:

$$Ri = \frac{g}{\theta_0} \frac{\partial \theta / \partial z}{(\partial u / \partial z)^2} \tag{2.19}$$

, where g is the gravity acceleration and θ_0 is a constant. The mixing length is also variable with the elevation, and can be obtained through different parameterizations. This approach for K arises from consideration of the TKE balance between local dissipation and production (shear and buoyancy), with suitable scaling of the terms (Garratt, 1994).

Note that static stability corresponds to $Ri > 0$, and vice versa for static instability. There are numerous semi-empirical formulae for $f_s(Ri)$. A common one, which is also used in the following chapters, reads:

$$f_s(Ri) = (1 + b|Ri|)^n \tag{2.20}$$

As the static stability increases, K should gradually vanish, while it grows as static instability intensifies. To model this behaviour, n and b must vary according to stability, and only one of them must change sign when the Ri sign changes. The values of n and b are thus considered as:

$$\begin{aligned} n = -2; b = 5 \quad for\ Ri > 0 \\ n = \frac{1}{2}; b = 20 \quad for\ Ri < 0 \end{aligned} \tag{2.21}$$

2.5.2 One-and-a-half order

One-and-a-half-order closures retain the first-order closure prognostic equations, which may include the equations for the mean quantities of wind, temperature, and humidity, plus the TKE equation, which includes the variances of the mean variables.

As an illustration, similar to the first-order closure, a one-dimensional, horizontally homogeneous, dry boundary layer is considered. The governing equations thus consist of the first-order closure equations (simplified momentum Eqs. (2.15) and (2.16) accompanied by the temperature Eq. (2.11), which includes only the turbulent heat flux on the right-hand side) and the TKE equation. Hence, the K diffusivity approach mentioned in Eq. (2.17) leads to the following set of equations for the one-and-a-half-order closure scheme:

$$\frac{\partial u}{\partial t} = \frac{\partial}{\partial z}\left(K_m \frac{\partial u}{\partial z}\right) + f(v - v_g) \tag{2.22}$$

$$\frac{\partial v}{\partial t} = \frac{\partial}{\partial z}\left(K_m \frac{\partial v}{\partial z}\right) - f(u - u_g) \tag{2.23}$$

$$\frac{\partial \theta}{\partial t} = \frac{\partial}{\partial z}\left(K_h \frac{\partial \theta}{\partial z}\right) \tag{2.24}$$

$$\frac{\partial E}{\partial t} = \frac{\partial}{\partial z}\left(K_e \frac{\partial e}{\partial z}\right) + K_m \left[\left(\frac{\partial u}{\partial z}\right)^2 + \left(\frac{\partial v}{\partial z}\right)^2\right] - \left(\frac{g}{\theta_0}\right) K_h \frac{\partial \theta}{\partial z} - \varepsilon \tag{2.25}$$

, where K_m, K_h, and K_e are the momentum, heat, and TKE (E) eddy diffusivities, respectively. ε is the dissipation rate which is approximated based on scaling arguments consistent with the TKE balance in the neutral boundary layer. Some well-known parameterizations are suggested by Mellor and Yamada (1974) for the eddy diffusivities and dissipation rate in terms of the turbulent length scale. A complete one-and-a-half-order turbulence closure scheme, including the corresponding parameterizations, can be found in Chapters 6 and 7.

2.6 Numerical Integration Schemes

The following *ordinary differential equation* (ODE) initial value problem is considered in order to introduce a multi-stage Runge-Kutta scheme in a simplified abstract setting:

$$\dot{y}(t) = f(t, y), \quad y(t_0) = y_0 \tag{2.26}$$

The general Runge-Kutta method, applied to problem (2.26), can provide us with numerical approximations y_{n+1} at the new time step where n = 1, 2, 3, etc.; see e.g., Butcher (1987, 2008), Hairer et al. (1987), Hundsdorfer and Verwer (2003). An s-stage partitioned Runge-Kutta method is characterized by the Butcher tableau and describes one step of the solution ($y_{old} \rightarrow y_{new}$), as follows. The Butcher tableau

c	**A**
	$\mathbf{b^T}$

(2.27)

includes the coefficients of s-stage Runge-Kutta methods, where $\mathbf{b^T} = [b_1, ..., b_s]$, $\mathbf{A}=[a_{ij}]$ (i, j= 1, ..., s) are real numbers and $c_i = \sum_j a_{ij}$ in **c** for a physically justified scheme. The

solution at the new time step n+1 for an s-stage Runge-Kutta method is then obtained by:

$$y_{n+1} = y_n + h\sum_{i=1}^{s} b_i k_i \tag{2.28}$$

, where

$$k_i = f(t_n + c_i h, y_n + h\sum_{j=1}^{s} a_{ij} k_j) \tag{2.29}$$

, with step size h.

This study focuses on the performance of a class of Runge-Kutta methods which possess specific nonlinear stability characteristics distinguished by the terms *strongly stable* or *monotonic*. The numerical applications may consist of commonly used ground-air heat/moisture exchange and wind/potential temperature diffusion processes. A scheme is defined to be strongly stable or monotonic when it satisfies the condition:

$$\|y_{n+1}\| \leq \|y_n\| \tag{2.30}$$

in the progression from the time step n to n+1 in the numerical integration of the ODE initial value problem (2.26).

Specifically, the property (2.30) is of particular prominence for the solution of nonlinear parabolic partial differential equations such as the diffusion equation, as a semi-discretized parabolic equation gets the form of Eq. (2.26); monotonic numerical methods are considered a powerful tool for the solution of these challenging problems; see e.g., Shu and Osher (1988), LeVeque (2002), and Higueras (2005). Strong stability of the numerical time integrator in a partial differential equation has been proved to be essential to prevent spurious oscillations caused by spatial discretization (Gottlieb et al., 2009).

Some studies have been performed on multi-stage higher-order methods, such as Gourlay and Morris (1981) and Cash (1984). However, fully implicit schemes are computationally expensive and not practical in atmospheric boundary layer simulations. *Diagonally-implicit Runge-Kutta* (DIRK) methods possess the advantages of implicitness while being computationally efficient in comparison with fully coupled multi-stage implicit methods. In other words, stages in DIRK methods can be solved sequentially, which brings about computational efficiency (Nazari et al., 2013). DIRK schemes are explained more in the following chapters.

3. Literature Review

A well-known concern in ABL prediction models is the nonlinearity accompanied with stiffness involved in the diffusion equation, which requires very small time steps in explicit schemes and makes the use of fully implicit methods impractical. Although prognostic approaches are common in ABL modeling, there is still a wide variety of applications for diagnostic approaches where the diffusion coefficients are typically related to the stability (Richardson number) via nonlinear equations (see e.g., Eq. (2.18)). The diffusion coefficients can be relatively large in comparison with the time step and vertical grid space regularly used in climate and NWP models, and they often exceed the numerical stability limits for explicit schemes (Siebesma et al., 2007). As an example, NOGAPS (*Navy Operational Global Atmospheric Prediction System*) is a complex model that includes a full set of physical parameterizations to represent sub-grid scale physical processes such as radiation, turbulence, clouds, and moist convection. Nonlinearities introduced by these parameterizations can cause several specific numerical problems; in particular, for parameter values (e.g., eddy-diffusivity coefficient and mass-flux coefficient) and time steps typically used in operational NWP centers, spurious numerical oscillations may occur in some variables (Teixeira et al., 2007). Consequently, various semi-implicit schemes have been introduced and studied in terms of stability, accuracy, and efficiency to solve nonlinear diffusion or damping equations in the atmospheric boundary layers (Kalnay and Kanamitsu, 1988; Girard and Delage, 1990; Teixeira, 1999; Wood et al., 2007). A stable and accurate numerical method for diffusion equations is also very useful for unified models in which the same dynamical core is used for both operational weather predictions and long-term climate simulations (Staniforth and Wood, 2008). On the other hand, there is a wide range of applicability for nonlinear diffusion equations, from engineering flows (Oran and Boris, 1987) and magnetohydrodynamics (Potter, 1973) to insect dispersal (Murray, 1993), and numerical stability is a general concern associated with them (Teixeira, 1999). A scheme with better stability and accuracy can thus be of great interest for all those applications.

The spatial and temporal distributions of velocity and temperature are typically obtained by solving a set of coupled diffusion equations, as illustrated in Section 2.4. It is known that under statically stable conditions, the traditional implicit scheme is not unconditionally stable, and linear numerical instability occurs in the form of large bounded spurious oscillations [Girard and Delage, 1990]. This problem has also been observed in the study of a ground temperature model [Kalnay and Kanamitsu, 1988; Diamantakis et al., 2006]. To prevent these problems, the time step in the solution of nonlinear diffusive systems cannot be increased significantly, which leads to prohibitive computational costs.

Several articles exist in the literature regarding explicit and implicit Runge-Kutta methods for solving ordinary (e.g., Ixaru, 2012) and partial (e.g., Verwer, 1996) differential equations. Some studies have also been performed on multi-stage higher-order methods, such as Gourlay and Morris (1981) and Cash (1984). However, fully implicit schemes are computationally expensive and not practical in atmospheric boundary layer simulations. On the other hand, a class of *extended backward differentiation formulae* (EBDF) was introduced by Cash (1980) for the integration of stiff ordinary differential equations, which was later modified (Cash, 1983) to enhance the stability properties and reduce computational efforts.

Strong stability property (2.30) is of particular prominence for the solution of nonlinear parabolic partial differential equations such as the diffusion equation, as semi-discretized parabolic equation gets the form of Eq. (2.26); monotonic numerical methods are considered as a powerful tool for the solution of these challenging problems; see e.g. Shu and Osher (1988), LeVeque (2002), Higueras (2005). Strong stability of the numerical time integrator has been proved to be essential to prevent spurious oscillations caused by the spatial discretization in a partial differential equation (Gottlieb et al., 2009).

Diagonally-implicit Runge-Kutta (DIRK) methods possess the advantages of implicitness while they are computationally efficient in comparison with fully coupled multi-stage implicit methods. In other words, each stage in DIRK methods can be solved independently, which brings about computational efficiency (Nazari et al., 2013). Optimally monotonic SDIRK (*singly DIRK*) schemes have been studied by

Ferracina and Spijker (2007) with certain stages and orders of accuracy in order to preserve the strong stability property of the schemes for as large a time step as possible.

Furthermore, in wave propagation and computational acoustics, both dissipation and dispersion errors are of great concern and preserving the stability limits do not suffice to obtain desirable results (Hu et al., 1996). As a result, low-dissipative low-dispersive integration schemes have drawn attention in the simulation of these physical phenomena. Spatial discretization techniques have first been under considerable investigation to have low-dissipation and low-dispersion errors. Some related studies consist of explicit DRP (Tam and Webb, 1993), compact (implicit) finite differences (Lele, 1992), and ENO schemes (Casper et al. 1994). Some efforts have also been done to introduce low-dissipative low-dispersive temporal integration schemes. Due to the benefits of Runge-Kutta schemes, Hu et al. (1996) developed low-dispersion and low-dissipation Runge–Kutta (LDDRK) schemes through the minimization of dissipation and dispersion errors. Optimized second-order single-step four-, five- and six-stage Runge-Kutta schemes in addition to optimized two-step schemes with different coefficients for the alternating steps were introduced. For the two-step methods and only six-stage single-step method, they could reach fourth-order accuracy. The study of low-dissipation low-dispersion schemes were then continued e.g. by Bogey and Bailly (2004) (second-order explicit multi-stage Runge-Kutta schemes) extended later by Berland et al. (2006) to introduce a low-storage, fourth-order accurate optimal scheme, or Stanescu and Habashi (1998) (fourth-order weakly stable six-stage explicit scheme).

As is clear, all of the mentioned studies are related to explicit schemes. However, explicit schemes are well-known for the numerical stability concerns. To avoid instability, very small time steps may be required in some applications such as solid boundaries in flow field, which leads to high computational costs.

4. A Stable and Accurate Scheme for Nonlinear Diffusion Equations: Application to Atmospheric Boundary Layer[1]

Abstract

Stability concerns are always a factor in the numerical solution of nonlinear diffusion equations, which are a class of equations widely applicable in different fields of science and engineering. In this study, a modified extended backward differentiation formulae (ME BDF) scheme is adapted for the solution of nonlinear diffusion equations, with a special focus on the atmospheric boundary layer diffusion process. The scheme is first implemented and examined for a widely used nonlinear ordinary differential equation, and then extended to a system of two nonlinear diffusion equations. A new temporal filter which leads to significant improvement of numerical results is proposed, and the impact of the filter on the stability and accuracy of the results is investigated. Noteworthy improvements are obtained as compared to other commonly used numerical schemes. Linear stability analysis of the proposed scheme is performed for both systems, and analytical stability limits are presented.

Keywords: Diffusion equation; Numerical stability; Non-linear diffusion; Multi-stage integration; Atmospheric boundary layer; Stiff equations.

4.1 Introduction

A well-known concern in the ABL (Atmospheric Boundary Layer) prediction models is the nonlinearity involved in the diffusion equation accompanied with stiffness, which leads to very small time steps in explicit schemes and makes the use of fully implicit methods impractical. Although prognostic approaches are common in the ABL modeling, there is still a wide variety of applications for diagnostic approaches,

[1] This chapter has been published as Farshid Nazari, Abdolmajid Mohammadian, Ayrton Zadra, and Martin Charron, "A Stable and Accurate Scheme for Nonlinear Diffusion Equations: Application to Atmospheric Boundary Layer", Journal of **Computational Physics** 236 (2013) 271-288 http://dx.doi.org/10.1016/j.jcp.2012.10.039.

where the diffusion coefficients are typically related to the stability (Richardson number) via nonlinear equations. The diffusion coefficients can be relatively large in comparison with the time step and vertical grid space regularly used in climate and NWP (Numerical Weather Prediction) models, and they often exceed the numerical stability limits for explicit schemes (Siebesma et al., 2007). Janiskova et al. (1999) developed a simplified physical parameterization package containing the same vertical turbulent diffusion model as the one studied in this paper for inclusion in an incremental four-dimensional variational assimilation. They evaluated this package in the global ARPEGE (Action de Recherche Petite Echelle Grande Echelle) model. Furthermore, NOGAPS (Navy Operational Global Atmospheric Prediction System) is a complex model that includes a full set of physical parameterizations to represent sub-grid scale physical processes such as radiation, turbulence, clouds, and moist convection. Nonlinearities introduced by these parameterizations can cause several specific numerical problems; in particular, for parameter values (e.g. eddy-diffusivity coefficient and mass-flux coefficient) and time steps typically used in operational NWP centers, spurious numerical oscillations may occur in some variables (Teixeira et al., 2007). Consequently, various semi-implicit schemes have been introduced and studied in terms of stability, accuracy, and efficiency to solve nonlinear diffusion or damping equations in atmospheric boundary layers (Kalnay and Kanamitsu, 1988: KK88 hereafter; Girard and Delage, 1990: GD90 hereafter). A stable and accurate numerical method for diffusion equations is also very useful for unified models in which the same dynamical core is used for both operational weather predictions and long-term climate simulations (Staniforth and Wood, 2008). On the other hand, there is a wide range of applicability for nonlinear diffusion equations, from engineering flows (Oran and Boris, 1987) and magnetohydrodynamics (Potter, 1973) to insect dispersal (Murray, 1993), and numerical stability is a general concern associated with them (Teixeira, 1999). A scheme with better stability and accuracy can thus be of great interest for all those applications.

The spatial and temporal distributions of velocity and temperature are typically obtained by solving a set of coupled diffusion equations. GD90 proposed two versions of semi-implicit schemes using a well-known parameterization for the diffusion

coefficient in numerical weather prediction (NWP) in order to solve the diffusion equation. They showed that under statically stable conditions, the traditional implicit scheme is not unconditionally stable, and linear numerical instability occurs in the form of large bounded spurious oscillations. This problem has also been observed by KK88 in their study of a ground temperature model.

A widely accepted nonlinear ODE (Ordinary Differential Equation) form of ground surface temperature simulation (surface heat flux) in ABL modeling was studied by KK88, who used a number of numerical schemes to study stability and accuracy problems associated with the selected numerical schemes. They obtained stable and accurate results using a traditional semi-implicit scheme which applies a time filter for higher temperature values (the unstable region).

Wood et al. (2007) examined a two-time-level scheme for the KK88 nonlinear damping equation and then extended their scheme for linear and nonlinear diffusion equations. For the nonlinear case, they used the simple nonlinear form of the KK88 diffusion coefficient. An adapted spatial discretization was proposed by Teixeira (1999) to reach an unconditionally stable scheme for solving the diffusion equation. That study mainly discussed the stability of linear diffusion equations with an application for the GD90 nonlinear atmospheric diffusion equation.

Some studies have also been performed on multi-stage higher-order methods, such as Gourlay and Morris (1981) and Cash (1984). However, fully implicit schemes are computationally expensive and not practical in atmospheric boundary layer simulations.

Several articles exist in the literature regarding explicit and implicit Runge-Kutta methods for solving ordinary (e.g. Ixaru, 2011) and partial (e.g. Verwer, 1996) differential equations. On the other hand, a class of EBDF (Extended Backward Differentiation Formulae) was introduced by Cash (1980) for the integration of stiff ordinary differential equations, which was later modified (Cash, 1983) to enhance the stability properties and reduce the computational efforts.

The objective of this paper is to analyse the performance of a ME BDF (Modified Extended Backward Differentiation Formulae) scheme in the form of singly diagonally implicit Runge-Kutta (SDIRK) schemes for nonlinear diffusion equations, with a focus

on atmospheric boundary layer simulations as an application. The scheme is adapted and proposed in this study in order to obtain a scheme which is highly stable and fairly accurate for high degree of nonlinearity. The proposed scheme uses a semi-implicit approach, which is computationally efficient, to deal with nonlinear diffusion coefficients. Low sensitivity of the results to spatial and temporal resolution is another property of the proposed scheme we are seeking, which is very important, for instance, in studying atmospheric boundary layer properties.

This paper is organized as follows. The proposed scheme is first explained in the general form in Section 4.2. It is then implemented in Section 4.3 for a strongly nonlinear ordinary differential equation proposed in KK88. In Section 4.4, the scheme is implemented for a system of nonlinear diffusion equations using the non-constant diffusion coefficient used by GD90. Both of these sections include linear stability analysis of the scheme, applied to the corresponding equation, as well as numerical experiments to evaluate the performance of the proposed method. Some concluding remarks complete the study.

4.2 The Proposed Scheme

To introduce the proposed scheme in a simplified abstract setting, we consider the following ODE initial value problem

$$\dot{y}(t) = f(t, y), \quad y(t_0) = y_0 \tag{4.1}$$

An *s*-stage partitioned Runge-Kutta method is characterized by the Butcher tableau and describes one step of the solution ($y_{old} \rightarrow y_{new}$), as follows.

The Butcher tableau

$$\begin{array}{c|ccc} c_1 & a_{11} & \dots & a_{1s} \\ \vdots & \vdots & & \vdots \\ c_s & a_{s1} & \dots & a_{ss} \\ \hline & b_1 & \dots & b_s \end{array} \tag{4.2}$$

includes the coefficients of s-stage Runge-Kutta methods where b_1, ..., b_s, a_{ij} (i, j = 1, ..., s) are real numbers and $c_i = \sum_j a_{ij}$. The solution at the new time step n+1 for an s-stage Runge-Kutta method is obtained by

$$y_{n+1} = y_n + h \sum_{i=1}^{s} b_i k_i \tag{4.3}$$

where

$$k_i = f(t_n + c_i h, y_n + h \sum_{j=1}^{s} a_{ij} k_j) \tag{4.4}$$

with step size h.

The proposed scheme here, originally defined by the following Butcher tableau, is in fact a combination of a singly diagonally implicit Runge-Kutta (SDIRK) and a modified extended backward differentiation formula (ME BDF). The advantage of SDIRK methods is that they are computationally more efficient than the general implicit Runge-Kutta methods. The computational efficiency arises from the fact that each stage can be computed independently as opposed to fully coupled stages of general implicit RK methods. Also the Butcher tableau implies a simple matrix A=[a_{ij}], where the linear system associated with the stage equations may be solved exactly, due to its lower triangular structure (e.g. as in LU decompositions). As will be shown in Section 4.4, this scheme (SDIRK), using proper spatial discretizations, leads to tridiagonal systems.

1	1	0	0
2	1	1	0
1	1/2	-1/2	1
	1/2	-1/2	1

(4.5)

However, as will be shown in the following, it is not a desired scheme for solving the nonlinear systems in this study. Thus, a modification is introduced by the authors which reforms the proposed scheme as

1	1	0	0
2	1	1	0
1	1/2	-1/2	1
	5/8	1/8	1/4

(4.6)

This modification comes from a temporal filter implemented in the last stage in order to improve the stability of the scheme and reduce oscillations. To illuminate how the temporal filter leads to the Butcher tableau above, we expand the scheme and look at the details.

According to the tableau of the proposed scheme (4.6)

$$\begin{aligned} Y_1 &= y_n + hk_1 \\ k_1 &= \frac{Y_1 - y_n}{h} \end{aligned} \tag{4.7}$$

where Y_s represents Y in stage s.

$$\begin{aligned} Y_2 &= y_n + h(k_1 + k_2) \\ k_2 &= \frac{Y_2 - Y_1}{h} \end{aligned} \tag{4.8}$$

$$\begin{aligned} Y_3 &= y_n + h(\frac{1}{2}k_1 - \frac{1}{2}k_2 + k_3) \\ \frac{Y_3 - y_n}{h} &= \frac{1}{2}\frac{Y_1 - y_n}{h} - \frac{1}{2}\frac{Y_2 - Y_1}{h} + k_3 \end{aligned} \tag{4.9}$$

Equation (4.9) gives

$$k_3 = \frac{Y_3 - Y_1 + \frac{1}{2}(Y_2 - y_n)}{h} \tag{4.10}$$

Lastly, to find y_{n+1} at the new time step, Eq. (4.4) gives

$$y_{n+1} = y_n + h(b_1k_1 + b_2k_2 + b_3k_3) \tag{4.11}$$

Substituting k_1, k_2, and k_3 from Eqs. (4.7), (4.8), and (4.10) in Eq. (4.11) and rearranging them results in

$$\begin{aligned} y_{n+1} = y_n(1 - b_1 - \frac{1}{2}b_3) + Y_1(b_1 - b_2 - b_3) \\ +Y_2(b_2 + \frac{1}{2}b_3) + Y_3b_3 \end{aligned} \tag{4.12}$$

As indicated previously, the values of b_1, b_2, and b_3 for the scheme in the original form are 1/2, -1/2, and 1. However the following temporal filter, proposed in this study, leads to other b_i values

$$y_{n+1} = \frac{\frac{1}{2}(y_n + Y_2) + \frac{1}{2}(Y_1 + Y_3)}{2} \tag{4.13}$$

The justification behind this filter goes back to the temporal locations of the Y values in different stages. Since y_n is at time t_n and Y_2 is calculated at time $t_n + 2h$, the average is

found at time $t_n + h$. In a similar way, since Y_1 and Y_3 are calculated at time $t_n + h$, so will the average. Consequently, y_{n+1} at the new time step is calculated correctly at $t_n + h$, and hence no phase error is caused by this filter.

Equalizing Eqs. (4.12) and (4.13) results in b_1, b_2, and b_3 having values of 5/8, 1/8, and 1/4. Note that this leads to four equations, where each equation equalizes y_n, Y_1, Y_2, and Y_3 coefficients in Eqs. (4.12) and (4.13), with three unknowns (b_1, b_2, and b_3), and the fourth equation is used for the verification. Now that the proposed scheme is complete, as shown in the Butcher tableau (4.6), we proceed to perform stability analyses of the two schemes (4.5) and (4.6).

4.2.1 Stability properties

Considering the standard linear test equation $\dot{y} = \lambda y$, the stability functions (see Atkinson et al., 2009 and Butcher, 2008 for complete details) of the scheme in the original form (4.5) and the proposed scheme (4.6) are given by

$$R(z) = \frac{z^2 - 4z + 2}{2(1 - z)^3}$$
$$R(z) = \frac{2z^3 - 9z^2 + 16z - 8}{8(z - 1)^3} \tag{4.14}$$

respectively, where $z = h\lambda$. A plot of the related stability regions is shown in Fig. 4.1, where the dark area shows the region of stability. Both versions of the scheme, with and without the temporal filter, are A-stable, including the left-half plane. The instability area, however, is smaller for the scheme with the proposed temporal filter. The stability functions, in addition, imply L-stability of the scheme when no temporal filter is applied, while it is not the case for the scheme with the temporal filter (for detailed explanations of A- and L-stability, see Atkinson et al., 2009 and Butcher, 2008).

For nonlinear problems, A-stability does not necessarily mean that a scheme performs well. Another form of stability which is very useful for nonlinear problems is

B-stability. If we require that the numerical solution be contractive (that is, different solutions cannot become further apart or separated), it needs to be B-stable (Atkinson et al., 2009). For a scheme to be B-stable, two conditions must be satisfied (Burrage and Butcher, 1979; Butcher, 2008):

$$B = diag(b_1, \dots, b_s)$$
$$M = BA + A^T B - bb^T \tag{4.15}$$

are nonnegative semidefinite (i.e. $x^T Mx \geq 0$ for all vectors x); where $A = \left[a_{ij}\right]$ and $b = [b_i]$.

Testing these conditions for the ME BDF scheme, both with and without the temporal filter, shows that the scheme without a temporal filter is not B-stable since there is a negative b_i in the matrix b which causes it to have a negative eigenvalue and so, not to satisfy the condition (4.15). Moreover, the matrix M of this scheme is $M = \begin{bmatrix} 0.75 & -0.25 & 0 \\ -0.25 & -1.25 & 0 \\ 0 & 0 & 1 \end{bmatrix}$ with eigenvalues of -1.2808, 0.7808, 1, and therefore is not nonnegative semidefinite in that all the eigenvalues should be nonnegative for a matrix to be nonnegative semidefinite. Alternatively, using a temporal filter as is introduced in this paper improves the scheme, allowing it to be B-stable. All b_i's in the matrix b of the scheme (4.6) are positive and the matrix M of this scheme is $M = \begin{bmatrix} 0.8594 & 0.0469 & -0.0313 \\ 0.0469 & 0.2344 & -0.1563 \\ -0.0313 & -0.1563 & 0.4375 \end{bmatrix}$ with eigenvalues of 0.1486, 0.5151, 0.8675. Hence, both matrixes B and M are nonnegative semidefinite satisfying the condition (4.15) for a scheme to be B-stable. For the solution of nonlinear systems, that is a desirable and important characteristic. To get B-stability, it is important to solve the stage equations sufficiently accurately. The simplifications commonly used in atmospheric models to reduce computational costs, such as explicit treatment of exchange coefficients in the diffusion equation (i.e. partially implicit approach (scheme (g) in KK88)), often destroys stability. This is what is demonstrated by KK88 and the

presented approach in the following sections appears to restore some of this lost stability.

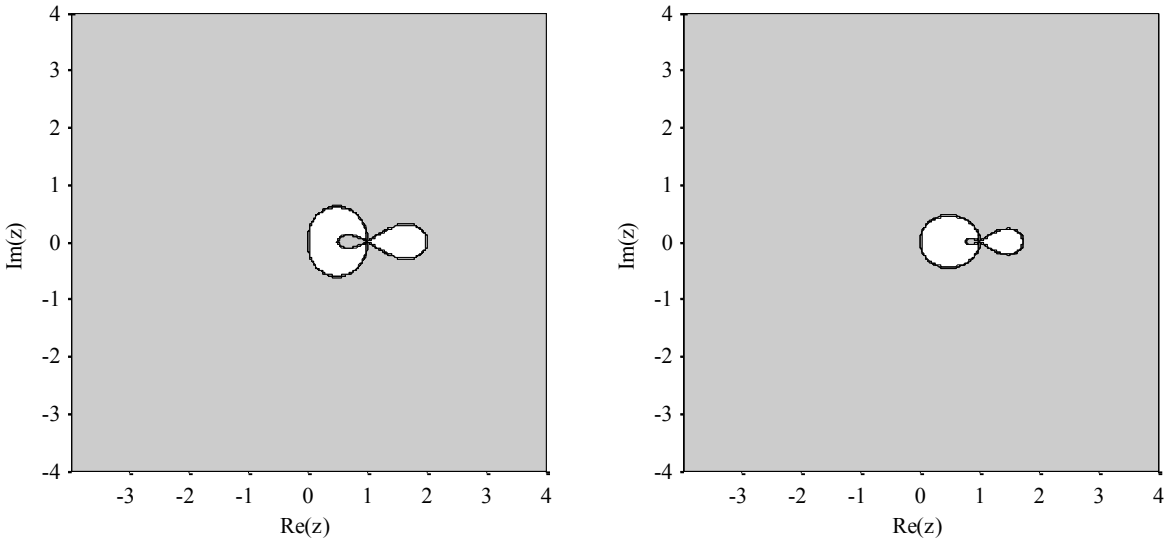

Fig. 4.1. Stability regions for the ME BDF scheme without temporal filter (Scheme (4.5)) (left) and with the proposed temporal filter (Scheme (4.6)) (right).

4.3 A Strongly Nonlinear System

In this section, a commonly used nonlinear damping equation is considered for stability and accuracy analysis (KK88)

$$\frac{\partial X}{\partial t} = -KX^P X + S \tag{4.16}$$

where X represents the temperature difference between the ground and air, $K$and P are constants in the exchange coefficient term (KX^P), and S represents all slowly varying processes such as solar radiation.

Several temporal integration schemes were tested by KK88, and most of them showed large-amplitude oscillations or spurious non-oscillatory results. KK88 introduced some simple schemes with a high range of stability and fairly accurate

results. These schemes were all first-order. The ME BDF (Modified Extended Backward Differentiation Formulae) scheme with the specific characteristics mentioned in Section 4.2 is employed in this paper.

This study deals with nonlinear exchange coefficients, and it is computationally expensive to implement the ME BDF scheme in its original form for this case. Therefore, the proposed scheme estimates the exchange coefficient semi-implicitly. For the first two stages, two calculations are performed in each in order to estimate the exchange coefficient at times $t_n+\Delta t/2$ and $t_{n+1}+\Delta t/2$ respectively. The average of the two estimations (first and second iterations) in each stage is considered as the final result of the stage. As will be shown numerically in the following, this approach improves the phase accuracy of the results. The first stage of the scheme, according to the Butcher tableau (4.6) in Section 4.2, can then be summarized as

$$\frac{X_{11} - X_n}{\Delta t} = -KX_n^P X_{11} + S_1 \tag{4.17}$$

$$\frac{X_{12} - X_n}{\Delta t} = -KX_*^P X_{12} + S_1 \tag{4.18}$$

with

$$X_* = \frac{X_n + X_{11}}{2} \tag{4.19}$$

Then,

$$X_1 = \frac{X_{11} + X_{12}}{2} \tag{4.20}$$

where S_1 is the value of $S(t_n + \Delta t)$, X_n is the value at the time t_n, X_{11} and X_{12} are the values after the first and second iterations, respectively, and X_1 is the final result of the stage 1 at time t_{n+1}.

The corresponding rate of change of X_1 (denoted by k_i in the Runge-Kutta formulation in Eq. (4.3)) is also calculated as

$$k_1 = \frac{k_{11} + k_{12}}{2} \tag{4.21}$$

where

$$k_{11} = -KX_n^P X_{11} + S_1 \tag{4.22}$$

$$k_{12} = -KX_*^P X_{12} + S_1 \tag{4.23}$$

The second stage is exactly as the same as the first, but starts from X_1, and the result will be calculated at time $t_n + 2\Delta t$.

For the third stage, the temperature variable in the exchange coefficient is calculated at time $t_n + \Delta t/2$ using

$$X_{**} = \frac{0.5(X_n + X_2) + X_1 + 2X_n}{4} \tag{4.24}$$

and according to the Butcher tableau of the scheme (4.6)

$$\frac{X_3 - X_n}{\Delta t} = \frac{1}{2}k_1 - \frac{1}{2}k_2 - KX_{**}^P X_3 + S_3 \tag{4.25}$$

where k_1 and k_2 are the Runge-Kutta coefficients in the first and second stages and $S_3 = S_1 = S(t_n + \Delta t)$.

Finally, applying the temporal filter introduced in Section 4.2 (Eq. (4.13)) in order to improve the stability of the scheme and reduce oscillations, gives the final result of X_{n+1} at new time step

$$X_{n+1} = \frac{\frac{1}{2}(X_n + X_2) + \frac{1}{2}(X_1 + X_3)}{2} \tag{4.26}$$

Note that the above filter estimates the value of X_{n+1} exactly at $t_n+\Delta t$, and therefore no phase error is introduced by this filter.

4.3.1 Linear stability analysis

If the temperature is assumed to be close to the equilibrium value (X_e), then

$$X = X_e + \delta X \tag{4.27}$$

where $X_e^{P+1} = S/K$. Replacing (4.27) in (4.16) and keeping the linear terms versus δX, we obtain

$$\frac{\partial \delta X}{\partial t} = -KX_e^P(P\delta X + \delta X) \tag{4.28}$$

It should be noted that the first linearised term in parentheses corresponds to the exchange coefficient KX^p, and the second term corresponds to the temperature term X. This is very important in the subsequent stability analyses.

The stability analysis of the proposed scheme is performed in the following. The first stage of the scheme leads to

$$\frac{\delta X_{11} - \delta X_n}{\Delta t} = -KX_e^P(P\delta X_n + \delta X_{11}) \tag{4.29}$$

Defining $\alpha = KX_e^P \Delta t$ and amplification factor $\rho = \frac{\delta X_{n+1}}{\delta X_n}$ and rearranging the equation, one obtains

$$\frac{\delta X_{11}}{\delta X_n} = \frac{1-\alpha P}{1+\alpha} \tag{4.30}$$

According to Eq. (4.19)

$$\delta X_* = \frac{\delta X_n + \delta X_{11}}{2} \tag{4.31}$$

In a similar way, according to Eq. (4.18)

$$\begin{gathered} \frac{\delta X_{12} - \delta X_n}{\Delta t} = -K X_e^P (P\delta X_* + \delta X_{12}) \\ \frac{\delta X_{12}}{\delta X_n} = \frac{1-\alpha P \frac{\delta X_*}{\delta X_n}}{1+\alpha} \end{gathered} \tag{4.32}$$

Expanding Eq. (4.32) gives $\frac{\delta X_{12}}{\delta X_n}$ as a function of α and P

$$\frac{\delta X_{12}}{\delta X_n} = \frac{(\alpha P)^2 - P(\alpha^2 + 2\alpha) + 2(1+\alpha)}{2(1+\alpha)^2} \tag{4.33}$$

And finally, according to Eq. (4.20), the amplification factor for the first stage takes the following form

$$\begin{gathered} \frac{\delta X_1}{\delta X_n} = \frac{1}{2}\left(\frac{\delta X_{11}}{\delta X_n} + \frac{\delta X_{12}}{\delta X_n}\right) \\ \frac{\delta X_1}{\delta X_n} = \frac{(\alpha P)^2 - P(3\alpha^2 + 4\alpha) + 4(1+\alpha)}{4(1+\alpha)^2} \end{gathered} \tag{4.34}$$

Then, since $k_1 = \frac{X_1 - X_n}{\Delta t}$

$$\delta k_1 . \Delta t = \delta X_1 - \delta X_n \tag{4.35}$$

$$\frac{\delta k_1.\Delta t}{\delta X_n} = \frac{\delta X_1}{\delta X_n} - 1$$

The same process is performed for the second stage, with the difference being that the starting point is X_1. Thus

$$\begin{aligned} \frac{\delta X_2}{\delta X_1} &= \frac{\delta X_1}{\delta X_n} \\ \frac{\delta X_2}{\delta X_n} &= \left(\frac{\delta X_1}{\delta X_n}\right)^2 \end{aligned} \tag{4.36}$$

and since $k_2 = \frac{X_2 - X_1}{\Delta t}$

$$\begin{aligned} \delta k_2.\Delta t &= \delta X_2 - \delta X_1 \\ \frac{\delta k_2.\Delta t}{\delta X_n} &= \left(\frac{\delta X_1}{\delta X_n}\right)^2 - \frac{\delta X_1}{\delta X_n} \end{aligned} \tag{4.37}$$

Employing the same procedure for the third stage, considering Eq. (4.25), substituting the values of δk_1 and δk_2 from Eqs. (4.35) and (4.37), and linearising, the third stage leads to

$$\frac{\delta X_3}{\delta X_n} = \frac{1}{1+\alpha}\left\{1 - \frac{1}{2}\left(\frac{\delta X_1}{\delta X_n} - 1\right) + \frac{1}{2}\frac{\delta X_1}{\delta X_n}\left(\frac{\delta X_1}{\delta X_n} - 1\right) - \alpha P \frac{\delta X_{**}}{\delta X_n}\right\} \tag{4.38}$$

and finally, by implementing the time filter, the following amplification factor (ρ) is obtained for the proposed scheme

$$\frac{\delta X_{n+1}}{\delta X_n} = \frac{1}{4}\left(1 + \frac{\delta X_1}{\delta X_n} + \frac{\delta X_2}{\delta X_n} + \frac{\delta X_3}{\delta X_n}\right) \tag{4.39}$$

or, in the form of an explicit function of α and P

$$\frac{\delta X_{n+1}}{\delta X_n} = \frac{1}{4}\Bigg[1 + \frac{(\alpha P)^2 - P(3\alpha^2 + 4\alpha) + 4(1+\alpha)}{4(1+\alpha)^2} + \left(\frac{(\alpha P)^2 - P(3\alpha^2 + 4\alpha) + 4(1+\alpha)}{4(1+\alpha)^2}\right)^2 + \frac{1}{1+\alpha}\Bigg\{1 + \frac{\alpha}{2}\Bigg[\frac{1}{2}\left(\frac{(\alpha P)^2 - P(3\alpha^2 + 4\alpha) + 4(1+\alpha)}{4(1+\alpha)^2}\right)^2 - \frac{(\alpha P)^2 - P(3\alpha^2 + 4\alpha) + 4(1+\alpha)}{4(1+\alpha)^2} + \frac{1}{2}\Bigg] - \frac{\alpha P}{8}\Bigg[5 + \frac{(\alpha P)^2 - P(3\alpha^2 + 4\alpha) + 4(1+\alpha)}{2(1+\alpha)^2} + \left(\frac{(\alpha P)^2 - P(3\alpha^2 + 4\alpha) + 4(1+\alpha)}{4(1+\alpha)^2}\right)^2\Bigg]\Bigg\}\Bigg] \tag{4.40}$$

The amplification factor should lie between $-1 < \rho < 1$ in order to have a stable and convergent solution. However, if $0 < \rho < 1$, the solution will be damped monotonically, and if $-1 < \rho < 0$, the solution will have an oscillatory damping form. Various nonlinear time integration schemes up to two-time-level methods were discussed by KK88. They showed that for $\rho > 1$, a spurious behaviour is obtained and the methods lead to a false solution, while for $\rho < -1$, large amplitude oscillations occur. The scheme proposed here is stable in the large area shown in Fig. 4.2, and will also be shown numerically in the following. The reason for the large area of stability in the proposed scheme as compared to the ME BDF scheme without temporal filter is the use of the appropriate time filter at each NWP model time step. Note that the stability criterion is related to the power P in addition to the usual stability parameter α. A comparison of the stability region of the proposed scheme and the following methods, forward explicit, explicit exchange coefficient/implicit temperature, and time-filtered explicit exchange coefficient/implicit temperature methods (schemes a, d, and h, respectively in KK88) is shown in Fig. 4.2. Note that scheme (h) is the most stable

scheme in KK88's study. The lines represent $|\rho| = 1$, and the stability region is beneath the line of each scheme.

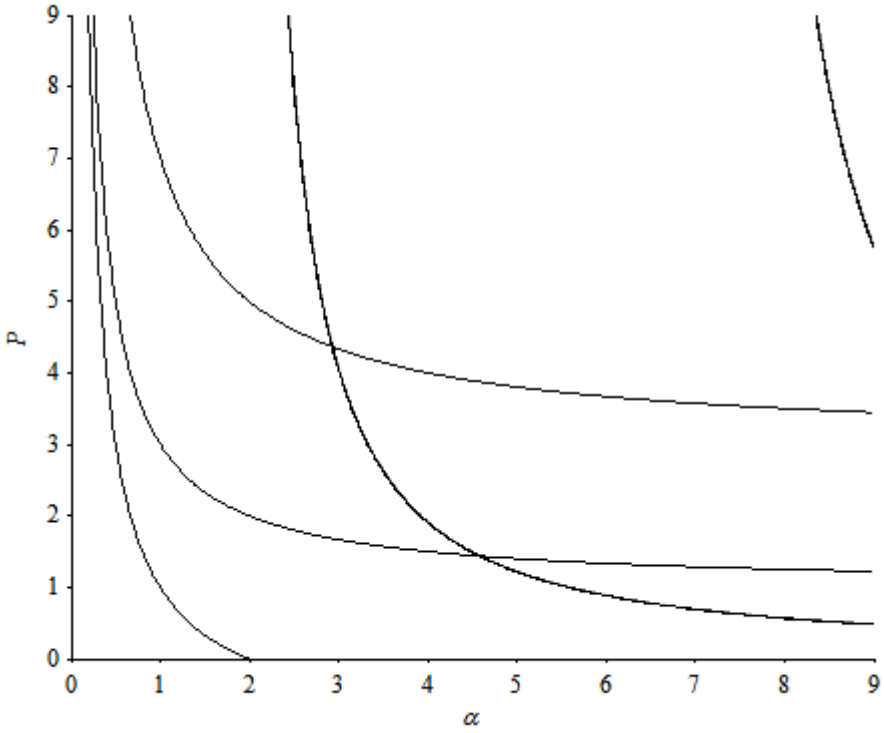

Fig. 4.2. Stability limits of: a) forward explicit method, d) explicit exchange coefficient/implicit temperature method, h) the time-filtered explicit exchange coefficient/implicit temperature method, m) the ME BDF method without temporal filter, and the proposed method.

It can be observed that the proposed ME BDF scheme is stable over a wide range of P and α, which is comprehensive for atmospheric conditions. It performs considerably better than the other schemes, and it will also be numerically shown in Section 4.3.3 that the proposed scheme is stable and convergent.

4.3.2 Asymptotic error analysis

The asymptotic errors are derived for the ME BDF scheme both with and without the temporal filter in order to examine the local truncation error. Following the method of Diamantakis et al. (2006), the response functions of the schemes to the nonlinear

problem of KK88 are obtained by using the linear perturbation analysis in Section 4.3.1, and then compared to the analytical solution of the perturbed problem (4.28) response function

$$E_A = \frac{\delta X(t_{n+1})}{\delta X(t_n)} = e^{-\alpha(P+1)} \tag{4.41}$$

The Taylor series expansion of (4.41) in α for a particular value of P gives

$$T(E_A) = 1 - (P+1)\alpha + \frac{1}{2}(P+1)^2\alpha^2 + O(\alpha^3) \tag{4.42}$$

To obtain an error estimate for the response function of the proposed ME BDF scheme, we go through the same process as in the linear stability analysis in Section 4.3.1. Starting from the first stage by expanding (4.17) gives

$$T_{11} = 1 - (P+1)\alpha + (P+1)\alpha^2 + O(\alpha^3) \tag{4.43}$$

where T_{11} is the Taylor series expansion for the response function of X_{11}. We continue with

$$T_{12} = 1 - (P+1)\alpha + (0.5P^2 + 1.5P + 1)\alpha^2 + O(\alpha^3) \tag{4.44}$$

$$T_1 = 1 - (P+1)\alpha + (0.25P^2 + 1.25P + 1)\alpha^2 + O(\alpha^3) \tag{4.45}$$

According to (4.36),

$$\begin{gathered} T_2 = (T_1)^2 \\ T_2 = 1 - (2P+2)\alpha + (1.5P^2 + 4.5P + 3)\alpha^2 + O(\alpha^3) \end{gathered} \tag{4.46}$$

and according to (4.35) and (4.37), the response functions of $\delta k_1.\Delta t$ and $\delta k_2.\Delta t$ are

$$T(\delta k_1.\Delta t) = T_1 - 1 \tag{4.47}$$

$$T(\delta k_2.\Delta t) = T_2 - T_1 \tag{4.48}$$

Equation (4.24) gives

$$\begin{aligned} T_{**} &= \frac{1}{4}(2.5 + T_1 + 0.5T_2) \\ T_{**} &= 1 - 0.5(P+1)\alpha + (0.25P^2 + 0.875P + 0.625)\alpha^2 \\ &\quad + O(\alpha^3) \end{aligned} \tag{4.49}$$

So, from (4.25),

$$T_3 = 1 - (P+1)\alpha + 0.5(P+1)\alpha^2 + O(\alpha^3) \tag{4.50}$$

And finally, according to (4.26),

$$\begin{aligned} T_{n+1} &= 1 - (P+1)\alpha + (0.4375P^2 + 1.5625P + 1.125)\alpha^2 \\ &\quad + O(\alpha^3) \end{aligned} \tag{4.51}$$

Thus the asymptotic error estimate for small values of α for the response of the proposed scheme is

$$\begin{aligned} TE &= T(E_A) - T_{n+1} \\ TE &= [0.0625P^2 - 0.5625P - 0.625]\alpha^2 + O(\alpha^3) \end{aligned} \tag{4.52}$$

The leading error term of the proposed scheme obtained in Eq. (4.52) is plotted against the corresponding term for the ME BDF scheme in this study without temporal filter as well as two of the semi-implicit schemes from Diamantakis et al. (2006), one of which is equivalent to the scheme (g) of KK88 and the other being the generalization of the scheme (f) of KK88 with the introduced parameters $\alpha = 1/3$, $\xi_1 = 3/2$, $\xi_2 = 1$ (see Diamantakis et al. 2006 for the details). The latter is the proposed scheme in their paper. The leading error terms are normalized by α^2 and are plotted as functions of P in Fig. 4.3. It shows that, asymptotically, the proposed scheme is noticeably more accurate than the other schemes when the nonlinearity intensifies though it does not have the smallest leading error for smaller P's. The leading error term remains small for a very wide range of P. One remarkable point illustrated by Fig. 4.3 is how effective the temporal filter is in the performance of the ME BDF scheme.

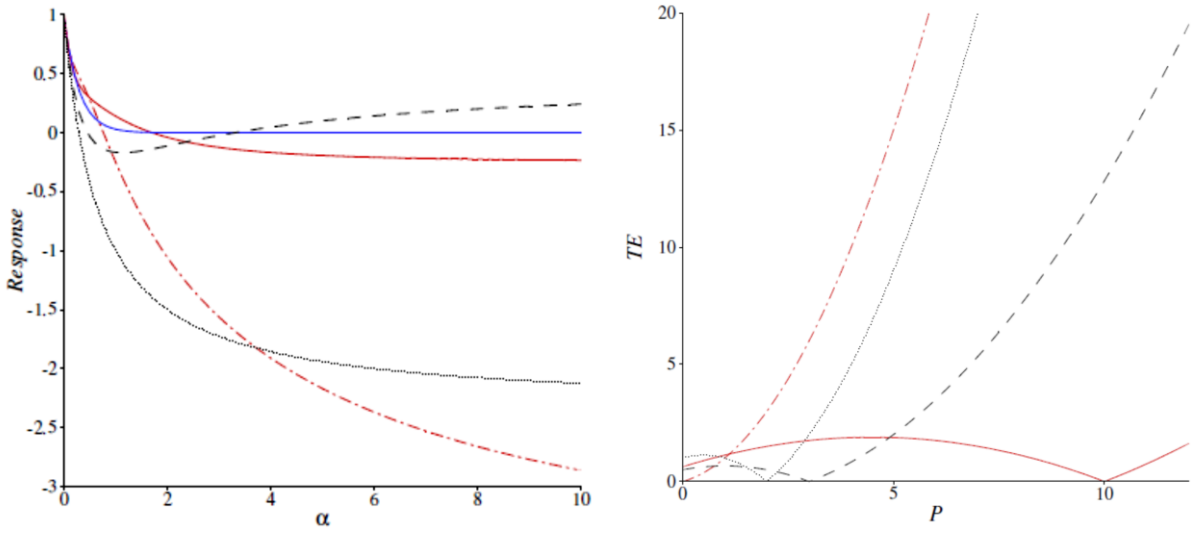

(a) (b)

Fig. 4.3. a) Analytic response (thick solid line) compared with: scheme (g) of KK88 with $\gamma = 1.5$ (extrapolated scheme) (dotted line); Diamantakis et al. (2006) proposed predictor-corrector scheme with $\alpha = 1/3$, $\xi_1 = 3/2$, $\xi_2 = 1$ (dashed line); The ME BDF scheme without temporal filter (dash-dotted line); and the proposed ME BDF scheme with temporal filter (solid line).

b) Absolute value of the normalized leading error term versus P for: scheme (g) of KK88 with $\gamma = 1.5$ (extrapolated scheme) (dotted line); Diamantakis et al. (2006) proposed predictor-corrector scheme with $\alpha = 1/3$, $\xi_1 = 3/2$, $\xi_2 = 1$ (dashed line); The ME BDF scheme without

temporal filter (dash-dotted line); and the proposed ME BDF scheme with temporal filter (solid line).

4.3.3 Numerical experiments

The numerical integration of the temperature equation is performed using the proposed ME BDF scheme. To solve the equation, S is assumed to be similar to KK88

$$S_n = 1 + sin\left(\frac{2\pi t}{20}\right) \tag{4.53}$$

where t is the time. Similar to KK88, $K = 10$, but Δt is variable in order to examine scheme stability and accuracy. A highly nonlinear case of $P = 4$ is considered here. The results of the proposed ME BDF scheme for $\Delta t = 0.5$ are shown in Fig. 4.4, along with schemes (d) and (h). They are compared to second-order Crank-Nicolson scheme results as the reference solution (dotted line). The reference solution is hardly distinguishable in Fig. 4.4, since other schemes results are superimposed there.

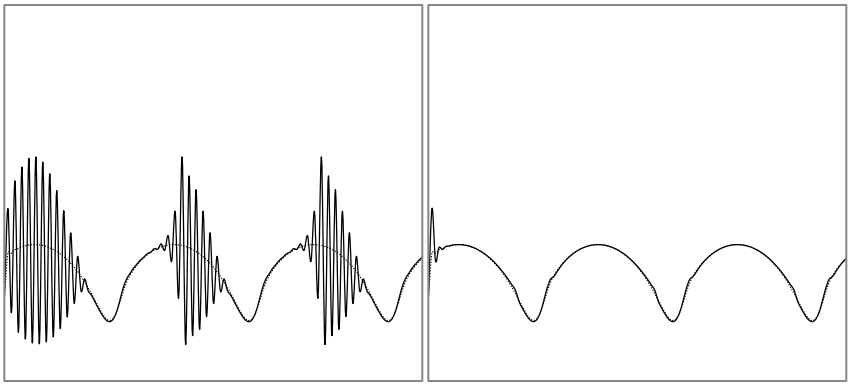

(a) (b)

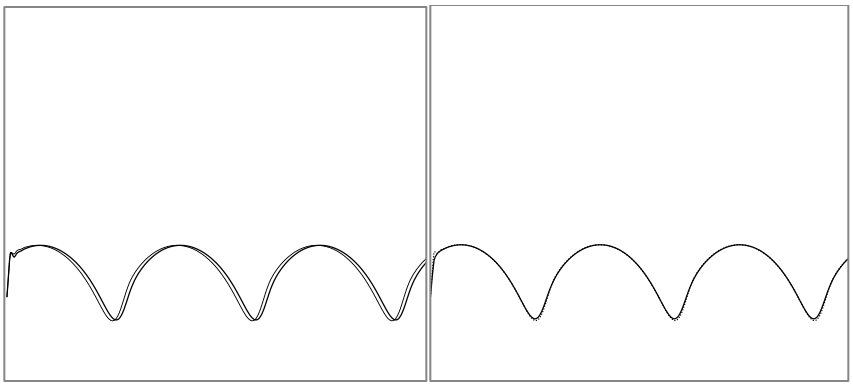

(c) (d)

Fig. 4.4. The numerical results from a) scheme (d); b) scheme (d) with time-filter adjustment of scheme (h); c) the ME BDF scheme without temporal filter; and d) the proposed scheme for $P = 4$ and $\Delta t = 0.5$. Horizontal axis shows time, and vertical axis shows *X*.

Fig. 4.4.a shows that scheme (d) is highly oscillatory but still bounded between two values, despite being in the instability region in Fig. 4.2. After the application of the time filter of scheme (h), scheme (d) leads to very good results in Fig. 4.4.b. Scheme (d) with the application of the time filter used in scheme (h) exhibits some minor errors in the rising and falling regions of the graph, and it is worth mentioning that this results from a combination of two first-order schemes, which causes a break point in the graph when it switches between the two schemes. The break point may cause some errors and oscillations for more sensitive cases. Scheme (d) with the application of the time filter used in scheme (h) is also not temporally accurate since its final result is approximated at time $t_n+\Delta t/2$, which suggests that it is not consistent with the continuous equations (KK88). The ME BDF scheme without the temporal filter of Eq. (4.13) results in Fig. 4.4.c, which shows good results against the reference solution for the small time step of 0.5; however, there is a slight phase shift in the solution. The proposed scheme solution in Fig. 4.4.d shows very good agreement with the reference solution as well as no oscillations after the initial adjustment. The superiority of the proposed scheme is more significant when the time step increases; it leads to better results, as shown in the following. In Fig. 4.5, the same schemes are compared for $\Delta t = 1.5$.

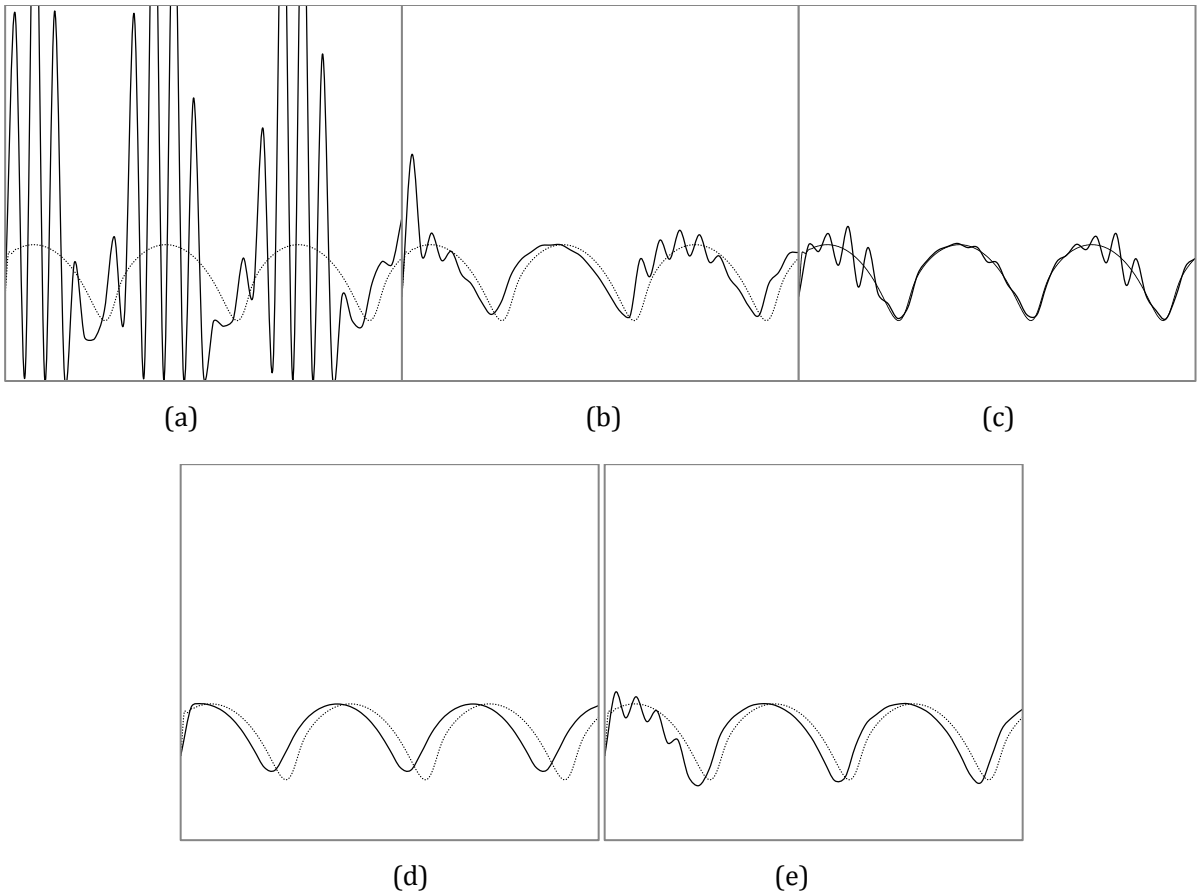

Fig. 4.5. The numerical results from: a) scheme (d); b) scheme (d) with time-filter adjustment of scheme (h); c) the ME BDF scheme without temporal filter; d) the proposed scheme; and e) Crank-Nicolson scheme for $\Delta t = 1.5$. Horizontal axis shows time, and vertical axis shows X.

As expected, scheme (d) shows larger oscillations in this case. Scheme (d) with the time-filter adjustment of scheme (h) is also very sensitive to the time step size, as shown in Fig. 4.5.b. The ME BDF scheme without the temporal filter exhibits some oscillations in the solution, while the phase shift of the solution remains unchanged versus Fig. 4.4.c, with $\Delta t = 0.5$. The proposed scheme is still oscillation-free. It should be noted that according to the linear stability analysis in Fig. 4.2, the proposed scheme is still far from the instability region, as the maximum solution is around 0.7, and thus, $\alpha \approx 3.6$; the present numerical test also does not exhibit instability in this case. It can be shown that even for larger time steps, the scheme is not only stable and returns no numerical oscillations, but also gives good results, albeit with some errors. The Crank-Nicolson fully implicit scheme results are also shown in Fig. 4.5.e for comparison. The strength of the proposed scheme is revealed more here, since this scheme and the

Crank-Nicolson scheme show the same behaviour with similar phase errors. The incurred phase shift is a result of the nature of implicit schemes for solving stiff equations. When the time step increases, these schemes are not capable of capturing the stiff solution component, and a phase shift occurs in the slowly varying solution component. The difference between the two schemes, as shown in Fig. 4.5.d, is that the proposed scheme shows some underestimation of the solution for smaller values of X (implying a more stable condition), while the Crank-Nicolson scheme shows overestimation along with some oscillations in the initial adjustment. Note that the Crank-Nicolson scheme used is fully implicit with a large number of iterations, which leads to high computational cost, but our scheme, as explained in Section 4.3, solves the equation semi-implicitly, with at most one iteration per step. For further investigation, the results of the last four schemes are compared in Fig. 4.6 for $\Delta t = 3$. As mentioned previously, the proposed scheme (Fig. 4.6.c) still shows acceptable results with some phase error and more underestimation of the more stable parts (shown by the smaller temperature values) of the solution. The same behaviour can be observed for the Crank-Nicolson scheme, but with more overestimation of the minimum value of the temperature. On the other hand, scheme (d) combined with the time-filter of scheme (h) from KK88 shows oscillatory results with much larger errors in both phase and amplitude. The same behaviour can be observed for the ME BDF scheme without the temporal filter, which again highlights the effect of the temporal filter proposed in this study.

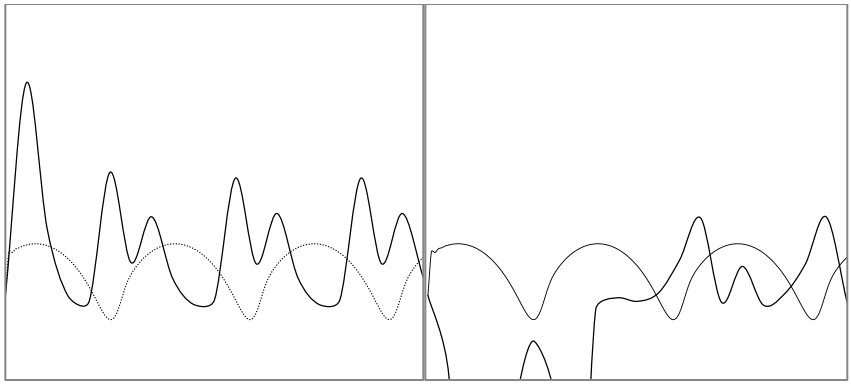

(a) (b)

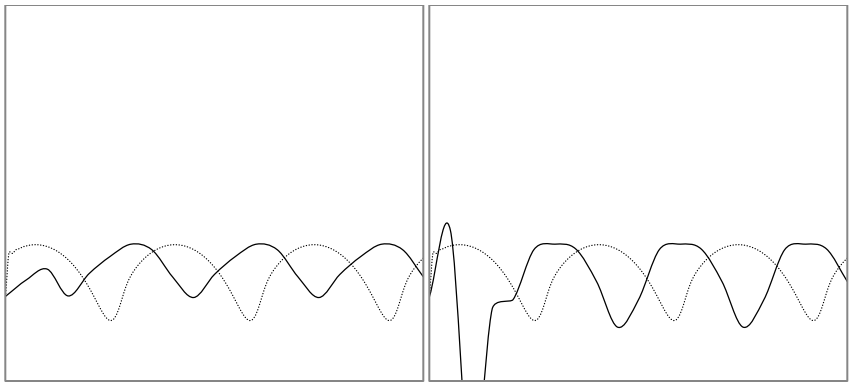

(c) (d)

Fig. 4.6. The numerical results from: a) scheme (d) with time-filter adjustment of scheme (h); b) the ME BDF scheme without temporal filter; c) the proposed scheme; and d) Crank-Nicolson scheme for $P = 4$ and $\Delta t = 3$. Horizontal axis shows time, and vertical axis shows X.

4.4 Nonlinear Diffusive System

Nonlinear diffusion equations appear in many applications, including Navier-Stockes and shallow water systems, magnetohydrodynamics, and atmospheric boundary layer equations. As an example of a highly nonlinear diffusive system, in this chapter we consider a commonly used model for atmospheric boundary layers. In this model, two diffusion equations are solved for wind velocity and potential temperature

$$\frac{\partial u}{\partial t} = \frac{\partial}{\partial z}\left(K\frac{\partial u}{\partial z}\right) \tag{4.54}$$

$$\frac{\partial \theta}{\partial t} = \frac{\partial}{\partial z}\left(K\frac{\partial \theta}{\partial z}\right) \tag{4.55}$$

Although the diffusion coefficients are generally different for wind and temperature, which has been investigated in some studies (e.g. Benard et al., 2000), they are assumed to be equal in this study and are obtained from the following equation (GD90)

$$K = l^2\left|\frac{\partial u}{\partial z}\right|(1 + b|Ri|)^n, \qquad \left(\frac{\partial u}{\partial z} \neq 0\right) \tag{4.56}$$

where l is the mixing length, n and b are constants, and Ri is the Richardson number

$$Ri = \frac{g}{\theta_0}\frac{\partial\theta/\partial z}{(\partial u/\partial z)^2} \tag{4.57}$$

where g is the gravity acceleration and θ_0 is a constant. The mixing length is also variable with the elevation, but it is assumed in this study to be constant.

As the static stability increases, K should gradually vanish, while it grows as the static instability intensifies. To obtain this behaviour, n and b must vary according to stability, and only one of them must change sign when the stability sign changes. As the results of this study will be compared with GD90's study, the same values of n and b are considered, which are

$$\begin{aligned} n = -2; b = 5 \quad &\text{for } Ri > 0 \\ n = \frac{1}{2}; b = 20 \quad &\text{for } Ri < 0 \end{aligned} \tag{4.58}$$

4.4.1 Numerical stability analysis

The analytical stability of the system of equations has been established by GD90. They also studied the stability of a class of two-time-level schemes. The proposed ME BDF scheme is now analyzed in the following.

Considering explicit diffusion coefficient and implicit velocity, the diffusion equation (4.54) can be written as

$$u_t = (Ku_z^+)_z = K_z u_z^+ + Ku_{zz}^+ \tag{4.59}$$

The plus sign designates the next time step. GD90 showed that K_z is given by

$$K_z = \frac{K(1-2\alpha)}{u_z}u_{zz} + \frac{K\alpha}{\theta_z}\theta_{zz} \tag{4.60}$$

where

$$\alpha = \frac{nb|Ri|}{1 + b|Ri|} \tag{4.61}$$

Consideration of solutions of the form $u = ce^{\omega t + imz}$ leads to $u^+ = \lambda u$, where λ is an amplification factor and c is a constant. Now, if we replace all terms in Eq. (4.59) using a second-order centered scheme for first- and second-order derivatives, we obtain

$$\begin{aligned} u_{1t} &= \left(\frac{K(1-2\alpha)}{\frac{u_{n(j+1)} - u_{n(j-1)}}{2\Delta z}} \frac{u_{n(j+1)} - 2u_{n(j)} + u_{n(j-1)}}{\Delta z^2} \right. \\ &\left. + \frac{K\alpha}{\frac{\theta_{n(j+1)} - \theta_{n(j-1)}}{2\Delta z}} \frac{\theta_{n(j+1)} - 2\theta_{n(j)} + \theta_{n(j-1)}}{\Delta z^2} \right) \frac{u_{1(j+1)} - u_{1(j-1)}}{2\Delta z} \\ &+ K \frac{u_{1(j+1)} - 2u_{1(j)} + u_{1(j-1)}}{\Delta z^2} \end{aligned} \tag{4.62}$$

for the first stage, in which u_1 is the velocity at time t_{n+1} after the first stage. This discretized equation leads to a tridiagonal system, which is very computationally efficient to solve. Replacing the discretized terms by their equivalent form ($u_{n(j+1)} = u_n e^{im(\Delta z)}$ and $u_1 = \lambda_1 u_n$), we obtain

$$
\begin{aligned}
&u_{1t} \\
&= \left(\frac{2K(1-2\alpha)}{u_n(2isin(m\Delta z))} \frac{u_n(-4sin^2\left(\frac{m\Delta z}{2}\right))}{\Delta z} \right. \\
&\left. + \frac{2K\alpha}{\theta_n(2isin(m\Delta z))} \frac{\theta_n(-4sin^2\left(\frac{m\Delta z}{2}\right))}{\Delta z} \right) \frac{\lambda_1(2isin(m\Delta z))}{2\Delta z} u_n \\
&+ K \frac{-4\lambda_1 sin^2\left(\frac{m\Delta z}{2}\right)}{\Delta z^2} u_n
\end{aligned}
\tag{4.63}
$$

Finally,

$$
u_{1t} = \frac{-4Ksin^2\left(\frac{m\Delta z}{2}\right)}{\Delta z^2}(2-\alpha)\lambda_1 u_n \tag{4.64}
$$

Since $u_1 = u_n + u_{1t}\Delta t$, one obtains

$$
\lambda_1 = \frac{1}{1 + \frac{4Ksin^2\left(\frac{m\Delta z}{2}\right)(2-\alpha)\Delta t}{\Delta z^2}} \tag{4.65}
$$

The procedure is the same for all three stages. The second stage is exactly the same as the first, only differing in the starting point, which is $u_1 = \lambda_1 u_n$. Thus, $\lambda_2 = \lambda_1$ where $u_2 = \lambda_2 u_1$.

According to the Butcher tableau of scheme (4.6), for the third stage

$$
u_{3t} = \frac{1}{2}k_1 - \frac{1}{2}k_2 + (Ku_{3z})_z \tag{4.66}
$$

where

$$k_1 = \frac{u_1 - u_n}{\Delta t} = \frac{\lambda_1 - 1}{\Delta t} u_n \tag{4.67}$$

$$k_2 = \frac{u_2 - u_1}{\Delta t} = \frac{(\lambda_2 - 1)\lambda_1}{\Delta t} u_n \tag{4.68}$$

$$u_3 = \lambda_3 u_n \tag{4.69}$$

If we proceed as in the first stage, the third term in Eq. (4.66) will be exactly the same as it was in Eq. (4.64) for the first stage. Thus, u_{3t} is obtained as

$$u_{3t} = \frac{1}{2}\left(\frac{\lambda_1 - 1}{\Delta t} - \frac{(\lambda_2 - 1)\lambda_1}{\Delta t}\right) u_n + \frac{-4Ksin^2\left(\frac{m\Delta z}{2}\right)}{\Delta z^2}(2 - \alpha)\lambda_3 u_n \tag{4.70}$$

As $u_3 = u_n + u_{3t}\Delta t$, the final result is written as

$$\lambda_3 = \frac{\lambda_1 + \frac{1}{2}(1 - \lambda_1\lambda_2)}{1 + \frac{4Ksin^2\left(\frac{m\Delta z}{2}\right)(2 - \alpha)\Delta t}{\Delta z^2}} \tag{4.71}$$

As mentioned previously, $\lambda_2 = \lambda_1$. Finally, the introduced temporal filter is employed in order to get non-oscillatory results, as follows

$$u_{n+1} = \frac{\frac{1}{2}(u_n + u_2) + \frac{1}{2}(u_1 + u_3)}{2} \tag{4.72}$$

where u_{n+1} is the velocity at the new time step. Consequently, the final amplification factor is obtained as

$$\lambda = \frac{1}{4}(1 + \lambda_1 + \lambda_1\lambda_2 + \lambda_3) \tag{4.73}$$

The same calculations can be done for the temperature equation.

The amplitude A of a wave of length $\gamma = \frac{2\pi}{m}$, diffused by coefficient K as a function of time for various spatial resolutions, is given by (GD90)

$$A(m\Delta z, t) = exp\left[-m^2 Kt(2-\alpha)\frac{sin^2\left(\frac{m\Delta z}{2}\right)}{\left(\frac{m\Delta z}{2}\right)^2}\right] \tag{4.74}$$

This amplitude is free of temporal truncation error, as shown in Fig. 4.7 for various spatial resolutions (2, 3, 4, 8, ∞). It shows that weakly resolved waves are diffused more slowly.

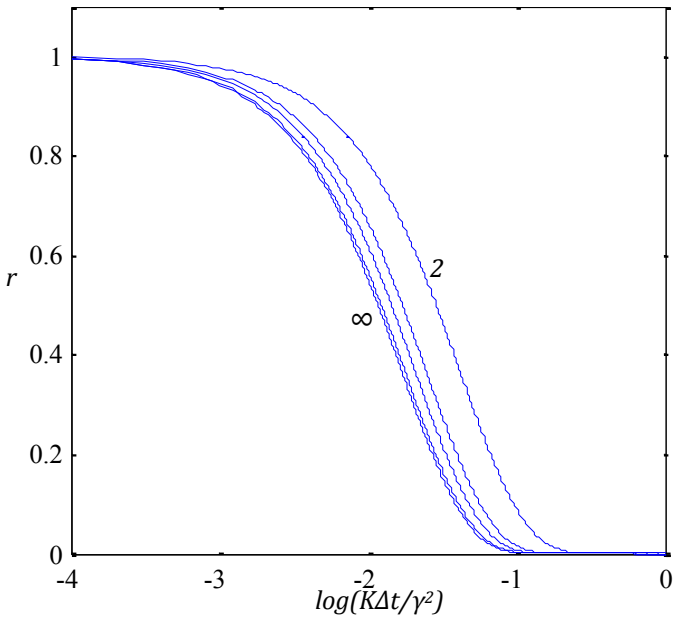

Fig. 4.7. The analytical amplitude of diffusing wave of length γ for various spatial resolutions as a function of time. Numbers on the curves represent spatial resolution ($\gamma/\Delta z$).

The ratio r is defined as follows, representing the reduction in numerical amplitude over the analytical one

$$r = \frac{1-\lambda}{1-A(0,\Delta t)} \tag{4.75}$$

The case $r < 1$ results in underestimation of the analytical diffusion, and $r > 1$ results in excessive numerical diffusion. The r ratio of the proposed scheme is shown in Fig. 4.8 along with the GD90 proposed scheme and the fully implicit one with $\beta_1 = \beta_2 = \beta$ and $\beta_1 = \beta_2 = 1$, respectively (refer to GD90 for more details). The proposed scheme with time filter (Fig. 4.8.a) seems to be less accurate than without the filter (Fig. 4.8.b) as the time step increases (i.e. for $K\Delta t/\gamma^2 \geq 10^{-1.5}$). But from another point of view, in large time steps, while the analytical wave amplitude exhibits no diffusion, the proposed scheme induces numerical diffusion, which helps in damping the oscillations. It is worth mentioning that the linear stability analysis results do not necessarily mean that the proposed scheme is less accurate. As will be shown in the numerical results, the proposed scheme performs very well for large time steps, although its r ratio is around 0.7. On the other hand, Fig. 4.8.b indicates that our scheme without a temporal filter is more accurate than the fully implicit scheme (Fig. 4.8.d). It is more consistent as the time step size increases. This means that the minimum r ratio is greater (and the maximum numerical diffusion is less) than in the fully implicit scheme when the spatial resolution increases. Hence, in case accuracy problems occur as the time step increases, the proposed ME BDF scheme may be used without the temporal filter. This feature is a result of the previously-mentioned L-stability of the scheme when no temporal filter is applied. For the ME BDF scheme, both with and without the temporal filter, behaviour similar to that of the fully implicit scheme is observed. The waves of length $2\Delta z$ (lowest spatial resolution) lead to the largest error in the region of small Δt values, and the waves with different lengths do not cross each other while Δt increases. Lastly, although the GD90 schemes result in stable conditions, they may no longer be second-order, and they are highly dependent on spatial resolution in order to achieve accurate results.

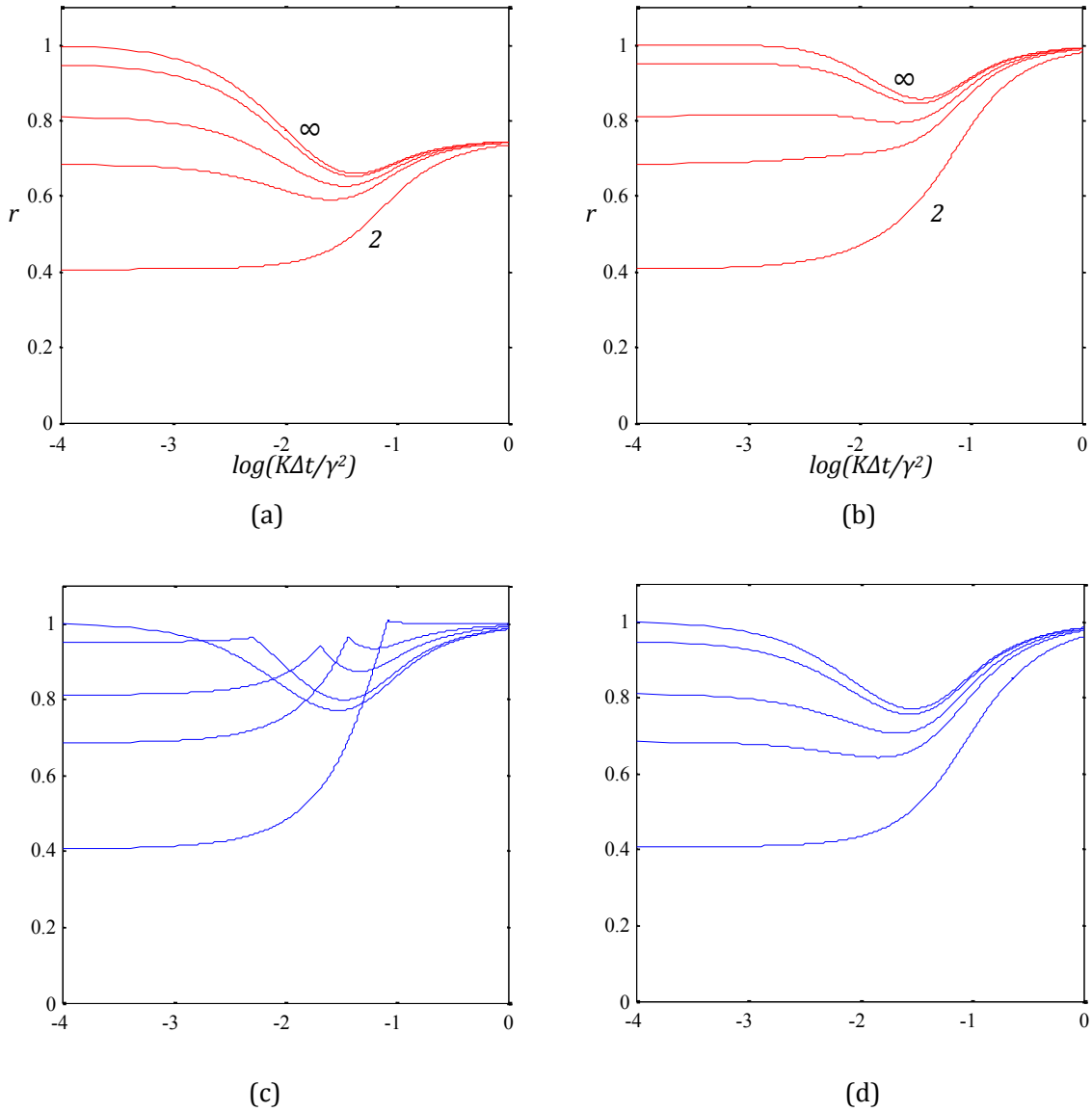

Fig. 4.8. The ratio of reduction of numerical amplitude to that of the analytical one (r) for the proposed ME BDF scheme: a) with temporal filter; b) without temporal filter; c) GD90 proposed scheme ($\beta_1 = \beta_2 = \beta$); and d) GD90 $\beta_1 = \beta_2 = 1$ (fully implicit) scheme for various spatial resolutions (2, 3, 4, 8, ∞).

4.4.2 Application

An idealized case similar to GD90 is considered in order to compare our results with their study. The problem specifications are:

- K is obtained from Eqs. (4.56) and (4.58) with $l = 50$ m

- Boundary conditions are $u = 0\ m/s$ and $\theta = 0$ ℃ at $z = 0$, and zero gradient at $z = 1000\ m$
- Initial conditions are $u = 10\ m/s$, and θ varies linearly with z from 0 ℃ to 1 ℃

According to GD90, the vertical resolution should be chosen very carefully for two reasons: 1) the traditional schemes for vertical diffusion in NWP models may cause oscillatory, inaccurate results if the vertical resolution is higher than a specific limit; and 2) an unwanted delay may occur in the solution, since K is calculated explicitly and the atmospheric flow propagation from the high K-value region to the low K-value region (boundary layer to free atmosphere) can take place at a maximum rate of one grid point per time step. GD90 also mentioned that the delay could occur for their proposed scheme if the vertical resolution was not carefully chosen.

Our proposed semi-implicit ME BDF scheme has greatly mitigated these drawbacks. The calculated wind profile and potential temperature vertical distribution using our scheme are shown in Fig. 4.9 (solid line) for the stable and unstable boundary layers for two vertical resolutions and with the same time step size as GD90, $\Delta t = 1{,}800\ s$.

The proposed method gives accurate results for $\Delta z = 100$ m, and is very close to the reference solution calculated using the traditional first-order implicit scheme (which includes explicit diffusion coefficient and implicit variable) with a very fine grid and $\Delta t = 120$ s (dashed line), which is hardly distinguishable in Fig. 4.9 since the results are very close. There is a small discrepancy between the proposed scheme results for $\Delta z = 20$ m and the exact solution ($\Delta z = 20$ m is five times higher spatial resolution than $\Delta z = 100$ m). This implies that the scheme is not very sensitive to spatial resolution. To understand the importance of this issue, the results of the extrapolated scheme (g) in KK88 are considered; as is mentioned in KK88 who refer to ECMWF in the context of scheme (g). As can be seen in Fig. 4.9, the results of this scheme are also close to the reference solution and the proposed scheme results for $\Delta z = 100$ m. However, when Δz is reduced to 20 m, large discrepancies occur using the scheme (g) (dotted line). In fact, the wind is not diffused in this case. Since the computational cost of the proposed scheme is three times the computational cost of the

scheme (g), we found the solution for $\Delta z = 20$ m using the latter scheme with $\Delta t = 600$ s, which is three times less than the previously-mentioned $\Delta t = 1{,}800\ s$. The results show that with the reduced time step size, the scheme (g) is capable of diffusing the wind and potential temperature in the stable boundary layer (Fig. 4.9.a) with small discrepancies from the proposed scheme results; however, in the unstable boundary layer (Fig. 4.9.b), there are fairly larger errors in the scheme (g) results according to the exact solution. The solution of the diffusive nonlinear system using the ME BDF scheme without the temporal filter is also shown in Fig. 4.9 (dash-dot). The results are close to the proposed scheme solutions, but oscillatory.

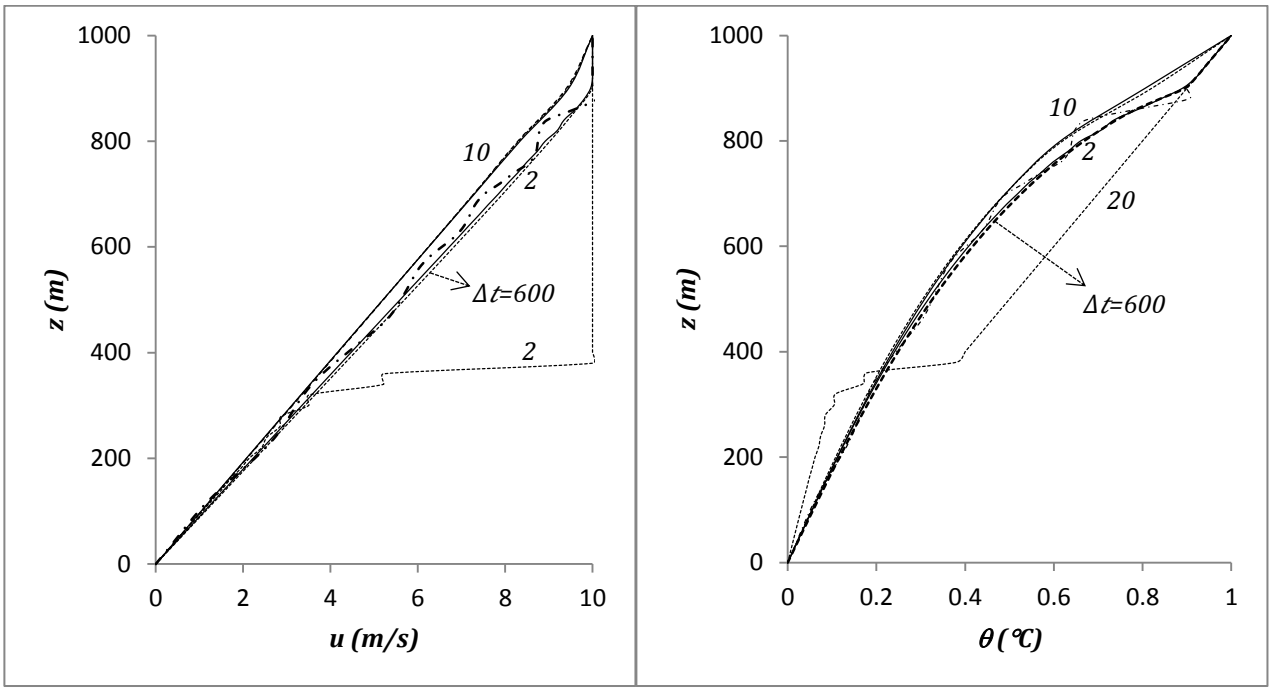

(a)

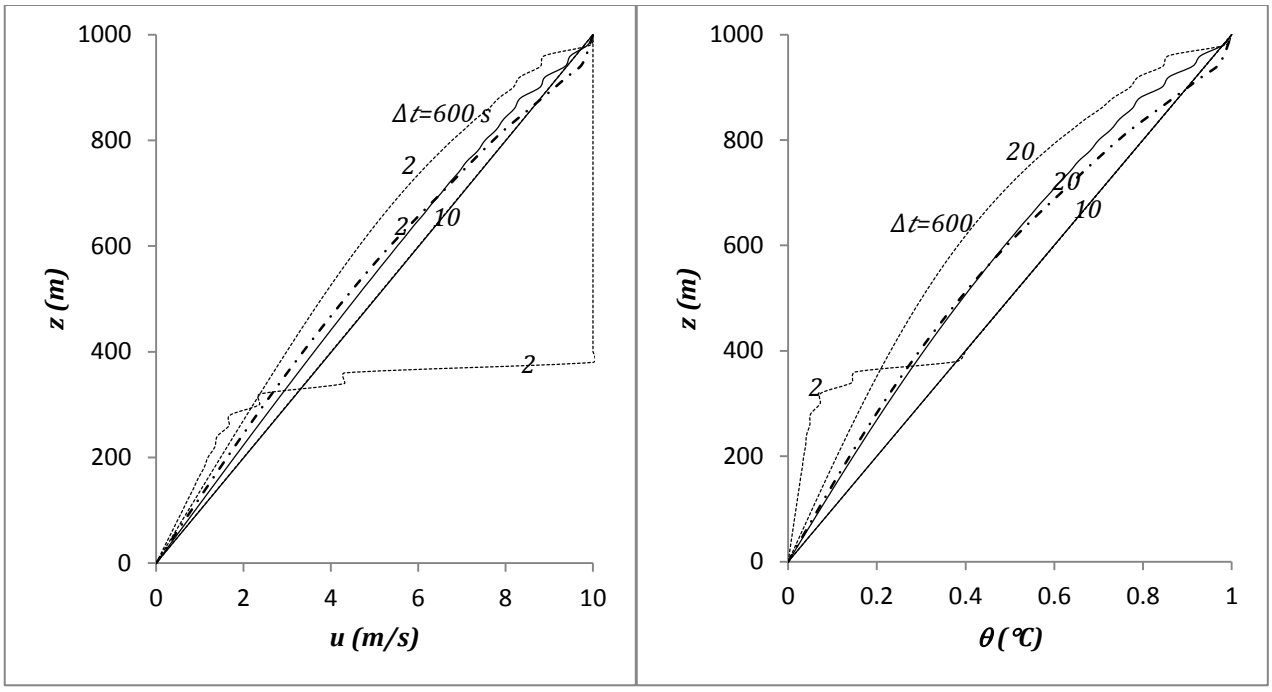

(b)

Fig. 4.9. Wind and potential temperature profile after 4 hours for two vertical resolutions for the idealized case described in Section 4.2 for the (a) stable and (b) unstable boundary layer using the proposed scheme (solid line), the ME BDF scheme without temporal filter (dash-dotted line), and the scheme (g) of KK88 (dotted line). Numbers next to the lines show Δz. The reference solution is shown by the dashed line. For all lines, $\Delta t = 1{,}800$ s except for the one shown as $\Delta t = 600$ s.

The above schemes (the proposed scheme with and without the temporal filter and the scheme (g)) are now applied on the diffusive system again, but this time by using GD90 linearized method mentioned and discretized in Section 4.1, for further analysis. The results are illustrated in Fig. 4.10 including the wind and potential temperature profile. It clearly shows that the proposed scheme results using GD90 approach are in acceptable agreement with the exact solution, while the results of the scheme (g) with one-third the time step used for the proposed scheme are entirely erroneous. It proves the consistency of the proposed scheme in that it is much more compatible with different numerical approaches such as the one used in GD90 study.

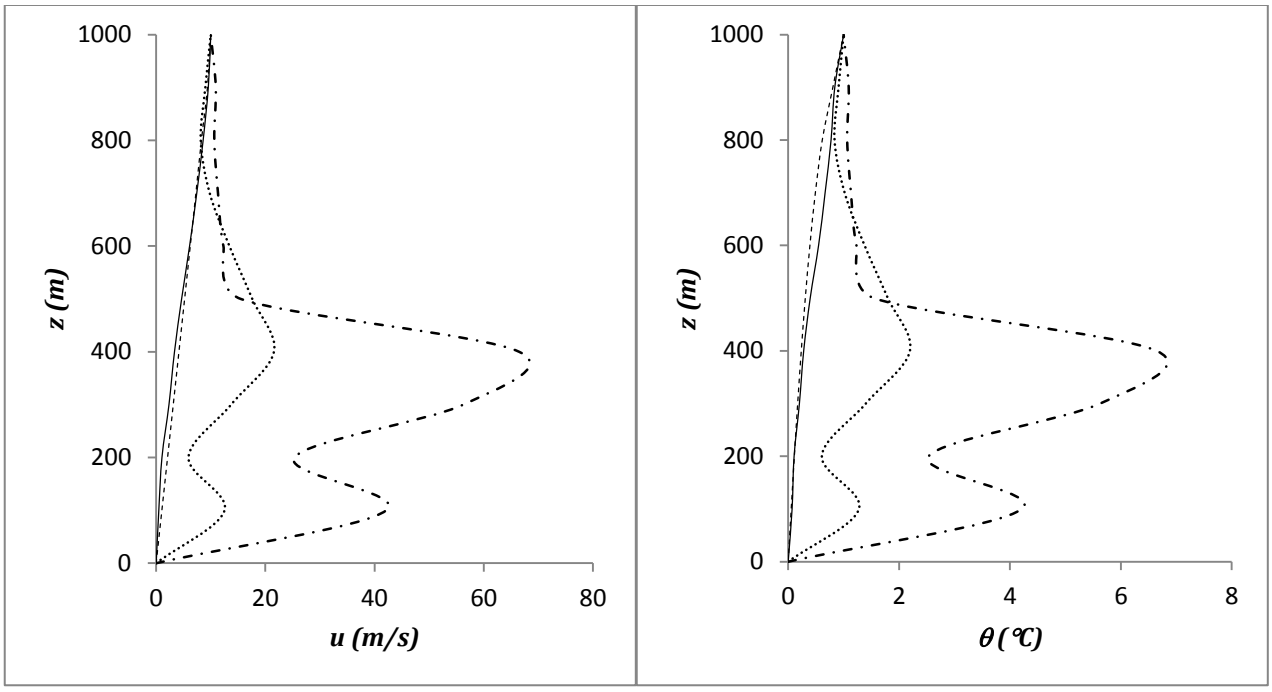

Fig. 4.10. Wind and potential temperature profile after 4 hours for the idealized case described in Section 4.2 for the stable boundary layer using the proposed scheme (solid line), the ME BDF scheme without temporal filter (dash-dotted line), and the scheme (g) of KK88 (dotted line) with GD90 approach. The reference solution is shown by the dashed line. $\Delta t = 1{,}800$ s except for the scheme (g) with $\Delta t = 600$ s.

As a subject for future study, moisture will be added to the system in order to examine the performance of the scheme in that circumstance. Furthermore, other implicit Runge-Kutta schemes, such as TVD Runge-Kutta methods, will be analyzed and compared.

4.5 Conclusion

A semi-implicit Modified Extended BDF scheme was proposed which is highly stable and efficient to apply. It maintains A- and B-stability properties and leads to negligible errors for a wide range of nonlinearity. The scheme was first applied to a commonly used nonlinear ordinary differential equation for atmospheric boundary layers, and good results were obtained. It greatly improves the stability and accuracy of

the numerical results. Unlike previous schemes, it is highly non-sensitive to the time step size while being easy and efficient to implement.

The scheme was further analyzed for nonlinear diffusion systems which have a diffusion coefficient commonly used in atmospheric boundary layer studies. It showed good performance for this case as well. Stability, accuracy of results, and high non-sensitivity to spatial and temporal resolution are the interesting features of the proposed method along with the compatibility with diverse numerical approaches. Moreover, as a result of the proposed modifications, the method is computationally inexpensive.

Acknowledgement

The research was supported by Environment Canada and Natural Sciences and Engineering Research Council of Canada.

5. On Strong-Stability-Preserving Singly-Diagonally-Implicit Runge-Kutta Schemes for Time Integration of Nonlinear Damping (ODE) and Diffusion (PDE) Equations [2]

Abstract

Nonlinear damping and diffusion incorporated in the turbulent mixing of atmospheric boundary layer is dealt with in this study using optimally stable *singly-diagonally-implicit Runge-Kutta* (SDIRK) methods, which have been proved to be effective and computationally efficient for the mentioned challenges in the literature. Various aspects of these schemes, including stability properties, linear stability analysis, and numerical experiments, are studied with regard to their applications for the time integration of well-known nonlinear damping and diffusive systems in atmospheric boundary layer models. Two *modified extended backward differentiation formulae* (ME BDF) SDIRK schemes, which are the modified versions of the optimal SDIRK schemes, are then proposed to improve their stability and numerical features. They exhibit significant improvements with respect to the schemes studied. At the end, the proposed schemes are implemented in an *E-l* turbulence model and the results are satisfactory.

Keywords: Ground temperature · Nonlinear diffusion · Numerical stability · Strongly stable schemes · Turbulent mixing

5.1 Introduction

Nonlinearity and stiffness associated with the *atmospheric boundary layer* (ABL) diffusion processes demand extensive studies on numerical integration methods. Boundary layer properties including temperature, moisture, and momentum are often

[2] Farshid Nazari, Abdolmajid Mohammadian, Martin Charron, and Ayrton Zadra, "On strong-stability-preserving singly-diagonally-implicit Runge-Kutta schemes for time integration of nonlinear damping (ODE) and diffusion (PDE) equations", International Journal for Numerical Methods in Engineering, Under Review.

parameterized via a nonlinear diffusion equation with an exchange coefficient related to the wind shear and static stability (Richardson number) (Girard and Delage, 1990 [GD90 hereafter]; Siebesma et al., 2007; Janiskova et al., 1999). Nonlinearities introduced by these parameterizations can cause several specific numerical problems (Teixeira et al., 2007).

This study focuses on the performance of a class of Runge-Kutta methods which possess specific nonlinear stability characteristics distinguished by the terms *strongly stable* or *monotonic*, for the solution of nonlinear damping and diffusion equations in the ABL. The numerical applications consist of commonly used ground-air heat/moisture exchange and wind/potential temperature diffusion processes. A scheme is defined to be strongly stable or monotonic when it satisfies the condition

$$\|y_{n+1}\| \leq \|y_n\| \tag{5.1}$$

in the march from the time step n to n+1, in the numerical integration of the following *ordinary differential equation* (ODE) initial value problem

$$\dot{y}(t) = f(t, y), \quad y(t_0) = y_0 \,. \tag{5.2}$$

Specifically, the property (5.1) is of particular prominence for the solution of nonlinear parabolic partial differential equations such as the diffusion equation, as semi-discretized parabolic equation gets the form of Eq. (5.2); monotonic numerical methods are considered as a powerful tool for the solution of these challenging problems; see e.g. Shu and Osher (1988), LeVeque (2002), Higueras (2005). Strong stability of the numerical time integrator has been proved to be essential to prevent spurious oscillations caused by the spatial discretization in a partial differential equation (Gottlieb et al., 2009).

Singly-diagonally-implicit Runge-Kutta (SDIRK) methods possess the advantages of implicitness while they are computationally efficient in comparison with fully coupled multi-stage implicit methods. In other words, each stage in SDIRK methods can

be solved independently, which brings about computational efficiency (Nazari et al., 2013). Optimally monotonic SDIRK schemes have been studied by Ferracina and Spijker (2007) with certain stages s and order of p in order to preserve the strong stability property of the schemes for as large a time step as possible. In this paper, optimal SDIRK methods up to 3 stages are studied and analyzed for the solution of nonlinear ordinary differential damping equations representing surface heat or moisture transfer as well as nonlinear partial differential diffusion equations of wind velocity and potential temperature in the ABL. The stability properties plus linear stability analysis of the schemes for both systems of equations are presented. Afterwards, the numerical solution results are illustrated, and finally, in order to obtain more stable and consistent results, two SDIRK methods are proposed, and their properties are revealed.

5.1.1 Optimal SDIRK methods

Multi-stage optimally monotonic SDIRK methods with various orders of accuracy are listed in Table 5.1 (Ferracina and Spijker (2007)). In this paper, studying these optimal methods is limited to schemes with the number of stages up to three and orders of accuracy of two and three. These methods are demonstrated by their coefficient matrices $A = a_{ij}$, with $i \leq s$ and $j \leq s$, where s is the number of stages. Multi-stage Runge-Kutta schemes and the corresponding numerical procedures plus the Butcher tableaus of the optimal schemes and their stability properties are presented in the Appendix.

5.2 Air-Ground Heat Exchange System

In this section, a commonly used nonlinear damping equation representing air-ground heat exchange, is considered for stability and accuracy analysis (Kalnay and M. Kanamitsu, 1988 [KK88 hereafter])

$$\frac{\partial X}{\partial t} = -KX^P X + S\,, \tag{5.3}$$

Table 5.1. Optimal SDIRK schemes coefficients

Optimal SDIRK methods of order $p = 2$	**Coefficients**
1-stage (implicit midpoint rule)	$a_{11} = 1/2$, $b_1 = 1$
2-stage	$a_{11} = a_{22} = 1/4$ and $a_{21} = b_1 = b_2 = ½$
3-stage	$a_{ij} = 1/6$ for $i = j$, $1 \le i \le s$, $a_{ij} = 1/3$ for $1 < j < i \le s$, and $b_i = 1/3$ for $1 \le i \le s$
Optimal SDIRK methods of order $p = 3$	**Coefficients**
2-stage	$a_{11} = a_{22} = \frac{3-\sqrt{3}}{6}$, $a_{21} = \frac{1}{\sqrt{3}}$, and $b_1 = b_2 = \frac{1}{2}$
3-stage	$a_{11} = a_{22} = a_{33} = \frac{1-\sqrt{1/2}}{2}$, $a_{21} = a_{31} = a_{32} = \frac{1}{\sqrt{8}}$, and $b_j = 1/3$ for $1 \le i \le s$

where X represents the temperature difference between the ground and air, $K$and P are constants in the exchange coefficient term (KX^P), and S represents all slowly varying processes such as solar radiation. One approach for the solution of this nonlinear equation is to treat it fully implicitly, which means that X^P and X on the right-hand side are considered at the new stage. This approach is very computationally expensive and it is not worth applying. An alternative approach is to treat the exchange coefficient semi-implicitly in order to avoid both the explicit method disadvantages and the expensive computational cost of the fully implicit method. As a demonstration of the method, the solution of the equation using SDIRK (1,2) is followed. Other SDIRK schemes will be applied similarly. For further details of the implementation of more complicated schemes, refer to Nazari et al. (2013).

SDIRK (1,2): According to the implementation of a multi-stage Ruge-Kutta scheme explained in the Appendix,

$$k_1 = -KX_n^P X_1 + S_1\,, \tag{5.4}$$

where X_1 is the value of X at the first stage, which is at t_n+$\Delta t/2$ for this scheme, and k_1 is the corresponding rate of change of X for the first stage. Thus

$$X_1 = X_n + \frac{1}{2}k_1.\Delta t\,. \tag{5.5}$$

Then, according to the SDIRK (1,2) coefficients, X_{n+1} at the new time step can be obtained by

$$X_{n+1} = X_n + k_1.\Delta t\ . \tag{5.6}$$

The procedure for other schemes is the same. For all the schemes, the value of the variable at the previous stage is used in the exchange coefficient. For instance, for SDIRK (2,2), X_1 is used in the exchange coefficient to calculate k_2.

5.2.1 Linear stability analysis

If the temperature is assumed to be close to the equilibrium value (X_e), then

$$X = X_e + \delta X\ , \tag{5.7}$$

where $X_e^{P+1} = S/K$. Replacing (5.7) in (5.3) and keeping the linear terms versus δX, we obtain

$$\frac{\partial \delta X}{\partial t} = -KX_e^P(P\delta X + \delta X)\ . \tag{5.8}$$

It should be noted that the first linearised term in parentheses corresponds to the exchange coefficient KX^P, and the second term corresponds to the temperature term X. This is very important in the subsequent stability analyses.

The stability analysis of SDIRK (1,2) is performed as follows. More details on this analysis can be found in Nazari et al. (2013).

SDIRK (1,2): Similar to Eq. (5.5),

$$\frac{\delta X_1 - \delta X_n}{\Delta t} = -\frac{1}{2} K X_e^P (P\delta X_n + \delta X_1) = \frac{1}{2} k_1 \,. \tag{5.9}$$

Defining $\alpha = K X_e^P \Delta t$ and amplification factor $\rho = \frac{\delta X_{n+1}}{\delta X_n}$ and rearranging the equation, one obtains

$$\frac{\delta X_1}{\delta X_n} = \frac{1 - \frac{1}{2}\alpha P}{1 + \frac{1}{2}\alpha} \,. \tag{5.10}$$

According to Eq. (5.6),

$$\frac{\delta X_{n+1} - \delta X_n}{\Delta t} = -K X_e^P (P\delta X_n + \delta X_1) = k_1 \,. \tag{5.11}$$

Hence, the amplification factor is

$$\frac{\delta X_{n+1}}{\delta X_n} = 1 - \alpha \frac{1 + P}{1 + \frac{1}{2}\alpha} \,. \tag{5.12}$$

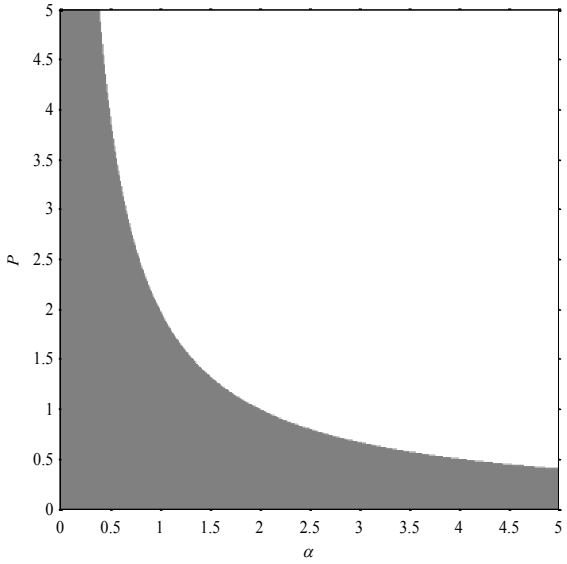

SDIRK (1,2)

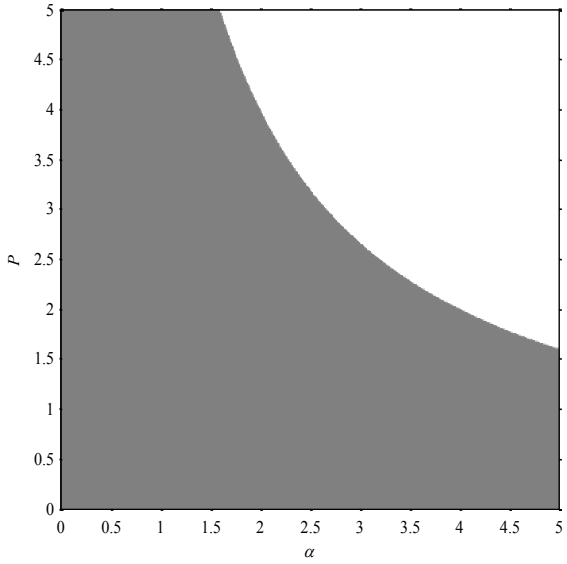

SDIRK (2,2)

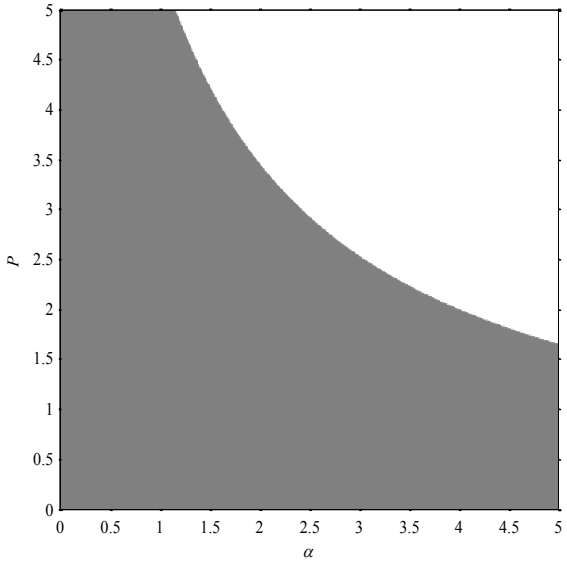

SDIRK (2,3)

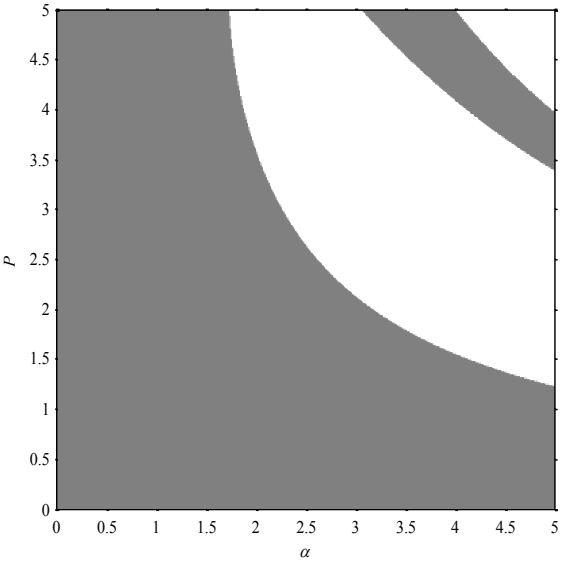

SDIRK (3,2)

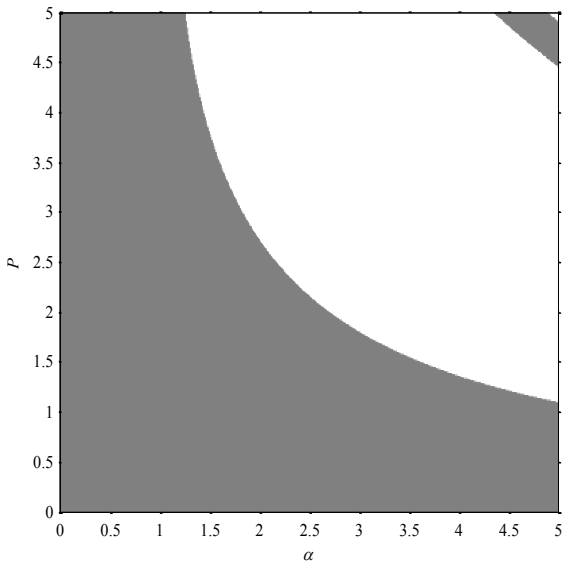

SDIRK (3,3)

Fig. 5.1. Stability limits of SDIRK methods. The first number in parentheses shows the number of stages, and the second number shows the order of accuracy.

The procedure is the same for other SDIRK schemes. In order to have a stable and convergent solution, the amplification factor should lie between $-1 < \rho < 1$. However, if $0 < \rho < 1$, the solution will be damped monotonically, and if $-1 < \rho < 0$, the solution will have an oscillatory damping form. Various nonlinear time integration schemes up to two-time-level were discussed by KK88. They showed that for $\rho > 1$, a spurious behaviour is obtained and the methods lead to a false solution, while for $\rho < -1$, large amplitude oscillations occur. The schemes studied here demonstrate diverse behaviours with regard to linear stability. Referring to Fig. 5.1, where the stability region is the dark area separated from the instability region by the line representing $|\rho| = 1$, SDIRK schemes with the same number of stages show fairly similar attitudes, where ostensibly the stability region is roughly wider for lower orders of accuracy. Note that the stability criterion is related to the power P in addition to the usual stability parameter α. Fig. 5.1 shows that the linear stability behaviour of SDIRK schemes is not substantially related to the number of stages and the formal order of accuracy, since higher stages or higher orders do not guarantee improved stability.

5.2.2 Numerical solutions

The numerical integration of the temperature equation is performed using an SDIRK scheme. To solve the equation, S is assumed to be similar to KK88

$$S_n = 1 + \sin\left(\frac{2\pi t}{20}\right), \tag{5.13}$$

where $t = n\Delta t$ is the time. Similar to KK88, $K = 10$, but Δt is variable in order to examine scheme stability and accuracy. A highly nonlinear case of $P = 4$ is considered here. The results of various SDIRK schemes for $\Delta t = 0.5$ are shown in Fig. 5.2. They are compared to second-order fully implicit Crank-Nicolson scheme results as the reference solution (dotted line). From Fig. 5.2, the best performance is observed for *s*=2-stage SDIRK schemes where good agreement exists between these schemes' solutions and the reference solution. Furthermore, no oscillations or phase shift occur. Similar to Sec. 2.1, SDIRK schemes of the same stage demonstrate analogous behaviours. S = 3-stage SDIRK schemes also show fairly good agreement with the reference solution; however, at the peak, SDIRK (3,2) underestimates the exact solution, whereas SDIRK(3,3) overestimates. Furthermore, both schemes show a slight phase lag (look at the peaks' positions). SDIRK (3,3) is around the limit of instability, considering the peak solution $X \cong 0.7$, which leads to $\alpha \cong 1.2$. As a result, SDIRK (1,2) is placed in the instability region causing the oscillatory results in Fig. 5.2. Notice that the oscillations are bounded within two limits. Oscillations are not desirable in the solution of a scheme in that they expose the scheme to stability issues. In Fig. 5.3, the same schemes are compared for $\Delta t = 1$. It is obvious that increasing the time step reduces the accuracy of the results, but the purpose is to examine the consistency of the schemes' behaviours. Again, the best performance is for *s*=2-stage SDIRK schemes, regarding the accuracy and non-oscillatory results. Although these schemes enter the instability region with $\alpha \cong 3.6$, they are able to damp the oscillations and avoid the instability problems. S = 3-stage schemes are most sensitive to the time step size among

the schemes in this study. Doubling the time step has placed the *s*=3-stage SDIRK schemes into the unstable region,

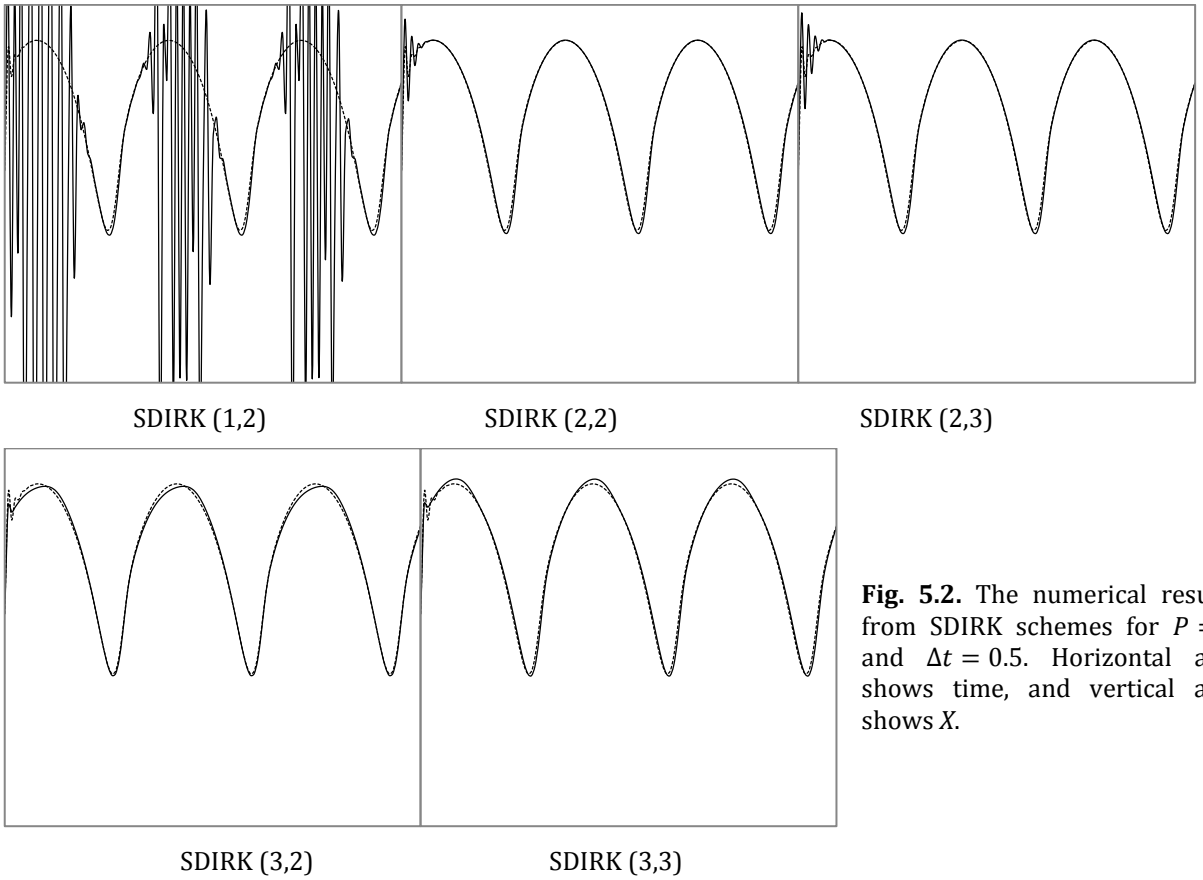

Fig. 5.2. The numerical results from SDIRK schemes for $P = 4$ and $\Delta t = 0.5$. Horizontal axis shows time, and vertical axis shows *X*.

which causes SDIRK (3,2) to become unstable and SDIRK (3,3) to exhibit large amplitude oscillations which are still bounded. As was expected from its previous performance for $\Delta t = 0.5$, SDIRK (1,2) demonstrates highly oscillatory and erroneous results for $\Delta t = 1$. Although appearing in the instability region, SDIRK (1,2) oscillations are still restricted.

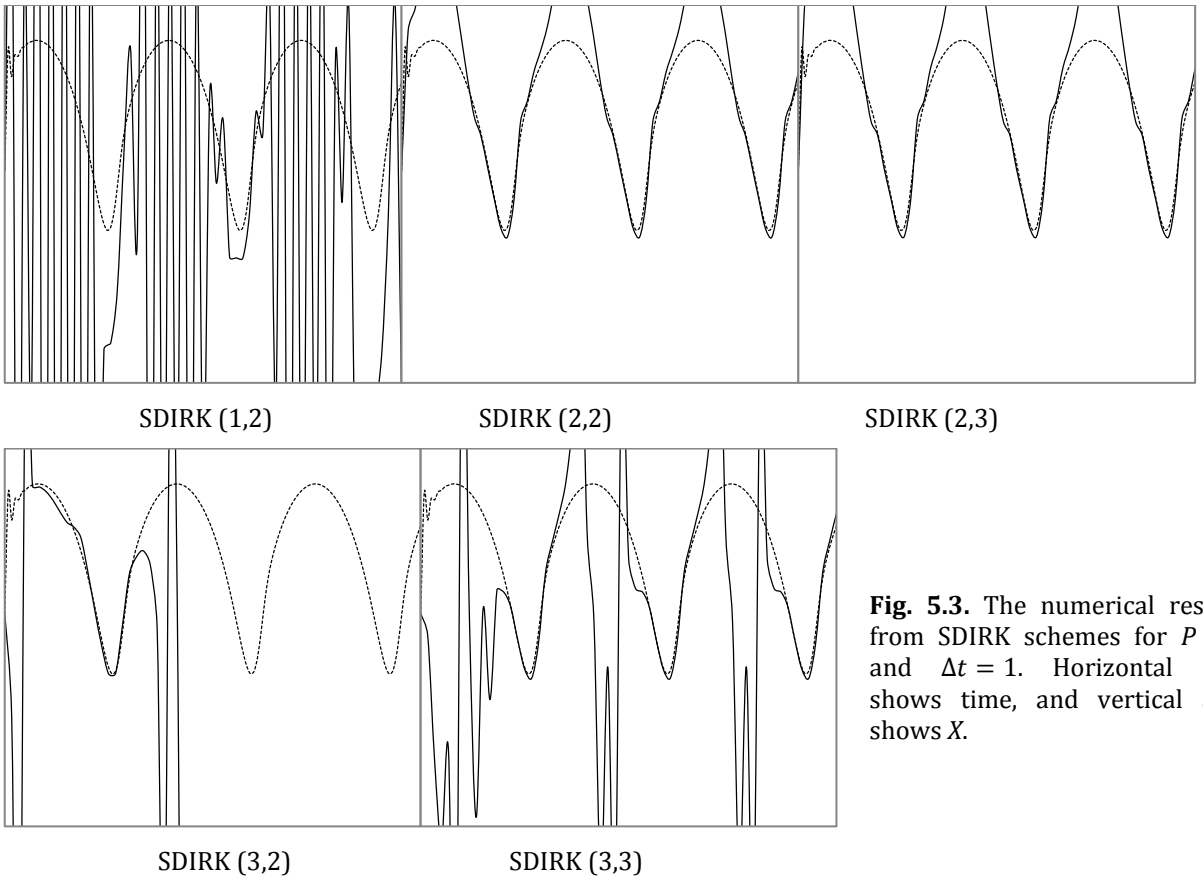

Fig. 5.3. The numerical results from SDIRK schemes for $P = 4$ and $\Delta t = 1$. Horizontal axis shows time, and vertical axis shows X.

5.3 Nonlinear Diffusive System of Wind-Potential Temperature

Nonlinear diffusion equations appear in many applications, including the Navier-Stokes equations, shallow water systems and atmospheric boundary layer equations. As an example of a highly nonlinear diffusive system, in this chapter we consider a commonly used model for atmospheric boundary layers. In this model, two diffusion equations are solved for wind velocity and potential temperature:

$$\begin{aligned} \frac{\partial u}{\partial t} &= \frac{\partial}{\partial z}\left(K\frac{\partial u}{\partial z}\right) \\ \frac{\partial \theta}{\partial t} &= \frac{\partial}{\partial z}\left(K\frac{\partial \theta}{\partial z}\right). \end{aligned} \tag{5.14}$$

Although the diffusion coefficients are generally different for wind and temperature, which has been investigated in some studies (e.g. Benard et al., 2000), they are assumed to be equal in this study and are obtained from the following equation (GD90):

$$K = l^2 \left|\frac{\partial u}{\partial z}\right| (1 + b|Ri|)^n, \qquad \left(\frac{\partial u}{\partial z} \neq 0\right), \tag{5.15}$$

where l is the mixing length, n and b are constants, and Ri is the Richardson number

$$Ri = \frac{g}{\theta_0} \frac{\partial \theta / \partial z}{(\partial u / \partial z)^2} , \tag{5.16}$$

where g is the gravity acceleration and θ_0 is a constant. The mixing length is also variable with the elevation, but it is assumed in this study to be constant.

As the static stability increases, K should gradually vanish, while it grows as the static instability intensifies. To obtain this behaviour, n and b must vary according to stability, and only one of them must change signs when the stability sign changes. As the results of this study will be compared with GD90's study, the same values of n and b are considered, which are

$$\begin{aligned} n = -2; b = 5 \quad for\ Ri > 0 \\ n = \frac{1}{2}; b = 20 \quad for\ Ri < 0\ . \end{aligned} \tag{5.17}$$

5.3.1 Numerical stability analysis

The analytical stability of the system of equations has been established by GD90. They also studied the stability of a class of two-time-level schemes.

Considering explicit diffusion coefficient and implicit velocity, the diffusion Eq. (5.14) can be written as

$$u_t = (Ku_z^+)_z = K_z u_z^+ + Ku_{zz}^+ . \tag{5.18}$$

The plus sign designates the next time step. GD90 showed that K_z is given by

$$K_z = \frac{K(1-2\alpha)}{u_z} u_{zz} + \frac{K\alpha}{\theta_z}\theta_{zz} , \tag{5.19}$$

where

$$\alpha = \frac{nb|Ri|}{1+b|Ri|} . \tag{5.20}$$

Consideration of solutions of the form $u = ce^{\omega t + imz}$ leads to $u^+ = \lambda u$, where λ is an amplification factor and c is a constant. Now, if we replace all terms in Eq. (5.18) using a second-order centered scheme for first- and second-order derivatives in RHS (spatial discretization), we obtain

$$\begin{aligned} u_{1t} &= \left(\frac{K(1-2\alpha)}{\frac{u_{n,j+1}-u_{n,j-1}}{2\Delta z}} \frac{u_{n,j+1}-2u_{n,j}+u_{n,j-1}}{\Delta z^2} \right. \\ &\left. + \frac{K\alpha}{\frac{\theta_{n,j+1}-\theta_{n,j-1}}{2\Delta z}} \frac{\theta_{n,j+1}-2\theta_{n,j}+\theta_{n,j-1}}{\Delta z^2} \right) \frac{u_{1,j+1}-u_{1,j-1}}{2\Delta z} \\ &+ K\frac{u_{1,j+1}-2u_{1,j}+u_{1,j-1}}{\Delta z^2} \end{aligned} \tag{5.21}$$

for the first stage, in which u_1 is the first stage velocity in the Butcher tableau. This discretized equation leads to a tri-diagonal system, which is very computationally efficient to solve. Replacing the discretized terms by their equivalent form ($u_{n,j+1} = u_n e^{im(\Delta z)}$ and $u_1 = \lambda_1 u_n$), we obtain

$$
\begin{aligned}
&u_{1t} \\
&= \left(\frac{2K(1-2\alpha)}{u_n(2isin(m\Delta z))} \frac{u_n(-4sin^2\left(\frac{m\Delta z}{2}\right))}{\Delta z} \right. \\
&\left. + \frac{2K\alpha}{\theta_n(2isin(m\Delta z))} \frac{\theta_n(-4sin^2\left(\frac{m\Delta z}{2}\right))}{\Delta z} \right) \frac{\lambda_1(2isin(m\Delta z))}{2\Delta z} u_n \\
&+ K \frac{-4\lambda_1 sin^2\left(\frac{m\Delta z}{2}\right)}{\Delta z^2} u_n \, .
\end{aligned} \tag{5.22}
$$

Finally,

$$
u_{1t} = \frac{-4Ksin^2\left(\frac{m\Delta z}{2}\right)}{\Delta z^2}(2-\alpha)\lambda_1 u_n \, . \tag{5.23}
$$

For SDIRK(1,2), $k_1 = u_{1t} = \frac{u_1 - u_n}{\frac{1}{2}\Delta t} = \frac{\lambda_1 - 1}{\frac{1}{2}\Delta t} u_n$. Replacing u_{1t} by its equivalent in the above equation gives

$$
\lambda_1 = \frac{1}{1 + \frac{4Ksin^2\left(\frac{m\Delta z}{2}\right)(2-\alpha)\frac{1}{2}\Delta t}{\Delta z^2}} \, . \tag{5.24}
$$

According to the Butcher tableau of SDIRK (1,2), $u_{n+1} = u_n + k_1\Delta t$; which means

$$
u_{n+1} = \left(1 + \frac{\lambda_1 - 1}{\frac{1}{2}\Delta t}\Delta t \right) u_n \, . \tag{5.25}
$$

Hence,

$$\lambda = 1 + 2(\lambda_1 - 1), \tag{5.26}$$

where λ is the amplification factor for the SDIRK (1,2) scheme. Likewise, amplification factors for other SDIRK schemes can be obtained (see Nazari et al. (2013) for more details).

The amplitude A of a wave of length $\gamma = \frac{2\pi}{m}$, diffused by coefficient K as a function of time for various spatial resolutions, is given by (GD90)

$$A(m\Delta z, t) = exp\left[-m^2 Kt(2-\alpha)\frac{sin^2\left(\frac{m\Delta z}{2}\right)}{\left(\frac{m\Delta z}{2}\right)^2}\right]. \tag{5.27}$$

This amplitude is free of temporal truncation error. The ratio r is defined as follows, representing the reduction in numerical amplitude over the analytical one:

$$r = \frac{1-\lambda}{1-A(0,\Delta t)}. \tag{5.28}$$

The case $r < 1$ results in underestimation of the analytical diffusion, and $r > 1$ results in excessive numerical diffusion. The r ratio of the previously mentioned SDIRK schemes is shown in Fig. 5.4. Obviously, all the SDIRK schemes except for SDIRK (2,2) (which was expected, referring to Fig. 5.3 for the nonlinear damping equation with $\Delta t = 1$) are linearly unstable when the time step is increasing. SDIRK (1,2) shows behaviour similar to implicit schemes until $K\Delta t/\gamma^2 \geq 10^{-1.8}$, when the numerical diffusion rises abruptly, and the *r* ratio will be around 2 at the end. SDIRK (2,3) shows poorer behaviour as the time step increases where the *r* ratio eventually falls and it continues to grow in the negative direction. SDIRK schemes with *s* = 3-stage exhibit similar behaviour. Their performances are similar to implicit schemes for $K\Delta t/\gamma^2 \leq 10^{-1.5}$, while after that the *r* ratio abruptly increases, showing too much numerical diffusion. SDIRK (2,2), however, shows the damping *r* ratio, which means that the

numerical diffusion tends to disappear when the time step increases. All the schemes demonstrate more accuracy for higher spatial resolutions with smaller time steps; nevertheless, there is not a significant difference among different spatial resolutions when the time step is large. The waves of length $2\Delta z$ (lowest spatial resolution) lead to the largest error in the region of small Δt values.

5.3.2 Application

An idealized case similar to GD90 is considered in order to compare our results with their study. The problem specifications are:

- K is obtained from Eqs. (5.15) and (5.17) with $l = 50$ m
- Boundary conditions are $u = 0$ m s^{-1} and $\theta = 0$ ℃ at $z = 0$, and zero gradient at $z = 1000$ m
- Initial conditions are $u = 10$ m s^{-1}, and θ varies linearly with z from 0 ℃ to 1 ℃.

According to GD90, the vertical resolution should be chosen very carefully for two reasons: 1) the traditional schemes for vertical diffusion in NWP models may cause oscillatory, inaccurate results if the vertical resolution is higher than a specific limit; and 2) an unwanted delay may occur in the solution, since K is calculated explicitly and the atmospheric flow propagation from the high K-value region to the low K-value region (boundary layer to free atmosphere) can take place at a maximum rate of one grid point per time step.

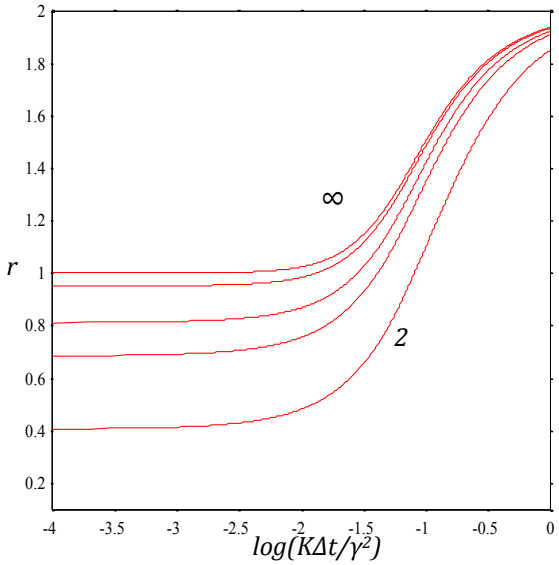

SDIRK (1,2)

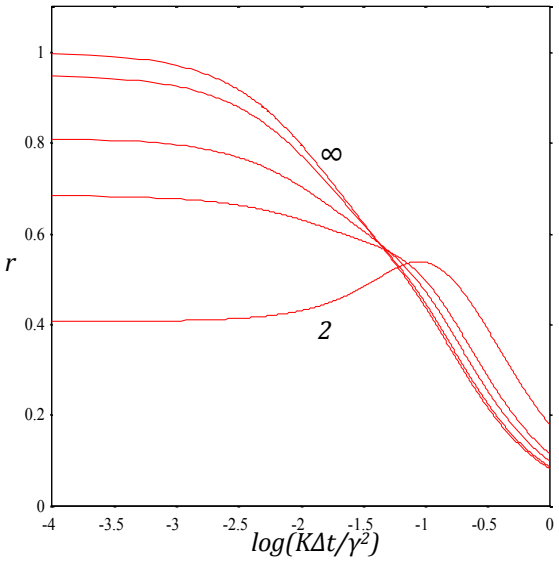

SDIRK (2,2)

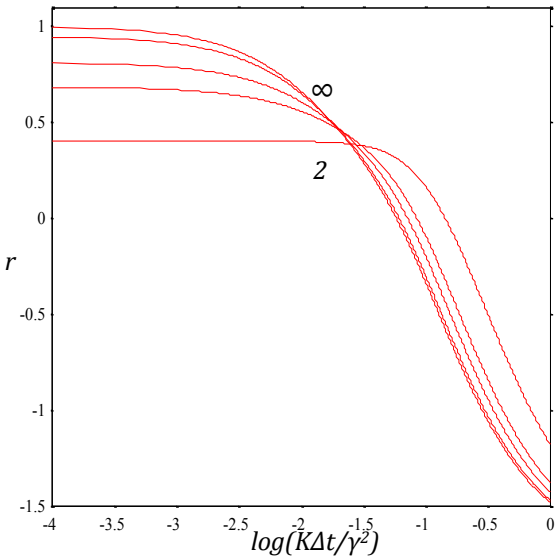

SDIRK (2,3)

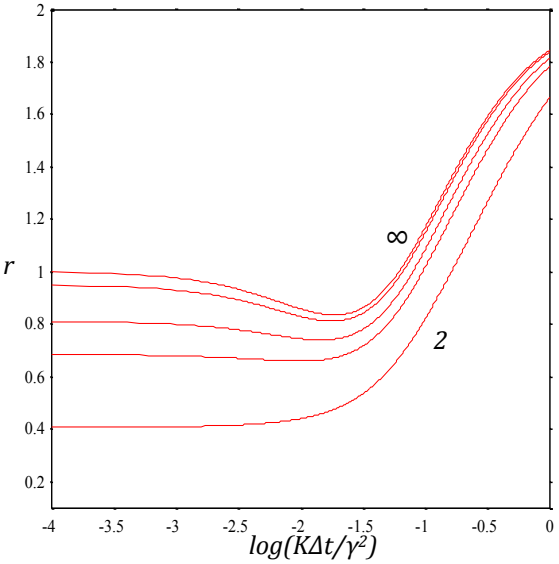

SDIRK (3,2)

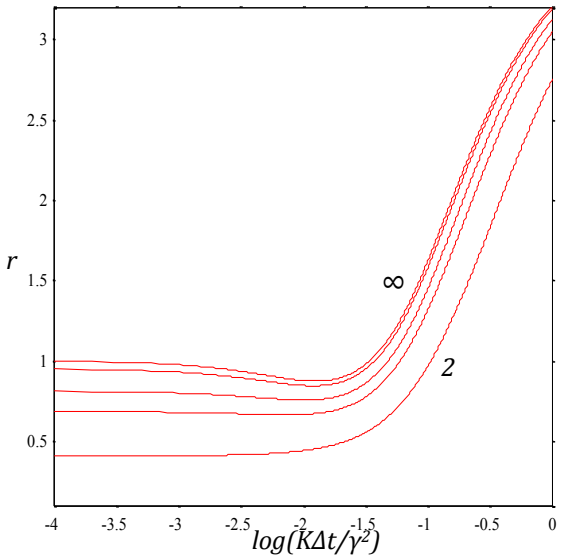

SDIRK (3,3)

Fig. 5.4. The ratios of reduction of numerical amplitude to that of the analytical one (r) for the SDIRK schemes. The numbers on the graphs show $\gamma/\Delta z$ representing spatial resolutions.

The calculated wind profiles using SDIRK schemes are shown in Fig. 5.5 for the stable boundary layer for two vertical resolutions and with the same time step size as GD90: $\Delta t = 1800$ s.

At first glance, all the schemes except SDIRK (1,2) are capable of reproducing the reference solution calculated using the traditional first-order implicit scheme (which includes explicit diffusion coefficient and implicit variable) with a very fine grid and $\Delta t = 120$ s (dotted line). All the schemes except for SDIRK (1,2) show similar behaviour for $\Delta z = 100$ m, with non-oscillatory results in good agreement with the reference solution. Decreasing Δz to 40 m (2.5 times higher spatial resolution), however, can reveal the differences between the schemes' behaviors. As can be seen in Fig. 5.5, the SDIRK (1,2) results are totally erroneous. The results are also very sensitive to spatial resolution, as are the results for SDIRK (2,3) and SDIRK (3,3) schemes, as the wind is not numerically diffused properly at all with large amplitude oscillations for $\Delta z = 40$ m. Unlike the nonlinear damping equation solutions in Sec. 2, schemes with the same number of stages do not exhibit the same behaviour for the nonlinear diffusive system. SDIRK schemes of higher order are prone to instability issues with increased spatial resolution, whereas SDIRK schemes with the formal order of accuracy $p = 2$ are less sensitive to spatial resolution. SDIRK (2,2)'s behaviour was

expected, regarding the linear stability results in Sec. 2.1. SDIRK (3,2) had also shown less r ratio with respect to SDIRK (3,3) as the time step increases.

5.4 The Proposed SDIRK Schemes

In this section, two SDIRK schemes are proposed by extending the current SDIRK (1,1) and SDIRK (1,2) methods, where the former is in fact the traditional implicit scheme, in order to improve SDIRK scheme performance in various situations while preserving computational efficiency.

The first proposed scheme is obtained using the traditional first-order implicit scheme for two time steps, and then, an arithmetic combination of the solutions at times n, n+1, and n+2 is considered in a way that the final solution takes place at time n+1 (i.e. $X_{n+1} = \frac{1}{2}[X_1 + \frac{1}{2}(X_n + X_2)]$ for the ODE system in Sec. 2; likewise for Sec. 3). The coefficient matrix A, hence, consists of $a_{ij} = 1$, $j \le i = 1, 2$, $b_1 = 3/4$, and $b_2 = 1/4$. This scheme is shown by PSDIRK (1) hereafter.

Another proposed scheme, PSDIRK (2), in this paper applies SDIRK (1,2) for 2 time steps and then takes the average of steps n+1 and n+2. As a result, the coefficient matrix A includes $a_{11} = a_{22} = 1/2$, $a_{21} = 1$, $b_1 = 3/4$, and $b_2 = 1/4$. Now, the analyses from the previous sections are performed for these schemes. A- and B-stability properties are as follows.

As illustrated in Fig. 5.6.a, PSDIRK (1) and PSDIRK (2) are A-stable in the whole domain except for the small area shown. Matrix M corresponding to B-stability is $M = \begin{bmatrix} 0.9375 & 0.0625 \\ 0.0625 & 0.4375 \end{bmatrix}$ with the eigenvalues 0.4298 and 0.9452 for PSDIRK (1) and $M = \begin{bmatrix} 0.1875 & 0.0625 \\ 0.0625 & 0.1875 \end{bmatrix}$ with the eigenvalues 0.125 and 0.250 for PSDIRK (2). Considering $b > 0$, we conclude that both proposed schemes are also B-stable. Detailed explanation about A- and B-stability, and the Butcher tableaus of the proposed schemes are presented in the Appendix.

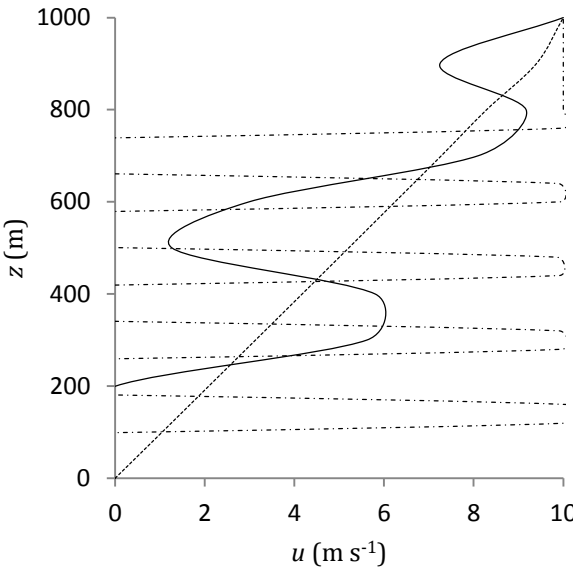

SDIRK (1,2)

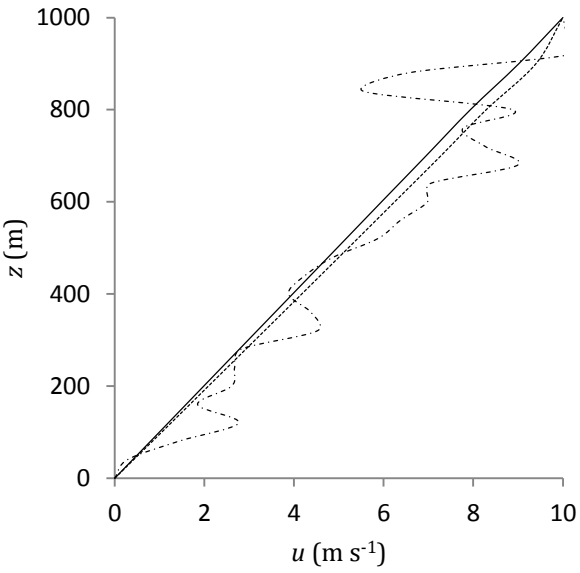

SDIRK (2,2)

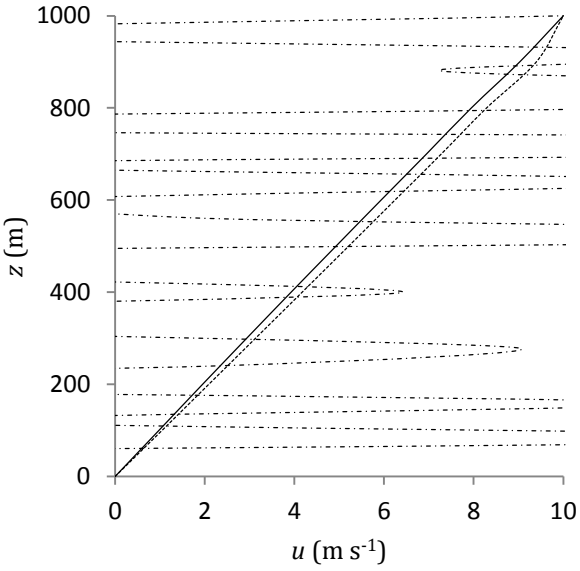

SDIRK (2,3)

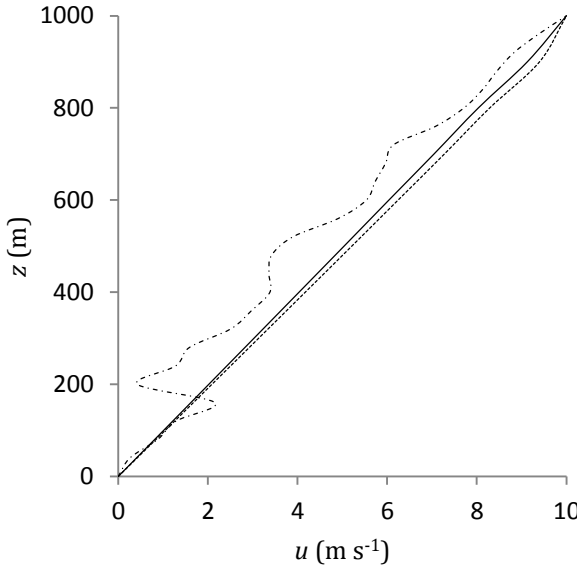

SDIRK (3,2)

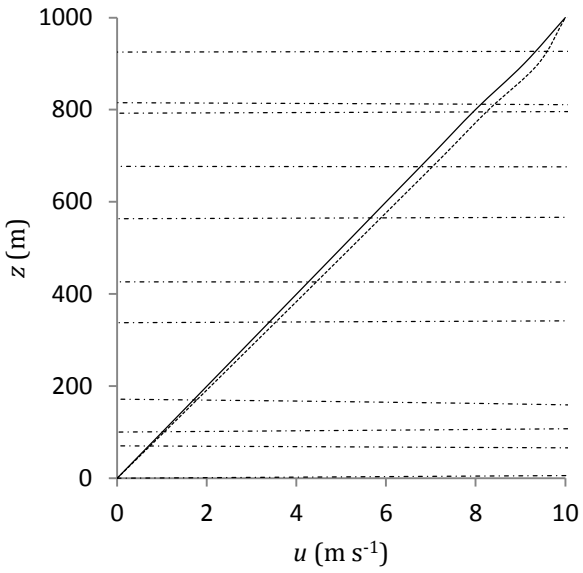

SDIRK (3,3)

Fig. 5.5. Wind profiles after 4 hours for two vertical resolutions for the idealized case described in Sec. 3.2 for the stable boundary layer using SDIRK schemes. $\Delta z = 100$ m is shown by a solid line and $\Delta z = 40$ m is shown by a dash-dotted line. The reference solution is shown by the dotted line. For all lines, $\Delta t = 1800$ s.

So far, the proposed schemes have demonstrated potential to be appropriate for nonlinear equations. Linear stability analysis results, similar to Sec. 2.1, are shown in Fig. 5.6.b. They show a large stability domain with respect to the previously mentioned SDIRK schemes. Numerical solutions of the nonlinear damping Eq. (5.3) using the proposed SDIRK scheme are shown in Fig. 5.6.c. The results are in very good agreement with the exact solution, even for $\Delta t = 1$, where there is a small discrepancy between the two solutions.

The response functions, $\frac{\delta X(t_{n+1})}{\delta X(t_n)}$, of the schemes to the nonlinear problem of Eq. (5.3) are illustrated in Fig. 5.6.d by using the linear perturbation analysis in Sec. 2.1. The response functions are compared to the analytical solution of the perturbed problem (5.8),

$$\frac{\delta X(t_{n+1})}{\delta X(t_n)} = e^{-\alpha(P+1)}\,, \tag{5.29}$$

for error analysis. The proposed schemes show far better performances than the SDIRK schemes in previous sections; PSDIRK (1)'s response function is fairly closer to the analytical one than PSDIRK (2)'s.

Moving to the next analysis, the numerical diffusion analysis is shown in Fig. 5.6.e. The performance of the schemes demonstrates an improvement with regard to the SDIRK schemes in the previous sections. The proposed schemes' behaviours are similar to the implicit schemes in GD90's or Nazari et al.'s (2013) proposed schemes. However, PSDIRK (2) shows L-stability, while PSDIRK (1) is not L-stable, inferring excessive numerical diffusion for large time steps. It is worth mentioning that although being L-stable may lead to more accurate solutions for large time steps, numerical diffusion may also be desirable for large time steps, which can damp the oscillations and prevent instability. Finally, applying PSDIRK (1) and PSDIRK (2) schemes on the nonlinear diffusive system in Sec. 3.1 results in the solutions illustrated in Fig. 5.6.f. The results are quite satisfactory, since for higher spatial resolution with $\Delta z = 40$ m and the same $\Delta t = 1800$ s, there is a slight difference from the reference solution, where PSDIRK (2) seems slightly more accurate. Comparing these results to the solutions using the previously mentioned SDIRK methods in Sec. 3.2 highlights the significant improvement in the results. Furthermore, the two proposed schemes are monotonic, as is obvious from the results in Fig. 5.6.f, for both spatial resolutions.

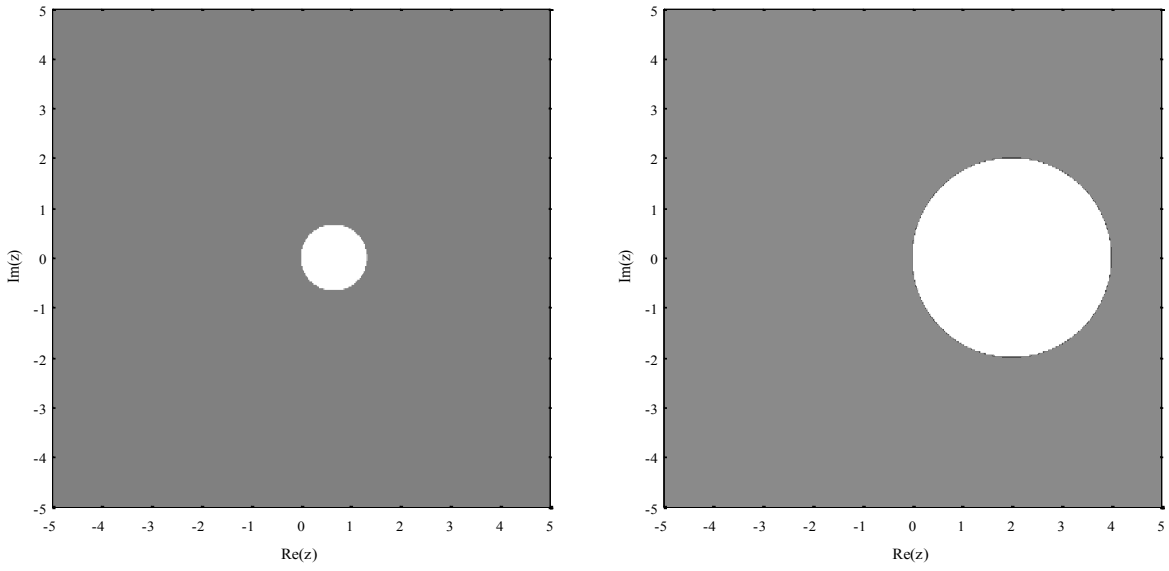

PSDIRK (1) PSDIRK (2)

(a)

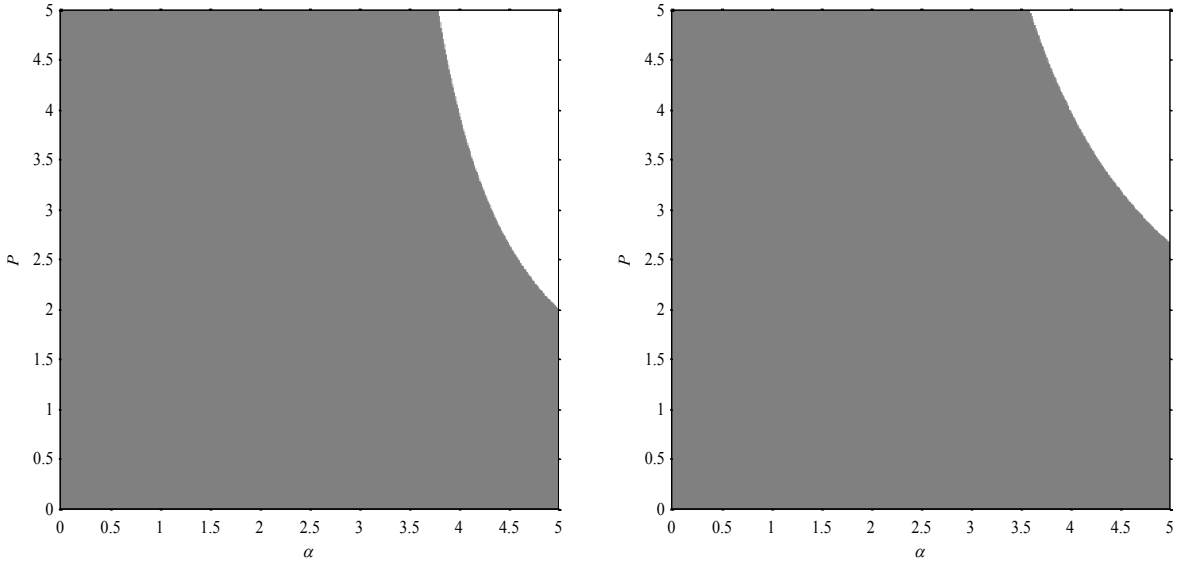

PSDIRK (1) PSDIRK (2)

(b)

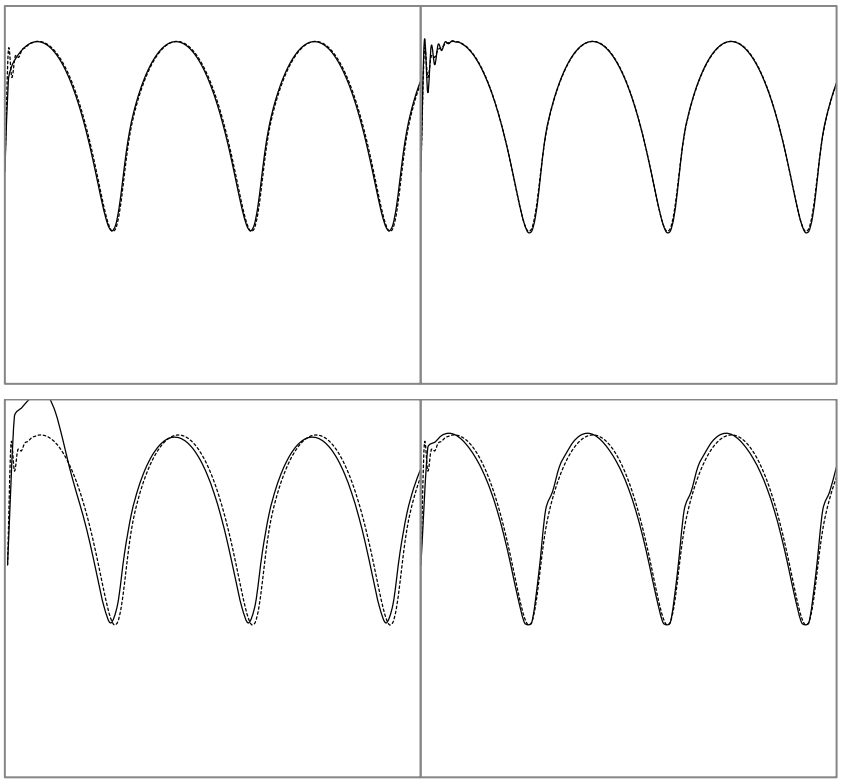

PSDIRK (1) PSDIRK (2)

(c)

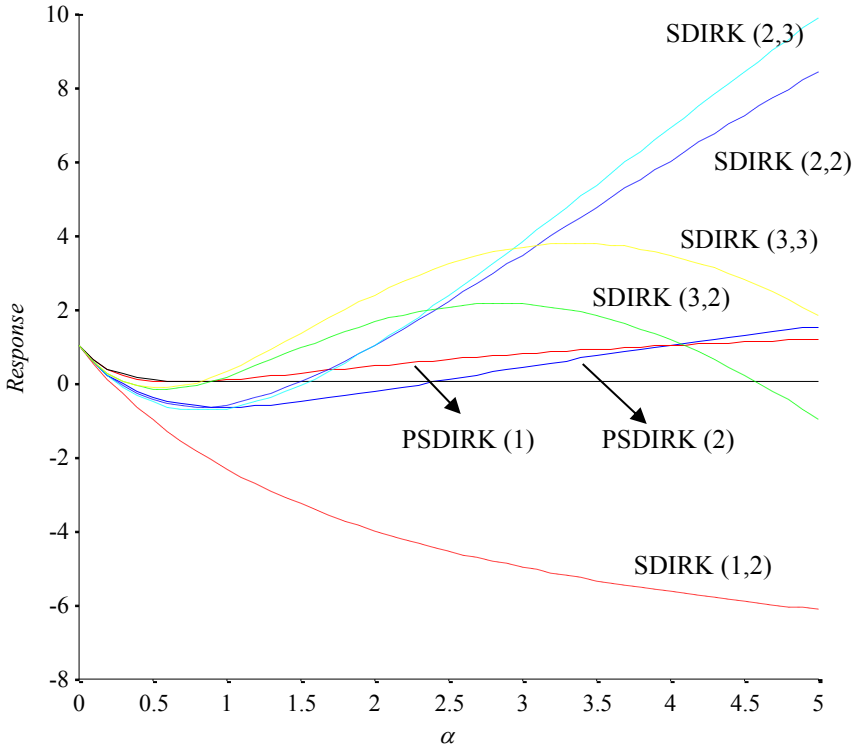

(d)

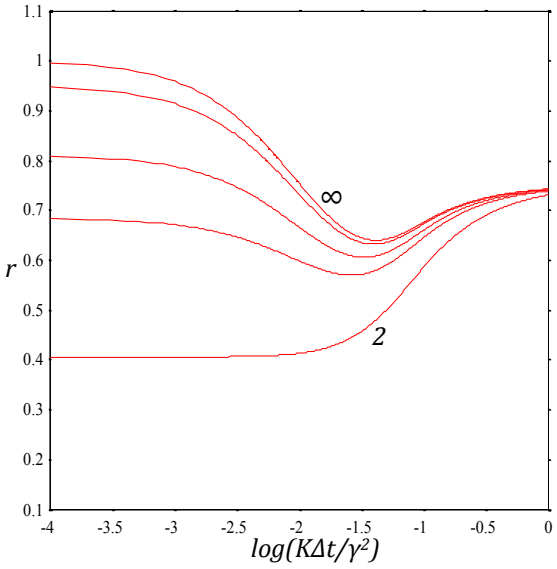

PSDIRK (1)

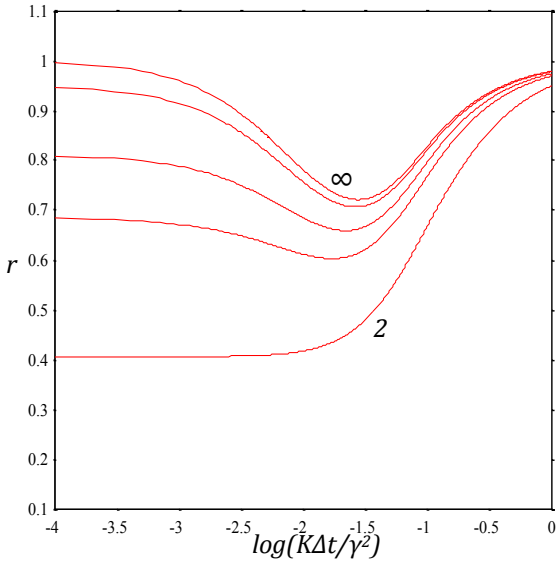

PSDIRK (2)

(e)

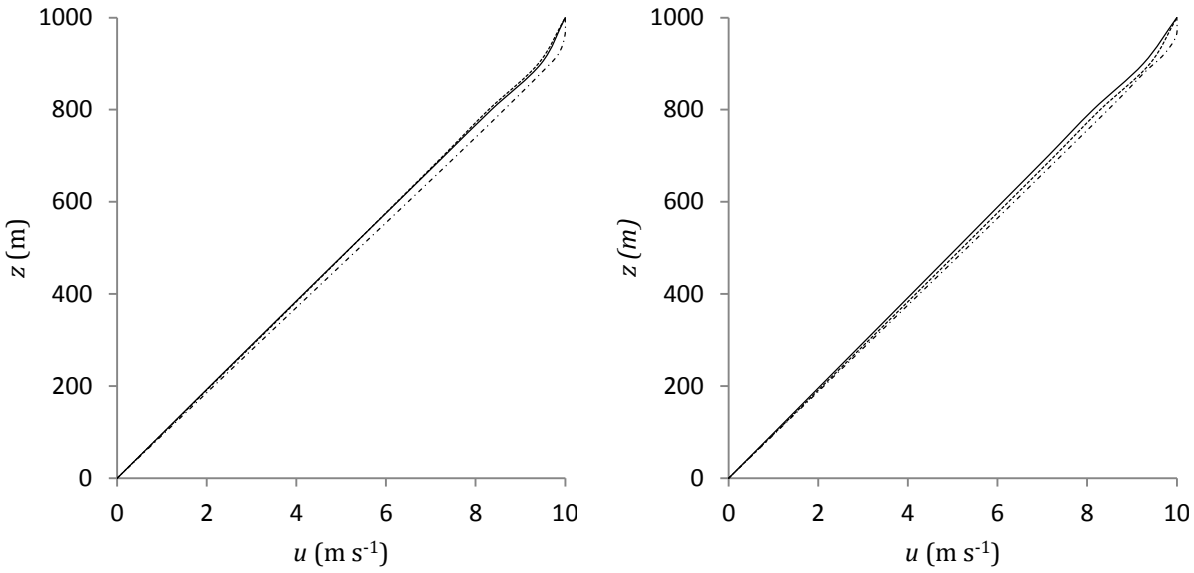

(f)

Fig. 5.6. The proposed PSDIRK (1) and PSDIRK (2) scheme properties: a) Stability region; b) Stability limits for the nonlinear damping equation; c) Numerical solutions of the nonlinear damping equation for $\Delta t = 0.5$ (top) and $\Delta t = 1$ (bottom); d) Response functions of SDIRK schemes compared with the analytic response; e) The ratio of reduction of numerical amplitude to that of the analytical one (r), the numbers on the graphs show $\gamma/\Delta z$ representing spatial resolutions; and f) Wind profile after 4 hours for two vertical resolutions for the idealized case described in Sec. 3.2 for the stable boundary layer: $\Delta z = 100$ m is shown by a solid line, $\Delta z = 40$ m is shown by a dash-dotted line, and the reference solution is shown by the dotted line.

5.5 Diurnal Cycle Simulation by *E-l* Turbulence Closure Scheme

At last, the proposed SDIRK schemes are used as the temporal schemes in the following 1.5-order *E-l* turbulence closure model with a diagnostic length scale to simulate the GABLS second inter-comparison project as a more realistic experiment, based on observations between 23 and 25 of October 1999 from the CASES99 field study in Kansas, USA. The simplified case dominantly forced by the surface potential temperature and the geostrophic wind is studied here.

The diffusive system changes as follows:

$$\frac{\partial u}{\partial t} = \frac{\partial}{\partial z}\left(K_m \frac{\partial u}{\partial z}\right) + f(v - v_g) \tag{5.30}$$

$$\frac{\partial v}{\partial t} = \frac{\partial}{\partial z}\left(K_m \frac{\partial v}{\partial z}\right) - f(u - u_g) \tag{5.31}$$

$$\frac{\partial \theta}{\partial t} = \frac{\partial}{\partial z}\left(K_h \frac{\partial \theta}{\partial z}\right) \tag{5.32}$$

to include the Coriolis effect. K_m and K_h are the momentum and heat eddy diffusivities respectively, f is the Coriolis factor, and u_g and v_g are the geostrophic wind components.

The 1.5-order *E-l* turbulence closure scheme with a diagnostic length scale, similar to that of Andre et al. (1978), is used. The turbulent fluxes are related to the flow vertical gradients via eddy diffusivities which are calculated using the turbulent kinetic energy. Thus, an extra prognostic equation is introduced to calculate the turbulent kinetic energy E with the square of the turbulent velocity scale $q^2 = 2E$:

$$\frac{\partial q^2}{\partial t} = \frac{\partial}{\partial z}\left(K_e \frac{\partial q^2}{\partial z}\right) + 2K_e M^2 - 2K_h N^2 - \frac{2q^3}{16.6l}\,, \tag{5.33}$$

where $K_e = 0.2lq$ is the eddy diffusivity of the turbulent kinetic energy and l is the turbulent mixing length calculated by Blackadar (1962)

$$\frac{1}{l} = \frac{1}{\kappa z} + \frac{1}{\lambda}\,, \tag{5.34}$$

where λ is a limiting mixing length that is generally set to a neutral value, e.g. 40 m. M and N are the Prandtl and Brunt-Vaisala frequencies

$$(M^2, N^2) = \left(\left(\frac{\partial u}{\partial z}\right)^2 + \left(\frac{\partial v}{\partial z}\right)^2, \frac{g}{\theta_0}\frac{\partial \theta}{\partial z}\right). \tag{5.35}$$

Then the turbulent kinetic energy is used to parameterise the eddy diffusivities in Eqs. (5.30)-(5.32), which can be expressed as

$$K_m = lqS_m \tag{5.36}$$

$$K_h = lqS_h \,, \tag{5.37}$$

where S_m and S_h are dimensionless stability functions, which have been parameterised by Galperin et al. (1988) as

$$S_m = \frac{0.393 - 3.085G_h}{1 - 40.803G_h + 212.469G_h^2} \tag{5.38}$$

$$S_h = \frac{0.494}{1 - 34.676G_h} \,, \tag{5.39}$$

where G_h is a function of the Brunt-Vaisala frequency

$$G_h = -\frac{l^2N^2}{q^2} \,. \tag{5.40}$$

Some physically justified constraints are implemented to eliminate numerical errors. A minimum value of 1×10^{-5} m^2 s^{-1}, which corresponds approximately to molecular diffusion, is imposed for the momentum, heat and turbulent kinetic energy diffusivities. A minimum value of 5×10^{-7} m^2 s^{-2} is also imposed upon the turbulent kinetic energy. The model initial and boundary conditions are as follows:

- The initial potential temperature profile is an adiabatic layer with potential temperature 279 K from the surface up to 100 m, above which the air is stable with a constant lapse rate of 0.01 K m^{-1}.

- The wind profiles are set equal to the geostrophic wind magnitudes (10 m s^{-1} in x-direction) initially throughout the boundary layer.
- The initial turbulent kinetic energy profile is decreasing linearly from 0.4 m^2 s^{-2} at the surface to zero at the height of 250 m, at and above which is set to the imposed minimum value.
- No-slip boundary condition is applied at the surface, and at the upper boundary, the wind is forced to its geostrophic value.
- The turbulent kinetic energy is set to a Dirichlet boundary condition at the surface, which is $q_0^2 = B_1^{2/3} u_*^2$ (Mellor and Yamada, 1974), and its minimum value at the top.

The surface friction velocity is

$$u_* = -[(\overline{u'w'})_0^2 + (\overline{v'w'})_0^2]^{\frac{1}{4}} = -\sqrt{K_m \left|\frac{\partial u}{\partial z}\right|} \,. \tag{5.41}$$

The model domain is 2000 m deep and the simulation is run over a period of 48 hours. A Coriolis parameter of $f = 1.39 \times 10^{-4}$ s^{-1} is used corresponding to 73°N, with a surface roughness height of $z_0 = 0.1$ m.

Time-height contour plots of the prognostic variables in the model are shown in Fig. 5.7, which proves that the proposed SDIRK schemes are working well with the *E-l* turbulence closure model. All the boundary layer features including the potential temperature variations during the day-night cycle, nocturnal jet, and turbulent kinetic energy growth early in the morning or at the top of the boundary layer are successfully modeled and are in good agreement qualitatively with other comparable modeling results such as Mellor and Yamada (1974). Contrary to what we see in this study, oscillatory solutions in the regions of rapid potential temperature gradient variation (transition from diurnal to nocturnal layer) have been reported in the literature, e.g, Dunbar and Hanert (2008), in which the oscillations are transmitted above the boundary layer. It is worth mentioning that the diffusion coefficient K is computed

explicitly only once by time-level n values for the mentioned E-l turbulence closure model and can be used in all SDIRK stages. Computing K is often the most expensive part of a vertical diffusion solver. Furthermore, the proposed SDIRK schemes demonstrate high compatibility with spatial and temporal resolutions without showing any instability or oscillation problems. This strength enables us to work with large time steps even for highly spatially resolved models.

5.6 Conclusion

Optimal 2- and 3-stage SDIRK methods with formal orders of accuracy p = 2, 3 were studied from different aspects in order to evaluate the performance of such schemes for the solution of nonlinear damping and diffusion equations commonly applied in atmospheric boundary layer modeling. A- and B-stability properties, linear stability analyses of the nonlinear damping and diffusive system, and numerical experiments prove that none of the SDIRK schemes behaves satisfactorily; however, the 2-stage SDIRK scheme with order p = 2 (SDIRK (2,2)) shows better performance in general. It is B-stable and damps the oscillations, preventing instability problems, although the accuracy of the results is not acceptable. Afterwards, two SDIRK schemes are proposed to alleviate these drawbacks. As was shown in this paper, the proposed schemes PSDIRK (1) and PSDIRK (2) have considerably improved the results. A- and B-stability of the proposed schemes are the reasons for their good performance for the solution of the nonlinear systems with stiff components, which are the sources of many subsequent problems.

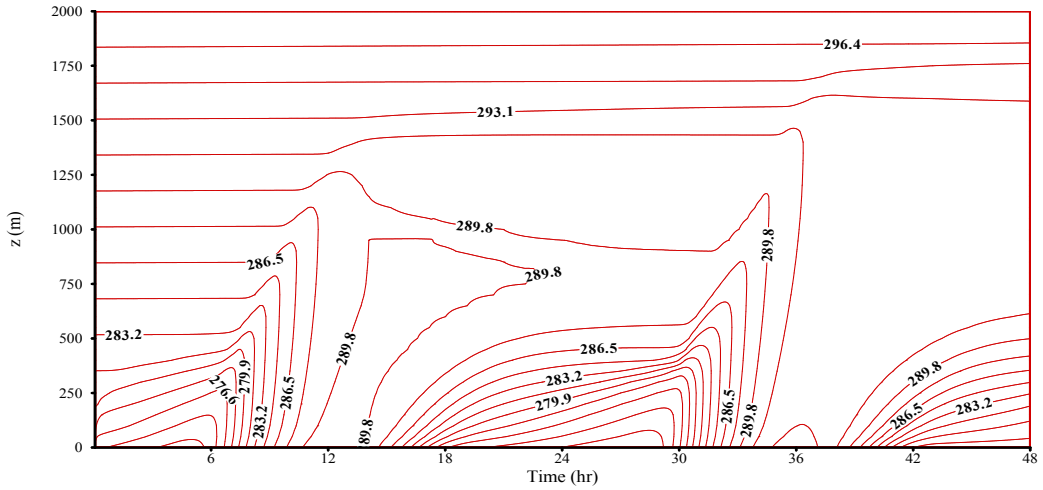
z (m)
Time (hr)
296.4
293.1
289.8
286.5
283.2
279.9

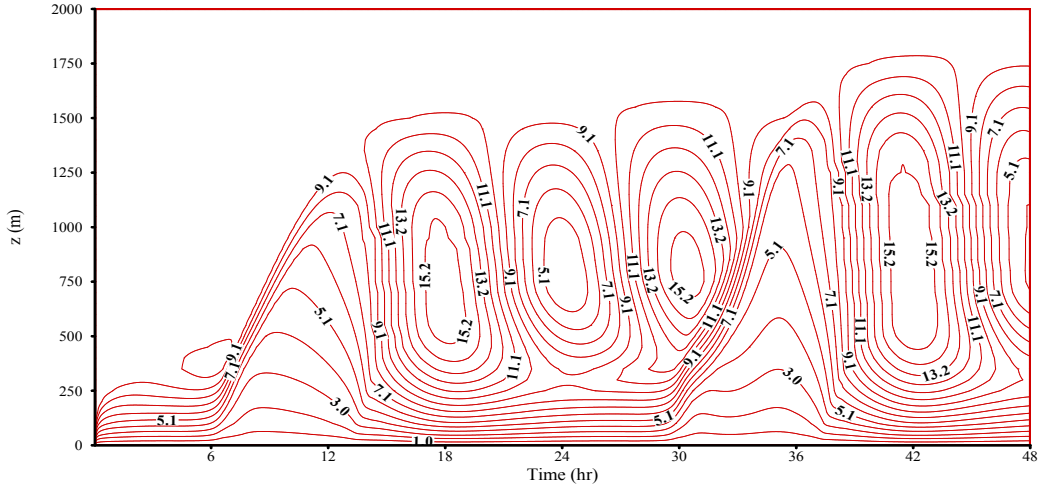
z (m)
Time (hr)

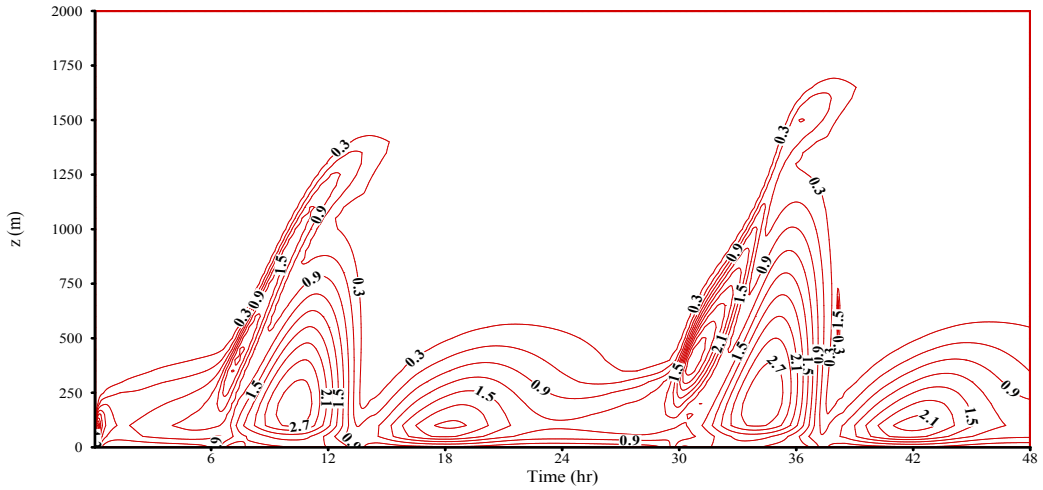
z (m)
Time (hr)

Fig. 5.7. Time-height contour plots of the *E-l* model, a) potential temperature (K), b) wind (m s^{-1}), and c) turbulent kinetic energy (m^2 s^{-2}) for 48-hour simulation of the second GABLS experiment day-night cycle using the proposed SDIRK scheme (PSDIRK (2)). The spatial resolution of $\Delta z = 50$ m with the time step of $\Delta t = 20$ s was chosen for the model.

Linear stability results are acceptable and the numerical solutions are in very good agreement with the reference solutions. The proposed schemes exhibit noteworthy compatability with the diagnostic and prognostic approaches including the *E-l* turbulence model, with temporal and spatial resolutions having the least influence on stability and accuracy, while preserving monotonicity.

Acknowledgement

The research was supported by Environment Canada and Natural Sciences and Engineering Research Council of Canada.

5.7 Appendix

To explain the schemes in an abstract format, we consider the following ODE initial value problem

$$\dot{y}(t) = f(t, y), \quad y(t_0) = y_0 \tag{5.42}$$

An *s*-stage partitioned Runge-Kutta method is characterized by the Butcher tableau and describes one step of the solution ($y_{old} \rightarrow y_{new}$), as follows.

The Butcher tableau

$$\begin{array}{c|ccc} c_1 & a_{11} & \dots & a_{1s} \\ \vdots & \vdots & & \vdots \\ c_s & a_{s1} & \dots & a_{ss} \\ \hline & b_1 & \dots & b_s \end{array} \tag{5.43}$$

includes the coefficients of s-stage Runge-Kutta methods where b_1, ..., b_s, a_{ij} (i, j = 1, ..., s) are real numbers and $c_i = \sum_j a_{ij}$. The solution at the new time step n+1 for an s-stage Runge-Kutta method is obtained by

$$y_{n+1} = y_n + h \sum_{i=1}^{s} b_i k_i \,, \tag{5.44}$$

where

$$k_i = f(t_n + c_i h, y_n + h \sum_{j=1}^{s} a_{ij} k_j) \tag{5.45}$$

with step size h. The Butcher tableaus of the schemes mentioned in the paper appear in the following.

SDIRK (1,2)

1/2	1/2
	1

SDIRK (2,2)

1/4	1/4	0
3/4	1/2	1/4
	1/2	1/2

SDIRK (3,2)

$1/6$	$1/6$	0	0
$1/2$	$1/3$	$1/6$	0
$5/6$	$1/3$	$1/3$	$1/6$
	$1/3$	$1/3$	$1/3$

SDIRK (2,3)

$\frac{3-\sqrt{3}}{6}$	$\frac{3-\sqrt{3}}{6}$	0	
$\frac{3+\sqrt{3}}{6}$	$\frac{1}{\sqrt{3}}$	$\frac{3-\sqrt{3}}{6}$	
	$1/2$	$1/2$	

SDIRK (3,3)

$\frac{1-\sqrt{1/2}}{2}$	$\frac{1-\sqrt{1/2}}{2}$	0	0
½	$\frac{1}{\sqrt{8}}$	$\frac{1-\sqrt{1/2}}{2}$	0
$\frac{1+\sqrt{1/2}}{2}$	$\frac{1}{\sqrt{8}}$	$\frac{1}{\sqrt{8}}$	$\frac{1-\sqrt{1/2}}{2}$
	$1/3$	$1/3$	$1/3$

PSDIRK (1)

1	1	0
2	1	1
	$3/4$	$1/4$

PSDIRK (2)

$1/2$	$1/2$	0
$3/2$	1	$1/2$
	$3/4$	$1/4$

5.7.1 A.1. Stability properties

Considering the standard linear test equation $\dot{y} = \lambda y$, the stability regions (see Atkinson et al. (2009) or Butcher (2008) for complete details) of the optimal SDIRK schemes are shown in Fig. 5.8, where the dark area shows the region of stability. Obviously, the optimal SDIRK schemes are A-stable up to order 2, including the left-half plane. 3rd-order SDIRKs' instability regions enter the left-half plane so they are not A-stable. For nonlinear problems, A-stability does not necessarily mean that a scheme performs well. Another form of stability which is very useful for nonlinear problems is B-stability. If we require that the numerical solution be contractive (that is, different solutions cannot become further apart or separated), it needs to be B-stable (Atkinson et al. (2009)). For a scheme to be B-stable, two conditions must be satisfied (Burrage and Butcher (1979); Butcher (2008)):

$$B = diag(b_1, \dots, b_s) \qquad M = BA + A^T B - bb^T \tag{5.46}$$

are nonnegative semidefinite (i.e. $x^T Mx \geq 0$ and $x^T Bx \geq 0$ for all vectors x), where $A = [a_{ij}]$ and $b = [b_i]$.

Testing these conditions on the SDIRK schemes shows that the schemes SDIRK (1,2), SDIRK (2,2), and SDIRK (3,2) are B-stable since Matrix $M = 0$ for all of them and $b > 0$. Instead, SDIRK (2,3) and SDIRK (3,3), in spite of having $b > 0$, have $M = \begin{bmatrix} -0.0387 & 0.0387 \\ 0.0387 & -0.0387 \end{bmatrix}$ with eigenvalues of -0.0774, 0.0000 and $M =$

$\begin{bmatrix} -0.0135 & 0.0067 & 0.0067 \\ 0.0067 & -0.0135 & 0.0067 \\ 0.0067 & 0.0067 & -0.0135 \end{bmatrix}$ with eigenvalues of -0.0202, -0.0202, 0.0000, respectively. Hence, the conditions in Eq. (5.46) are not satisfied and these two schemes are not B-stable. To get B-stability, it is important to solve the stage equations sufficiently accurately.

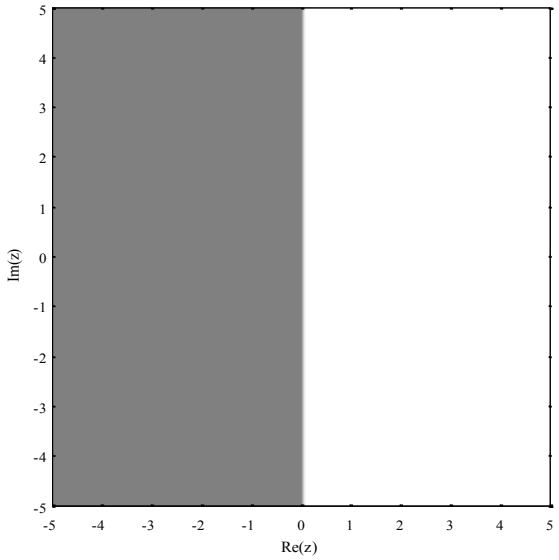

SDIRK (1,2)

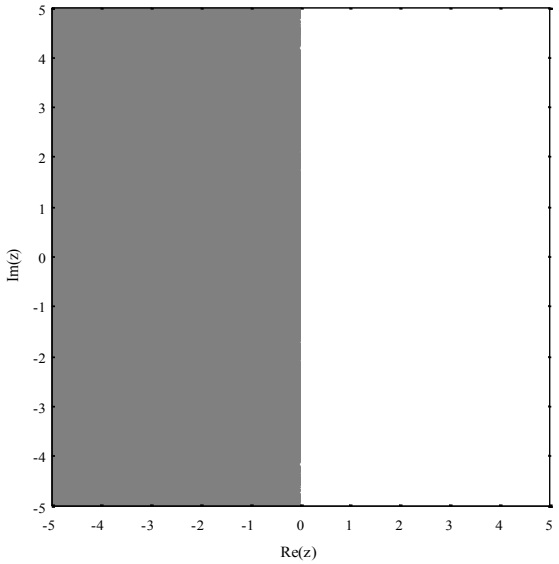

SDIRK (2,2)

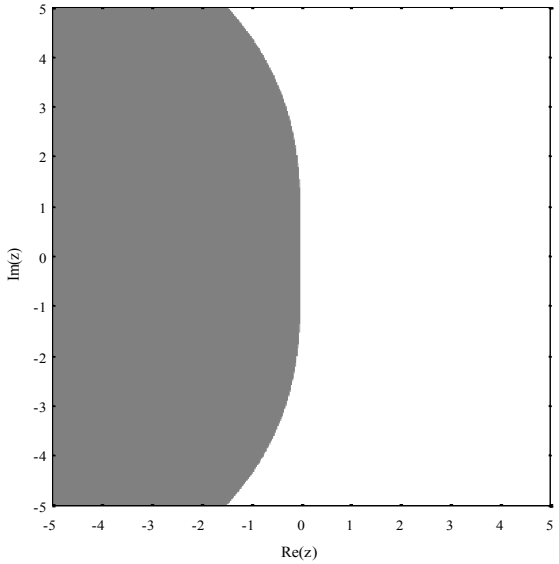

SDIRK (2,3)

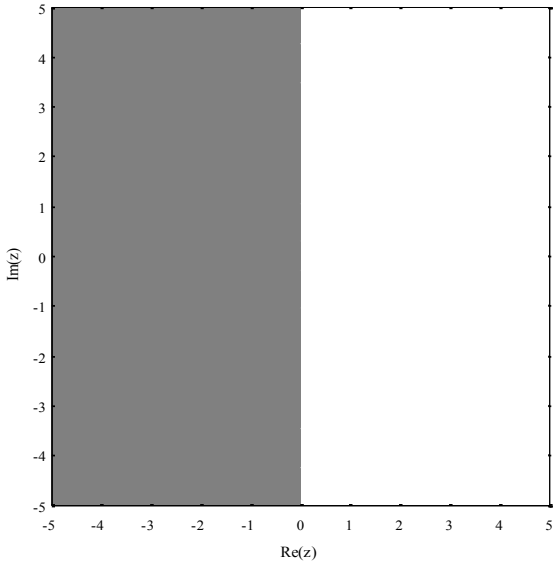

SDIRK (3,2)

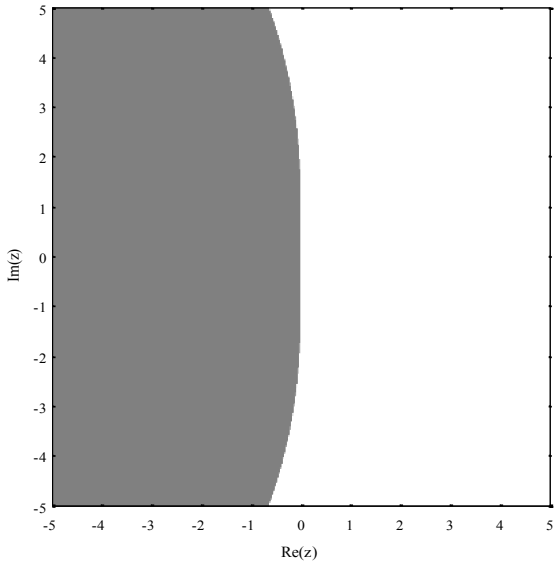

SDIRK (3,3)

Fig. 5.8. Stability regions for SDIRK schemes with different stages and orders of accuracy. The first number in the parentheses shows the stages, and the second number shows the order of accuracy.

6. Optimal High-Order Diagonally-Implicit Runge-Kutta Schemes for Nonlinear Diffusive Systems on Atmospheric Boundary Layer[3]

Abstract

Nonlinear diffusion equations are extensively applicable in diverse fields of science and engineering. Numerical stability is a common concern in this class of equations. In the present study, a three-stage third-order diagonally-implicit Runge-Kutta (DIRK) scheme is introduced by optimizing the error and linear stability analysis for a commonly used nonlinear diffusive system in atmospheric boundary layer. The proposed scheme is stable for a wide range of time steps and able to resolve different diffusive systems with diagnostic turbulence closures, or prognostic ones with a diagnostic length scale, with enhanced accuracy and stability compared to current schemes. It maintains A-stability, which makes it appropriate for the solution of stiff problems. The procedure implemented in this study is quite general and can be used in other diffusive systems as well.

Keywords: Nonlinear diffusion; Atmospheric boundary layer; Numerical stability; Optimal schemes; Diagonally-implicit Runge–Kutta; High-order accuracy; Multi-stage integration; Stiff equations.

6.1 Introduction

In many atmospheric models, nonlinear diffusive systems contain various physical parameterizations to represent sub-grid scale physical phenomena such as

[3] This chapter has been published as Farshid Nazari, Abdolmajid Mohammadian, Martin Charron, and Ayrton Zadra, “Optimal High-order Diagonally-Implicit Runge-Kutta Schemes for Nonlinear Diffusive Systems on Atmospheric Boundary Layer, Journal of **Computational Physics**: "Frontiers in Computational Physics: Modeling the Earth" 271 (2014) 118–130 http://dx.doi.org/10.1016/j.jcp.2014.01.039.

radiation, turbulence, clouds, moist convection and vertical turbulent mixing (Janiskova et al., 1999; Siebesma et al., 2007; Staniforth and Wood, 2008; Teixeira et al., 2007). Nonlinearities introduced by these parameterizations can cause several specific numerical problems; in particular, for parameter values (e.g. eddy-diffusivity coefficient and mass-flux coefficient) and time steps typically used in operational Numerical Weather Prediction (NWP) systems, spurious numerical oscillations may occur in some variables due to the ensuing stiffness. To prevent these problems, the time step in the solution of nonlinear diffusive systems cannot be increased significantly, which leads to prohibitive computational costs. Furthermore, oscillatory results have also been reported in the literature for this kind of systems (Teixeira et al., 2007; Girard and Delage, 1990). Explicit schemes are not desirable due to small time steps required to maintain numerical stability, which may lead to prohibitive computational costs. The problem of computational costs occurs with the use of fully implicit methods as well. *Diagonally-implicit Runge-Kutta* (DIRK) methods have been considered as an appropriate choice for the solution of stiff equations (see e.g. Franco et al., 1997). These schemes possess the advantages of implicitness while they are computationally efficient in comparison with fully coupled multi-stage implicit methods in that each stage in DIRK methods can be solved independently. An exhaustive study of strong stability preserving *singly-diagonally-implicit Runge-Kutta* (SDIRK) schemes regarding their performance in *atmospheric boundary layer* (ABL) simulation can be found in (Nazari et al., 2014). On the other hand, a class of *extended backward differentiation formulae* (EBDF) was introduced by Cash (1980) for the integration of stiff ordinary differential equations, which was later modified by Cash (1983) to enhance the stability properties and reduce the computational efforts.

Optimal temporal integration schemes have drawn attention in the simulation of some physical phenomena such as wave propagation (e.g. Hu et al., 1996; Nazari et al., 2014). In these studies, various single-step multi-stage explicit Runge-Kutta schemes are introduced by optimizing an error function regarding the nature of the phenomenon, which maintain low dissipation and dispersion.

Nazari et al. (2013) proposed a *modified extended backward differentiation formulae* (ME BDF) DIRK scheme which has greatly mitigated the drawbacks mentioned in the simulation of atmospheric boundary layer. It prevents oscillatory results for highly nonlinear damping and diffusive systems for large time steps; however, it is formally first-order and induces some numerical inaccuracy for high spatial resolutions.

In the present study, an optimal three-stage third-order diagonally-implicit Runge-Kutta ME BDF scheme is investigated and introduced for the solution of a typical nonlinear diffusive system in ABL, which is described in Section 6.2. The focus is to obtain a higher-order method which possesses the strengths of the previously proposed ME BDF scheme (Nazari et al., 2013) and can preferably gain an improvement in performance for high spatial resolutions and large time steps in comparison with available schemes, while retaining a comparable accuracy for low spatial resolutions as well. The final goal is to find and apply a new scheme on more realistic studies of the diffusive systems in the planetary boundary layer with the fully three dimensional models such as Canadian Global Environmental Multi-scale (GEM) and Meso-scale Compressible Community (MC2) models.

In Section 6.2, the nonlinear diffusive system is introduced. Multi-stage Runge-Kutta schemes and the corresponding order conditions are described in Section 6.3. Numerical stability analysis and the resulting new scheme are presented in Section 6.4. In Section 6.5, an algorithm is provided for the numerical solution of the problems under study using a multi-stage Runge-Kutta scheme. Section 6.6 contains the corresponding numerical tests. Conclusions are drawn in Section 6.7.

6.2 Nonlinear Diffusive System

Nonlinear diffusion equations appear in many applications, including Navier-Stokes, shallow water systems (Oran & Boris, 1987), magnetohydrodynamics (Potter, 1973), and atmospheric boundary layer equations. As an example of a highly nonlinear

diffusive system, we consider a commonly used model for atmospheric boundary layers. In this model, two diffusion equations are solved for wind velocity u and potential temperature θ

$$\frac{\partial u}{\partial t} = \frac{\partial}{\partial z}\left(K\frac{\partial u}{\partial z}\right) \tag{6.1}$$

$$\frac{\partial \theta}{\partial t} = \frac{\partial}{\partial z}\left(K\frac{\partial \theta}{\partial z}\right) \tag{6.2}$$

This is a one-dimensional system with z being the vertical component. Although the diffusion coefficients are generally different for wind and potential temperature, they are assumed to be equal in this study and are obtained from the following equation [Girard and Delage, 1990]

$$K = l^2\left|\frac{\partial u}{\partial z}\right|(1 + b|Ri|)^n, \qquad \left(\frac{\partial u}{\partial z} \neq 0\right) \tag{6.3}$$

where l is the mixing length, n and b are constants, and Ri is the Richardson number

$$Ri = \frac{g}{\theta_0}\frac{\partial\theta/\partial z}{(\partial u/\partial z)^2} \tag{6.4}$$

where g is the gravity acceleration and θ_0 is a constant. The mixing length is also variable with the elevation but is kept constant for the following numerical stability analysis.

As the static stability increases, K should gradually vanish, while it grows as the static instability intensifies. Note that static stability corresponds to $Ri > 0$ and static instability is vice versa. To obtain this behaviour, n and b must vary according to stability, and only one of them must change sign when the stability sign changes. As the

results of this study will be compared with Girard and Delage (1990) study, the same values of *n* and *b* are considered, which are

$$\begin{aligned} n &= -2; b = 5 \quad for\ Ri > 0 \\ n &= \frac{1}{2}; b = 20 \quad for\ Ri < 0 \end{aligned} \tag{6.5}$$

6.3 Third-Order Multi-Stage Runge-Kutta Schemes

The following ODE initial value problem is considered to introduce a multi-stage Runge-Kutta scheme in a simplified abstract setting,

$$\dot{y}(t) = f(t, y), \quad y(t_0) = y_0 \tag{6.6}$$

An *s*-stage partitioned Runge-Kutta method is characterized by the Butcher tableau and describes one step of the solution ($y_{old} \rightarrow y_{new}$), as follows. The Butcher tableau

c	**A**
	$\mathbf{b^T}$

(6.7)

includes the coefficients of *s*-stage Runge-Kutta methods where $\mathbf{b^T} = [b_1, ..., b_s]$, $\mathbf{A}=[a_{ij}]$ ($i,j= 1, ..., s$) are real numbers and $c_i = \sum_j a_{ij}$ in **c** for a physically justified scheme. The solution at the new time step n+1 for an *s*-stage Runge-Kutta method is then obtained by

$$y^{n+1} = y^n + h \sum_{i=1}^{s} b_i k_i \tag{6.8}$$

where

$$k_i = f(t^n + c_i h, y^n + h \sum_{j=1}^{s} a_{ij} k_j) \tag{6.9}$$

with step size h.

To retain third order accuracy, the coefficients need to satisfy the following "order conditions"

$$\sum_{i=1}^{s} b_i = 1 \tag{6.10}$$

for first order accuracy,

$$\sum_{i=1}^{s} b_i c_i = \frac{1}{2} \tag{6.11}$$

for second order accuracy, and

$$\begin{gathered} \sum_{i=1}^{s} b_i {c_i}^2 = \frac{1}{3} \\ \sum_{i=1}^{s} \sum_{j=1}^{s} b_i a_{ij} c_j = \frac{1}{6} \end{gathered} \tag{6.12}$$

for third order accuracy.

6.4 Numerical Stability Analysis

The analytical stability of the system of equations has been established by (Girard and Delage, 1990). They also studied the stability of a class of two-time-level schemes. In this section, we investigate third order 3-stage DIRK schemes to find a scheme which has the optimal numerical dissipation. More explanations will be provided during this section. To reach this goal, a parametric 3-stage DIRK scheme will be applied for the temporal discretization of the Eq. (6.1) stage by stage and the numerical amplitude will be obtained. Then, the numerical dissipation will be optimized for the best behaviour of the scheme we can obtain.

To obtain a DIRK scheme, the matrix needs to be lower-triangular. The advantage of DIRK schemes is that the solution at each stage is uncoupled from the solutions at future stages, which leads to facilitated implementation of the scheme and computational efficiency.

Considering explicit diffusion coefficient and implicit velocity, the diffusion Eq. (6.1) can be written as

$$u_t = (Ku_z^+)_z = K_z u_z^+ + Ku_{zz}^+ \tag{6.13}$$

The plus sign designates the next time step. Girard and Delage (1990) showed that K_z is given by

$$K_z = \frac{K(1-2\alpha)}{u_z} u_{zz} + \frac{K\alpha}{\theta_z}\theta_{zz} \tag{6.14}$$

where

$$\alpha = \frac{nb|Ri|}{1+b|Ri|} \tag{6.15}$$

Consideration of solutions of the form $u = ce^{\omega t+imz}$ leads to $u^+ = \lambda u$, where λ is an amplification factor and c is a constant. Now, if we replace all terms in RHS of the Eq. (6.13) using a second-order centered scheme for first- and second-order derivatives, we obtain

$$k_1 = U_t^1 = \left(\frac{K(1-2\alpha)}{\frac{u_{j+1}^n - u_{j-1}^n}{2\Delta z}} \frac{u_{j+1}^n - 2u_j^n + u_{j-1}^n}{\Delta z^2} + \frac{K\alpha}{\frac{\theta_{j+1}^n - \theta_{j-1}^n}{2\Delta z}} \frac{\theta_{j+1}^n - 2\theta_j^n + \theta_{j-1}^n}{\Delta z^2} \right) \frac{U_{j+1}^1 - U_{j-1}^1}{2\Delta z} + K \frac{U_{j+1}^1 - 2U_j^1 + U_{j-1}^1}{\Delta z^2} \tag{6.16}$$

for the first stage, in which U^1 and k_1 are the velocity and the RK coefficient at the first stage ($k_i = f(t^n + c_i h, y^n + h\sum_{j=1}^{s} a_{ij}k_j)$), respectively. This discretized equation leads to a tridiagonal system, which is computationally efficient to solve. Replacing the discretized terms by their equivalent form ($u_{j+1}^n = u^n e^{im(\Delta z)}$ and $U^1 = \lambda_1 u^n$), we obtain

$$k_1 = \left(\frac{2K(1-2\alpha)}{u^n(2isin(m\Delta z))} \frac{u^n(-4sin^2\left(\frac{m\Delta z}{2}\right))}{\Delta z} + \frac{2K\alpha}{\theta^n(2isin(m\Delta z))} \frac{\theta^n(-4sin^2\left(\frac{m\Delta z}{2}\right))}{\Delta z} \right) \frac{\lambda_1(2isin(m\Delta z))}{2\Delta z} u^n + K \frac{-4\lambda_1 sin^2\left(\frac{m\Delta z}{2}\right)}{\Delta z^2} u^n \tag{6.17}$$

Finally,

$$k_1 = \frac{-4Ksin^2\left(\frac{m\Delta z}{2}\right)}{\Delta z^2}(2-\alpha)\lambda_1 u^n \tag{6.18}$$

Since $U^1 = u^n + a_{11}k_1\Delta t$, one obtains

$$\lambda_1 = \frac{1}{1 + \frac{4Ksin^2\left(\frac{m\Delta z}{2}\right)(2-\alpha)(a_{11}\Delta t)}{\Delta z^2}} \tag{6.19}$$

Then, k_1 is simply

$$k_1 = \frac{\lambda_1 - 1}{a_{11}\Delta t}u^n \tag{6.20}$$

Similar procedure is employed for all three stages. The stages differ in the start point which is obtained from the last stage and the last stage value is used to calculate the diffusion coefficient. Thus, for the second stage differing in the start point, replacing $U^2 = \lambda_2(u^n + a_{21}k_1\Delta t)$ according to the Butcher tableau gives

$$k_2 = \frac{-4Ksin^2\left(\frac{m\Delta z}{2}\right)}{\Delta z^2}(2-\alpha)\lambda_2(u^n + a_{21}k_1\Delta t) \tag{6.21}$$

On the other hand

$$\frac{(\lambda_2 - 1)}{\Delta t}(u^n + a_{21}k_1\Delta t) = a_{22}k_2 \tag{6.22}$$

Hence,

$$\lambda_2 = \frac{1}{1 + \frac{4Ksin^2\left(\frac{m\Delta z}{2}\right)(2-\alpha)(a_{22}\Delta t)}{\Delta z^2}} \tag{6.23}$$

and k_2 is

$$k_2 = \frac{\lambda_2 - 1}{a_{22}}(1 + \frac{a_{21}}{a_{11}}(\lambda_1 - 1))\frac{u^n}{\Delta t} \tag{6.24}$$

Similarly, for the third stage by considering the start point as $u^n + (a_{31}k_1 + a_{32}k_2)\Delta t$ one obtains

$$k_3 = \frac{-4Ksin^2\left(\frac{m\Delta z}{2}\right)}{\Delta z^2}(2-\alpha)\lambda_3[u^n + (a_{31}k_1 + a_{32}k_2)\Delta t] \tag{6.25}$$

$$\lambda_3 = \frac{1}{1 + \frac{4Ksin^2\left(\frac{m\Delta z}{2}\right)(2-\alpha)(a_{33}\Delta t)}{\Delta z^2}} \tag{6.26}$$

Thus,

$$k_3 = \frac{\lambda_3 - 1}{a_{33}}\left[1 + \frac{a_{31}}{a_{11}}(\lambda_1 - 1) + \frac{a_{32}}{a_{11}}(\lambda_2 - 1)\left(1 + \frac{a_{21}}{a_{11}}(\lambda_1 - 1)\right)\right]\frac{u^n}{\Delta t} \tag{6.27}$$

According to the Butcher tableau of a Runge-Kutta scheme, the function value at the new time step is

$$u^{n+1} = u^n + (b_1k_1 + b_2k_2 + b_3k_3)\Delta t \tag{6.28}$$

Now, the final amplification factor of the 3-stage DIRK scheme, $\lambda = \frac{u^{n+1}}{u^n}$, can be obtained by replacing RK coefficients equivalents from Eq. (6.20), (6.24), and (6.27)

$$\lambda = 1 + \frac{b_1}{a_{11}}(\lambda_1 - 1) + \frac{b_2}{a_{22}}(\lambda_2 - 1)\left[1 + \frac{a_{21}}{a_{11}}(\lambda_1 - 1)\right] + \frac{b_3}{a_{33}}(\lambda_3 - 1)\left[1 + \frac{a_{31}}{a_{11}}(\lambda_1 - 1) + \frac{a_{32}}{a_{22}}(\lambda_2 - 1)\left(1 + \frac{a_{21}}{a_{11}}(\lambda_1 - 1)\right)\right] \tag{6.29}$$

The same calculations can be done for the potential temperature equation.

As mentioned in the introduction, we are looking for an optimal three-stage third-order DIRK ME BDF scheme which possesses the strengths of the previously proposed ME BDF scheme (Nazari et al., 2013). To reach this goal, we consider the ratio *r* of the reduction of the numerical amplitude (6.29) over the reduction of analytical amplitude after one time step

$$r = \frac{1 - \lambda}{1 - A(0, \Delta t)} \tag{6.30}$$

as the optimization parameter. The analytical amplitude A is the amplitude of a wave of length $\gamma = \frac{2\pi}{m}$, diffused by coefficient K as a function of time for various spatial resolutions (Girard and Delage, 1990)

$$A(m\Delta z, t) = exp\left[-m^2 K t(2 - \alpha)\frac{sin^2\left(\frac{m\Delta z}{2}\right)}{\left(\frac{m\Delta z}{2}\right)^2}\right] \tag{6.31}$$

This amplitude A is free of temporal truncation error. Thus, $A(0, \Delta t)$ where $m\Delta z \to 0$ is obtained as

$$A(0, \Delta t) = exp[-m^2 K \Delta t(2 - \alpha)] \tag{6.32}$$

The optimal scheme, thus, is a scheme which has the closest r ratios to the mentioned ME BDF scheme (Nazari et al., 2013) for large time steps, specifically. As a result, the objective function for optimization is defined as

$$Err(T) = \int_2^{\infty} \int_T^0 \left| r_{opt} - r_{MEBDF} \right|^2 d\tau d\delta \tag{6.33}$$

where T is determined according to the range of Δt for which the scheme is optimized for, $\tau = \log\left(\frac{K\Delta t}{\gamma^2}\right)$, $\delta = \frac{\gamma}{\Delta z}$, and r_{opt} and r_{MEBDF} are the r ratios of the optimal scheme and the mentioned ME BDF scheme (Nazari et al., 2013), respectively. Minimized error function ($\left|\lambda_{opt} - A(0, \Delta t)\right|^2$) and different values for the error have also been tried as the optimization function to confirm the best behaviour of the optimization function (6.33). As was expected, $r_{\text{ME BDF}}$ is a desirable ratio for the optimization. To ensure the stability of the optimal scheme, the amplification factor should not exceed unity for any value of Δt and Δz; i.e. $|\lambda| \leq 1$. So the A-stability of the optimal scheme is pre-approved.

The four conditions (6.10)-(6.12) for a third-order scheme form a constrained optimization problem and leave five out of the nine unknown coefficients of a third-order three-stage DIRK scheme for optimization. In the present study, the coefficients a_{11}, a_{21}, a_{22}, a_{31}, and a_{33} are chosen as the optimization parameters. A value of $T = -1$ is chosen for the present optimal scheme to cover large time steps. The parameters are searched as the constraints are satisfied and the objective function (6.33) is minimized. The optimal scheme parameters obtained from the optimization process are tabulated in Table 6.1. Note that a range of parameters can be obtained from the optimization process, but according to some constraints i.e. the absolute value of the numerical amplitude to be less than one (A-stable scheme) or the satisfying performance of a scheme for the problem under study, the optimal scheme is selected. The large number of significant digits of the coefficients is required for the third order nominal accuracy. It can be seen that the c_i values become large, but for the type of problems studied in

the paper (nonlinear diffusions), the proposed scheme works very well according to the numerical tests results in Section 6.6. It can be the result of systematic error cancellation due to satisfying the error conditions, Eqs. (6.10)-(6.12). We have considered this issue before and tried to restrict the coefficients, but we found out that this is not a crucial criterion and let it be free to find the best performance of the scheme.

The stability region of the optimal scheme for the linear ODE typically used for A-stability analysis is also plotted in Fig. 6.1 (right), which, as expected, confirms A-stability of the scheme. The stability region in the right plot of Fig. 6.1 extends to the entire negative half plain (i.e. it is for all z with $Re(z) \leq 0$). The current scheme does not depend on α, however we took α=0.5 for the optimization. Since the numerical dissipation graph does not change with a slight variations in α, the objective function does not change for the optimization and the same coefficients are obtained for the optimized scheme. As a result, the optimal scheme remains A-stable for a range of α around 0.5.

The r ratio of the optimal scheme along with Nazari et al. (2013) proposed ME BDF scheme are shown in Fig. 6.1. As intended, the optimal scheme shows a similar behaviour to the mentioned ME BDF scheme. These schemes show larger numerical amplitudes than the analytical one as the time step increases, which corresponds to $K\Delta t/\gamma^2 \geq 10^{-1.5}$. In large time steps, therefore, while the analytical wave amplitude exhibits no diffusion, the schemes shown in Fig. 6.1 induce numerical diffusion, which helps in damping the oscillations (Nazari et al., 2013). As will be shown in the numerical results, the schemes with the mentioned damping behaviour for short waves perform very well for large time steps, although their r ratio converges to 0.7 in that region. Fig. 6.1 infers more accuracy for the optimal scheme for smaller time steps, while afterwards for very large time steps, the mentioned optimal scheme and the proposed ME BDF scheme by Nazari et al. (2013) merge.

Table 6.1. Optimal coefficients for the third-order three-stage Diagonally-Implicit Runge-Kutta scheme.

Parameter	Value
a_{11}	1.5599102573609003
a_{21}	1.6564644024196673
a_{22}	13.127035081299413
a_{31}	1.6581695293693006
a_{32}	1.6726602892716570
a_{33}	11.047309968089305
b_1	1.1699600218442656
b_2	2.7597127236998267
b_3	−2.9296727455441003

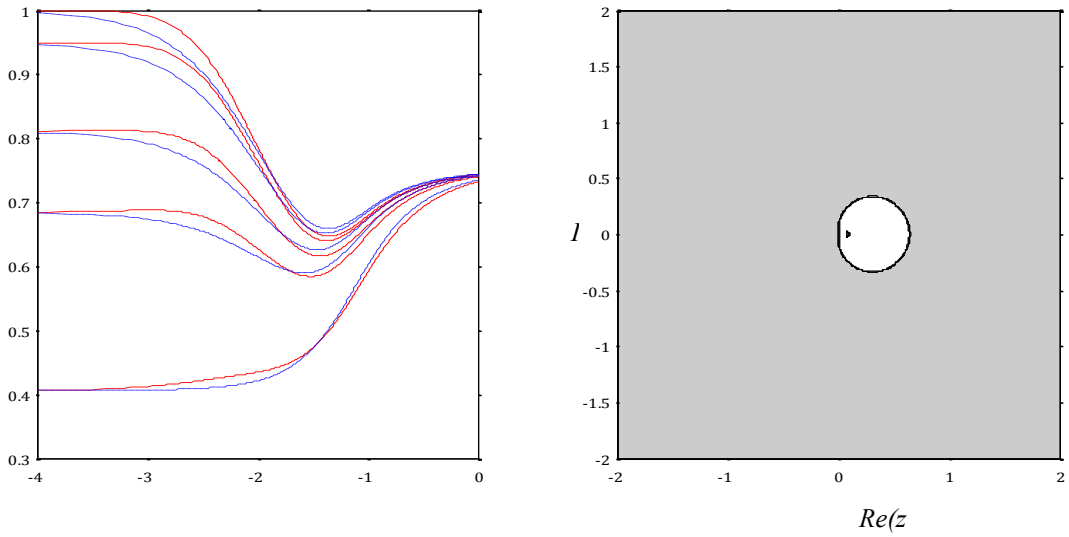

Fig. 6.1. The ratio of reduction of numerical amplitude to that of the analytical one (r) for various spatial resolutions (δ =2, 3, 4, 8, ∞) for the proposed optimal scheme (solid line) compared to Nazari et al. (2013) ME BDF scheme (dashed line) in the left; and the stability region (dark area) in the right.

For both of the schemes shown in Fig. 6.1, the waves of length $2\Delta z$ (lowest spatial resolution) lead to the largest error in the region of small Δt values, and the waves with different lengths do not cross each other while Δt increases. Lastly, the optimal scheme is from the third-order family of DIRK schemes, while the other scheme in Fig. 6.1 is only first-order.

6.5 Numerical Solution Procedure

A general multi-stage Runge-Kutta as the temporal scheme is applied to the following discretized form of Eq. (6.1) to elaborate how the proposed optimal DIRK scheme is used to numerically solve the diffusion Eq. (6.1). Let

$$\begin{aligned} u^n, U^i \in R^m, \mathbf{U} &= \begin{pmatrix} U^1 \\ U^2 \\ \vdots \\ U^s \end{pmatrix} \in R^{sm}, f: R^m \to R^m, \mathbf{F}(\mathbf{U}) \\ &= \begin{pmatrix} f(U^1) \\ f(U^2) \\ \vdots \\ f(U^s) \end{pmatrix}, \end{aligned} \tag{6.34}$$

where

$$\begin{aligned} f(U^i) &= \left(\frac{\frac{K_{j+1}^i + K_j^i}{2}\left(\frac{U_{j+1}^i - U_j^i}{\Delta z}\right) - \frac{K_j^i + K_{j-1}^i}{2}\left(\frac{U_j^i - U_{j-1}^i}{\Delta z}\right)}{\Delta z} \right) \\ &\approx \frac{\partial}{\partial z}\left(K(U^i)\frac{\partial U^i}{\partial z} \right). \end{aligned} \tag{6.35}$$

Then, applying the *s*-stage DIRK scheme (6.7)-(6.9) on problem (6.1) we obtain:

$$\frac{\mathbf{U} - \mathbf{1} \otimes u^n}{\Delta t} = (\mathbf{A} \otimes \mathbf{I})\mathbf{F}(\mathbf{U}) \tag{6.36}$$

where $\mathbf{1}$ is the $s \times 1$ vector having all its components equal to one, and $\mathbf{I}$ the $m \times m$ identity matrix. It is worth mentioning that there are different choices for the diffusion

coefficient K when marching from t^n to $t^n + \Delta t$: (i) compute K only once using field values at t^n and use the same K for all the s stages in the time-step n+1; (ii) compute K once for each DIRK stage using the latest available values (previous DIRK stage or t^n values at first stage); and iii) a combination of (i) and (ii) (see e.g. Nazari et al. (2013) ME BDF scheme). Option (i) is very efficient computationally, as often calculating the diffusion coefficient in an atmospheric model is more expensive than solving the tri-diagonal system. Hence, it is recommended to first try this option for modeling; as it is the case for all the numerical tests in Sections 6.1 and 6.2, except for the very stiff test in Section 6.1.1 shown in Fig. 6.2 (right). In this test, and only in this test, K is computed via option (ii). Option (iii) can also be taken into consideration if the first two options fail to properly simulate the boundary layer properties.

Note that the R.H.S of the Eq. (6.1) is equivalent to $\mathbf{k}$ vector representing multi-stage Runge-Kutta coefficients of rate of change in Eq. (6.9), which infers $\mathbf{k} = \mathbf{F}(\mathbf{U})$. Thus, Eq. (6.36) can alternatively be written as

$$\frac{\mathbf{U} - \mathbf{1} \otimes u^n}{\Delta t} = (\mathbf{A} \otimes \mathbf{I})\mathbf{k} \tag{6.37}$$

Since $\mathbf{A}$ is a lower triangular matrix for a DIRK scheme, the above system is a tri-diagonal system in which each stage can be solved independently. However, it is obvious that the calculation of k_i (k in stage i) in Eq. (6.9) needs to know k's in previous stages, so it is better to solve for stage values from the first stage. This way, U^1 is obtained from Eq. (6.36) and as a result, k_1 is known from Eq. (6.37). By knowing k_1, in the same way, U^2 and then k_2 are computed using Eqs. (6.36) and (6.37); and this procedure continues to the last stage. When $\mathbf{U}$ is determined, $\mathbf{k}$ is also known and the solution at the new time-step n+1 can then be written as

$$u^{n+1} = u^n + \Delta t \mathbf{b^T k} \tag{6.38}$$

6.6 Numerical Results and Discussion

6.6.1 Stable boundary layer

6.6.1.1 Diagnostic turbulence closure scheme

An idealized case similar to Nazari et al. (2013) is considered in order to compare our results with their study. The problem specifications are:

- K is obtained from Eq. (6.3) and (6.5) with $l = 50$ m
- Boundary conditions are $u = 0$ ms^{-1} and $\theta = 0$℃ at $z = 0$, and zero gradient at $z = 1000$ m
- Initial conditions are $u = 10$ ms^{-1}, and θ varies linearly with z from 0 ℃ to 1 ℃

The vertical resolution should be chosen very carefully since the traditional schemes for vertical diffusion in NWP models may cause oscillatory, inaccurate results if the vertical resolution is higher than a specific limit and an unwanted delay may occur in the solution from the high K-value region to the low K-value region (boundary layer to free atmosphere) due to the maximum rate of one grid point per time step (Girard and Delage, 1990). Thus, the focus in this study is on the refinement in the vertical direction to find an alternative scheme performing optimally and effectively for high spatial resolution.

The calculated wind vertical distribution using the ME BDF scheme (Nazari et al., 2013) and the optimal third-order scheme are shown in Fig. 6.2 for the stable boundary layer for two vertical resolutions and with the same time step size as (Girard and Delage, 1990), $\Delta t = 1{,}800\ s$. The R.H.S of the diffusion Eq. (6.1) is treated implicitly for the variable itself (u) but explicitly for the diffusion coefficient (K). u or θ in Eq. (6.3) can be replaced either from the last time step or the last stage; or a combination of them like the one used in the Nazari et al. (2013) proposed ME BDF scheme. This combined with a DIRK scheme as the temporal scheme (L.H.S of Eq. (6.1)) results in a

tri-diagonal system which is very efficient to solve. More clarification of the numerical solution algorithm can be found in Section 6.5.

For $\Delta z = 100$ m, both the optimal scheme and the ME BDF scheme show a very good agreement with the reference solution calculated using Crank-Nicolson second-order scheme with a very fine grid of $\Delta z = 20$ m and $\Delta t = 18$ s (solid line). Looking carefully reveals that the optimal scheme result is a bit closer to the reference solution.

Five times higher spatial resolution than $\Delta z = 100$ m with $\Delta z = 20$ m, on the other hand, divulges that the optimal scheme results are highly compatible with the reference solution, while there is a discrepancy between the ME BDF scheme results and the reference solution for $\Delta z = 20$ m. It is worth mentioning that the diffusion coefficient in the third stage of the ME BDF scheme (see Nazari et al., 2013) is computed using an average of all previous stages including the previous time step field values; while in the proposed optimal scheme, we simply use the obtained variables from the previous stage to compute the diffusion coefficient in the current stage for the case of high spatial resolutions (Fig. 6.2 right). For low resolutions shown in Fig. 6.2 (left), the last time step variables are used only once to calculate the diffusion coefficient for all the three DIRK stages.

6.6.1.2 E-l turbulence closure scheme with Coriolis effect

As another test, one dimensional, horizontally homogeneous, dry boundary layer is simulated using the proposed optimal scheme and the ME BDF (Nazari et al., 2013) scheme as the temporal integration schemes in a model where the diffusive system of (6.1) and (6.2) changes as follows:

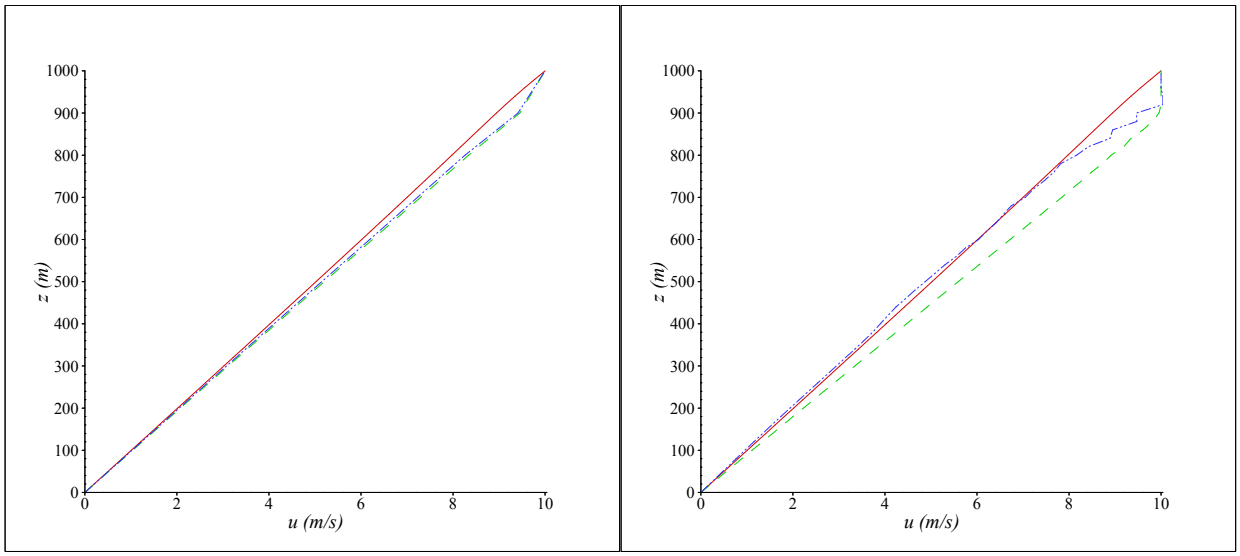

Fig. 6.2. Wind profiles after 4 hours for the stable boundary layer for two vertical resolutions of: $\Delta z = 100$ m (left) and $\Delta z = 20$ m (right) using the proposed optimal scheme (dash-dot-dot) and the ME BDF scheme (Nazari et al., 2013) (dash). The reference solution is shown by the solid line. For all lines, $\Delta t = 1{,}800$ s.

$$\frac{\partial u}{\partial t} = \frac{\partial}{\partial z}\left(K_m \frac{\partial u}{\partial z}\right) + f(v - v_g) \tag{6.39}$$

$$\frac{\partial v}{\partial t} = \frac{\partial}{\partial z}\left(K_m \frac{\partial v}{\partial z}\right) - f(u - u_g) \tag{6.40}$$

$$\frac{\partial \theta}{\partial t} = \frac{\partial}{\partial z}\left(K_h \frac{\partial \theta}{\partial z}\right) \tag{6.41}$$

to include Coriolis effect. The model is dominantly forced by the geostrophic wind and the surface potential temperature. No radiation or surface coupling scheme is considered for simplicity. K_m and K_h are the momentum and heat eddy diffusivities respectively, f is the Coriolis factor, and u_g and v_g are the geostrophic wind components.

The *E-l* turbulence closure scheme similar to that of Andre et al. (1978) is used, which is 1.5-order scheme with a diagnostic length scale. The turbulent fluxes are related to the flow vertical gradients via eddy diffusivities which are calculated using the turbulent kinetic energy. Thus, an extra prognostic equation is introduced to calculate the turbulent kinetic energy E with the square of the turbulent velocity scale $q^2=2E$:

$$\frac{\partial q^2}{\partial t} = \frac{\partial}{\partial z}\left(K_e \frac{\partial q^2}{\partial z}\right) + 2K_e M^2 - 2K_h N^2 - \frac{2q^3}{16.6l} \tag{6.42}$$

where $K_e = 0.2lq$ is the eddy diffusivity of the turbulent kinetic energy and l is the turbulent mixing length calculated by Blackadar (1962)

$$\frac{1}{l} = \frac{1}{\kappa z} + \frac{1}{\lambda} \tag{6.43}$$

where λ is a limiting mixing length that is generally set to a neutral value, e.g. 40 m. M and N are the Prandtl and Brunt-Vaisala frequencies

$$(M^2, N^2) = \left(\left(\frac{\partial u}{\partial z}\right)^2 + \left(\frac{\partial v}{\partial z}\right)^2, \frac{g}{\theta_0}\frac{\partial \theta}{\partial z}\right) \tag{6.44}$$

Then the turbulent kinetic energy is used to parameterise the eddy diffusivities in Eq. (6.39)-(6.41), which can be expressed as

$$K_m = lqS_m \tag{6.45}$$

$$K_h = lqS_h \tag{6.46}$$

where S_m and S_h are dimensionless stability functions, which have been parameterised by Galperin et al. (1988) as

$$S_m = \frac{0.393 - 3.085G_h}{1 - 40.803G_h + 212.469G_h^2} \tag{6.47}$$

$$S_h = \frac{0.494}{1 - 34.676G_h} \tag{6.48}$$

where G_h is a function of the Brunt-Vaisala frequency

$$G_h = -\frac{l^2N^2}{q^2} \tag{6.49}$$

Some constraints are implemented to eliminate numerical errors and also to ensure physically satisfying solutions. A minimum value of 1×10^{-5} m^2s^{-1}, which corresponds approximately to molecular values of diffusion, is imposed for the momentum, heat and turbulent kinetic energy diffusivities. A minimum value of 5×10^{-7} m^2s^{-2} is also imposed upon the turbulent kinetic energy.

Based upon the Kosovic and Curry (2000) stable nocturnal boundary-layer simulations, the first GABLS experiment is used in this study to verify the model with the proposed schemes. In this case the boundary layer is moderately stratified (θ gradient is not large), and the initial state and forcing are based upon observations from the BASE study in 1994. It is similar to a classic nocturnal boundary layer, though. The simulation, driven by an imposed barotropic geostrophic wind with a surface cooling rate, reaches a quasi-steady state, where all variables are steady except for the potential temperature changing at a constant rate.

The model initial and boundary conditions are as follows:

- The initial potential temperature profile is an adiabatic layer with potential temperature 265 K from the surface up to 100 m, above which the air is stable with a constant lapse rate of 0.01 K/m.
- The wind profiles are set equal to the geostrophic wind magnitudes (8 ms^{-1} in x-direction) initially throughout the boundary layer.
- The initial turbulent kinetic energy profile is decreasing linearly from 0.4 m^2s^{-2} at the surface to zero at the height of 250 m, at and above which is set to the imposed minimum value.
- A prescribed cooling rate of 0.25 K hr^{-1} is imposed at the surface, while at the top, the potential temperature is fixed at 268 K equal to the potential temperature of the free atmosphere.
- No-slip boundary condition is applied at the surface and at the upper boundary, the wind is forced to its geostrophic value.
- The turbulent kinetic energy is set to a Dirichlet boundary condition at the surface, which is $q_0^2 = B_1^{2/3} u_*^2$ (Mellor and Yamada, 1974), and its minimum value at the top.

The surface friction velocity is

$$u_* = -[(\overline{u'w'})_0^2 + (\overline{v'w'})_0^2]^{1/4} = -\sqrt{K_m \left|\frac{\partial u}{\partial z}\right|} \tag{6.50}$$

The model domain is 400 m deep and the simulation is run over a period of 9 hours.

A Coriolis parameter of $f = 1.39 \times 10^{-4}$ s^{-1} is used corresponding to 73°N, with a surface roughness height of $z_0 = 0.1$ m. As recommended by Beare et al. (2005) and Cuxart et al. (2005), the limiting value of the turbulent mixing length λ is set to 10 m, which is also consistent with mixing lengths estimated from observations of stable layers. λ value has a direct impact on proper representation of some features of the boundary layer such as the nocturnal jet or upper-level inversion. Eight-hour

simulation results are shown in Fig. 6.3 in comparison with a high resolution, three-dimensional Large Eddy Simulation from (Beare et al., 2005), which has been proved to be in good agreement with observed values.

The model results with $\Delta z = 20$ m from the proposed optimal scheme and Nazari et al. (2013) ME BDF scheme are close to those obtained by the LES model (Fig. 6.3.a). The potential temperature profile agrees well to the profile of the LES results throughout the mixed layer, whilst the upper level inversion at the boundary layer top is well defined. The nocturnal jet nearly coincides in level with that of the LES results, and is of the similar strength. Of particular note is that the model captures these features, which many other 1-D models, even those with similar closure schemes, fail to simulate (Cuxart et al., 2005). Furthermore, the spatial resolution is half and one fourth of the spatial resolution used by some other studies (e.g. Dunbar et al., 2008) with and without an adaptive grid, respectively, which approves the significant impact the temporal integration scheme has on the simulation results.

The model results are also shown with $\Delta z = 10$ m in Fig. 6.3.b, which show even more agreement between the proposed optimal scheme and the LES solution. The potential temperature profile matches the LES result more at lower and upper levels with some discrepancies at mid-levels, whilst the nocturnal jet occurs exactly at the same level and is of the same strength. More agreement is obtained at lower levels, too. It should be mentioned that the ME BDF scheme becomes unstable with the higher spatial resolution of $\Delta z = 10$ m with the same time step of

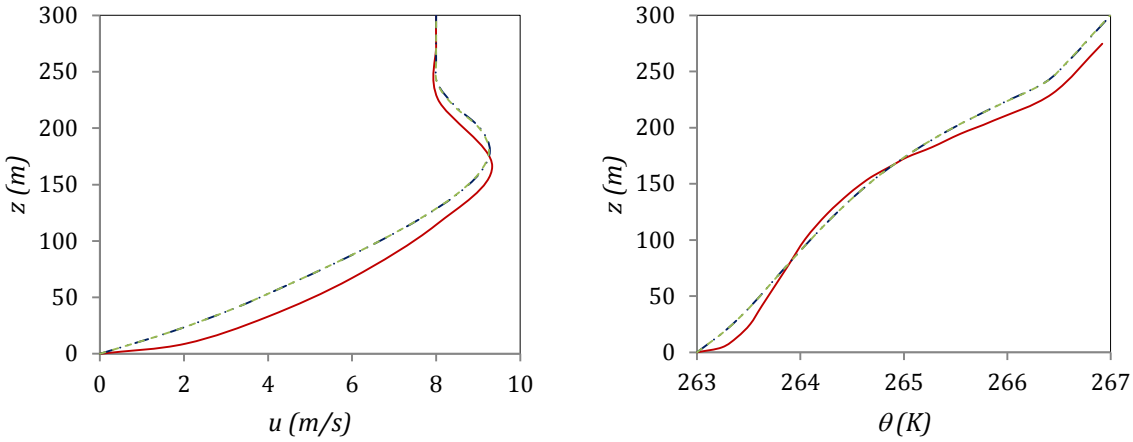
300
250
200
150
100
50
0
z (m)
0
2
4
6
8
10
u (m/s)
263
264
265
266
267
θ (K)

(a)

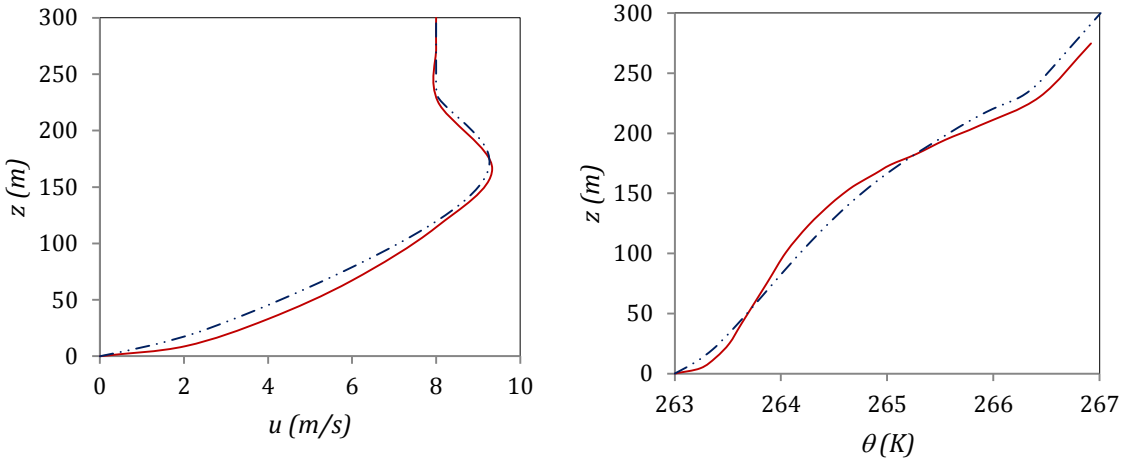
300
250
200
150
100
50
0
z (m)
0
2
4
6
8
10
u (m/s)
263
264
265
266
267
θ (K)

(b)

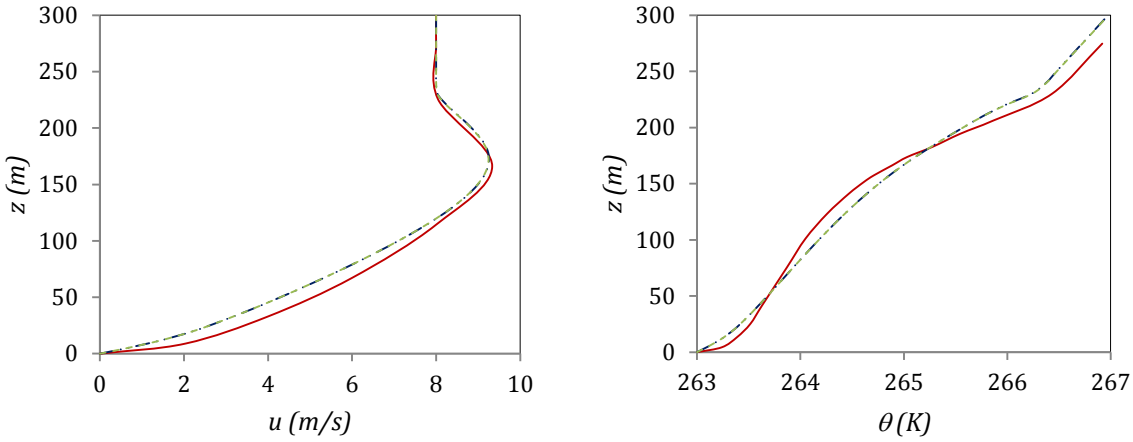
300
250
200
150
100
50
0
z (m)
0
2
4
6
8
10
u (m/s)
263
264
265
266
267
θ (K)

(c)

Fig. 6.3. Wind and potential temperature profiles after 8 hours of simulation for the stable boundary layer for the vertical resolutions and time steps of: a) $\Delta z = 20$ m, $\Delta t = 20$ s; b) $\Delta z = 10$ m, $\Delta t = 20$ s; and c) $\Delta z = 10$ m, $\Delta t = 10$ s; using the proposed optimal scheme (dash-dot-dot) and the ME BDF scheme (Nazari et al., 2013) (dash). The LES reference solution (Beare et al., 2005) is shown by the solid line.

$\Delta t = 20$ s. Hence, Fig. 6.3.c is added to clarify the performance of the two schemes for the higher spatial resolution of $\Delta z = 10$ m, but for the reduced time step of $\Delta t = 10$ s. As can be observed, the ME BDF scheme can also reproduce the numerical results similar to the optimal scheme at this time step. There is not a significant difference between the results obtained by the optimal scheme for $\Delta z = 10$ m, which approves the strength of the proposed optimal scheme in working with larger time steps and higher spatial resolutions.

6.6.2 Diurnal cycle

The proposed optimal three-stage third-order temporal scheme is used with the diagnostic closure model and the 1.5-order *E-l* turbulence closure model with a diagnostic length scale, discussed in this study in Sections 6.2 and 6.1.2, respectively, to simulate the GABLS second inter-comparison project as a further experiment. This is based on observations between 23 and 25 of October 1999 from the CASES99 field study in Kansas, USA, which were taken during a period with clear skies and when there was minimal change in the synoptic situation. The diurnal potential temperature cycle that was used to force the model at the surface can be found in Mellor and Yamada (1974). There exist some literature studying and modeling this case (e.g. Poulos et al., 2002; Steeneveld et al., 2006) using a very high resolution one-dimensional model which also include radiation and surface feedback processes. The simplified case dominantly forced by the surface potential temperature and the geostrophic wind is studied here.

Time-height contour plots of the prognostic variables in the model are shown in Fig. 6.4. According to this figure, the proposed optimal scheme with the mentioned diagnostic and *E-l* turbulence closure models successfully models the prognostic variables with regard to the good agreement qualitatively with other comparable modeling results such as Mellor and Yamada (1974) and Liu and Leung (1998). To clarify, the evolution of the potential temperature profile shows the rapid growth of the convective daytime layer, with entrainment occurring at the top of the boundary layer, and the slow growth of the nocturnal layer. The nocturnal jet is clearly observed in the wind profile, while during the day, the increasing turbulence through the boundary layer causes the reduction of the wind speed. The turbulent kinetic energy is clearly seen to peak during the day when convection is at its most vigorous, and extends throughout the layer, whilst it is subdued during the night. Enhanced turbulent kinetic energy can be seen at the top of the boundary layer where entrainment is occurring, and also in early morning when the convective layer is developing through the night-time mixed layer.

Particularly notable is that the diagnostic closure approach using the same temporal scheme leads to the satisfactory results with much larger time steps than the mentioned *E-l* turbulence closure model. However, *E-l* turbulence model can calculate the turbulent kinetic energy as shown in Fig. 6.4.e. Contrary to what we see in this study, oscillation problems have been reported in the literature e.g. Dunbar et al. (2008), in which the oscillations are transmitted above the boundary layer; where the adaptive grid solution does not work. The oscillations mostly occur in the transition region from diurnal to nocturnal layer due to the consequent rapid potential temperature gradient variation.

The results prove that the optimal scheme, in spite of being optimized for the diagnostic model, is compatible with different models, i.e. the mentioned *E-l* turbulence model. It is worth mentioning that for the mentioned *E-l* turbulence model, in Sections 6.1.2 and 6.2, the diffusion coefficient K is computed explicitly only once by time-level n values and can be used by all three DIRK stages. Computing K is often the most

expensive part of a vertical diffusion solver and here is done only once as it is done in cheap low order schemes.

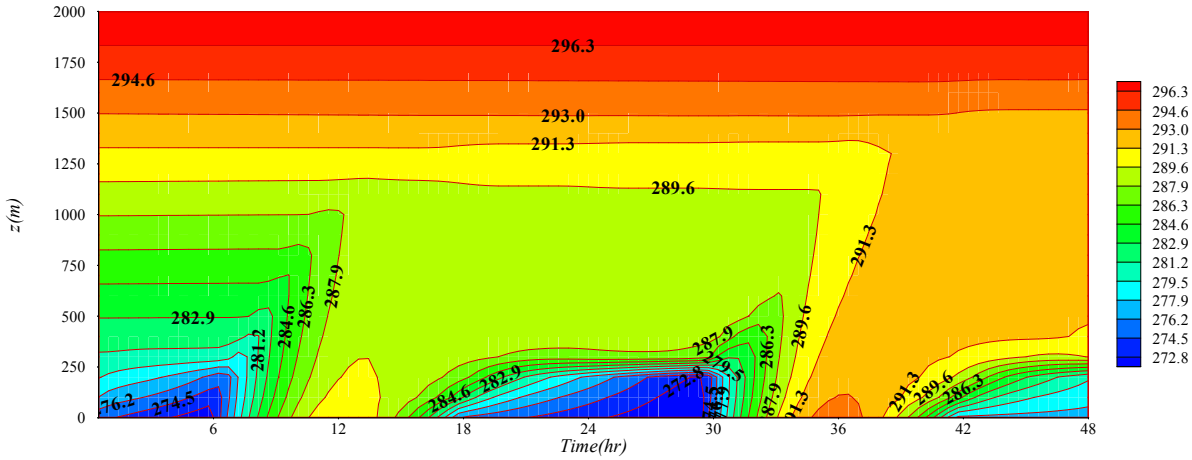

(a)

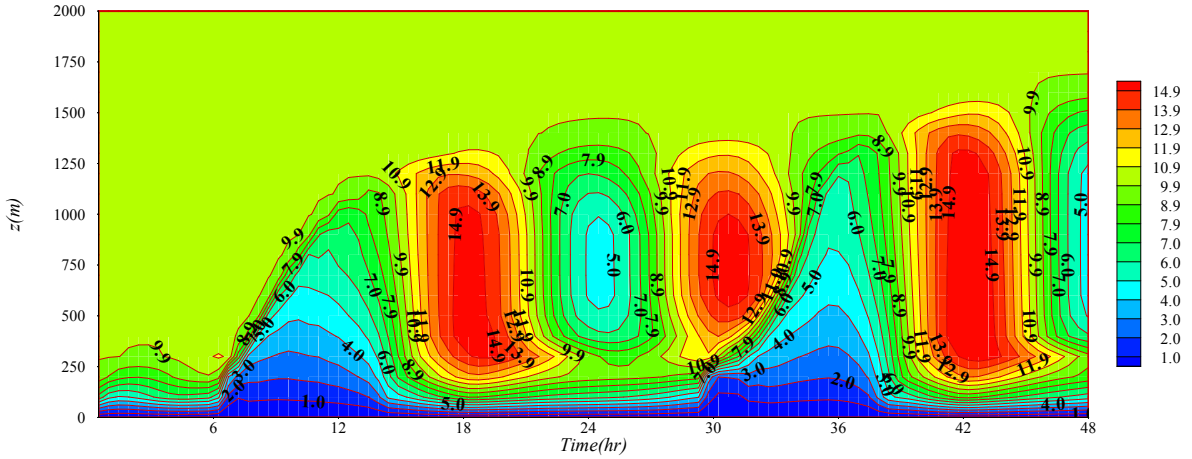

(b)

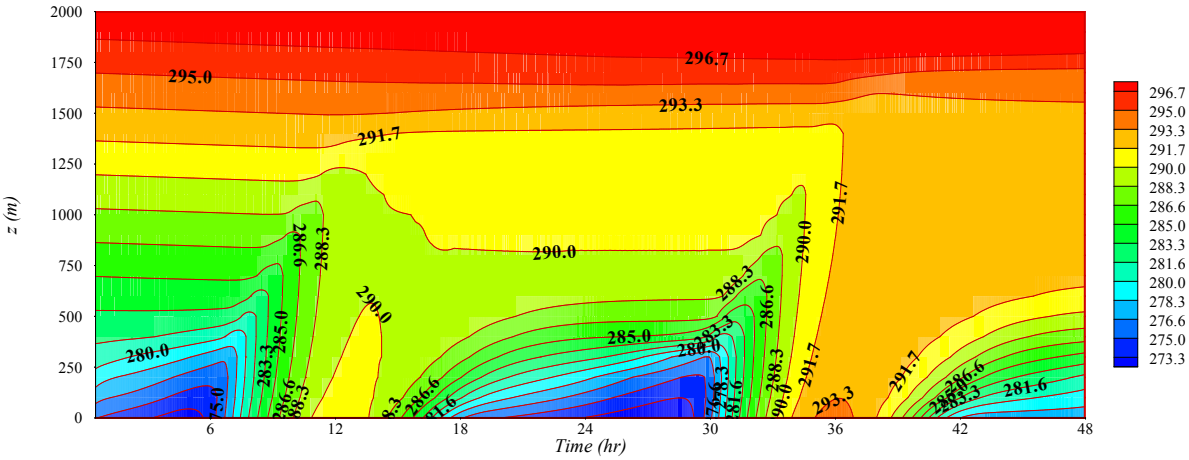
z (m)
Time (hr)
296.7
295.0
293.3
291.7
290.0
288.3
286.6
285.0
283.3
281.6
280.0
278.3
276.6
275.0
273.3

(c)

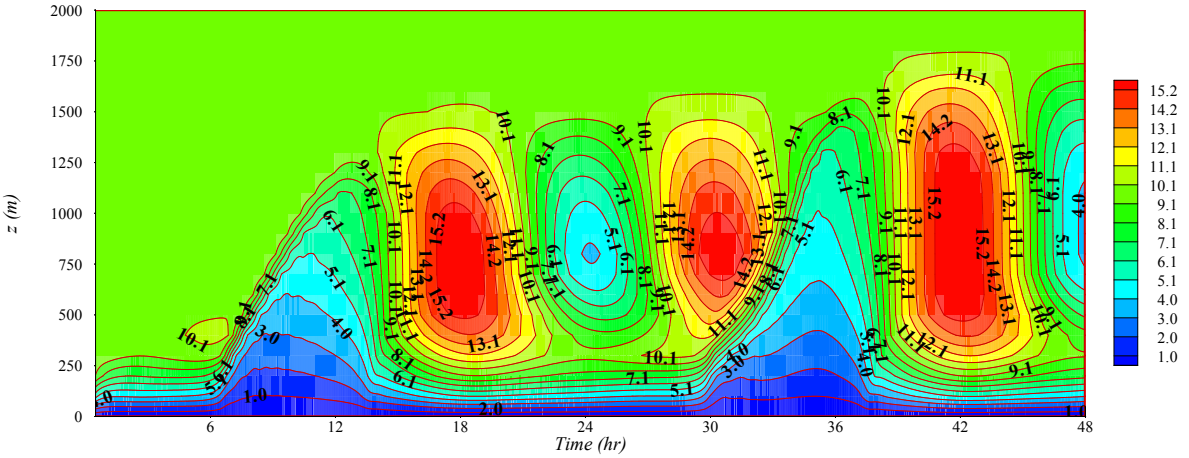
z (m)
Time (hr)
15.2
14.2
13.1
12.1
11.1
10.1
9.1
8.1
7.1
6.1
5.1
4.0
3.0
2.0
1.0

(d)

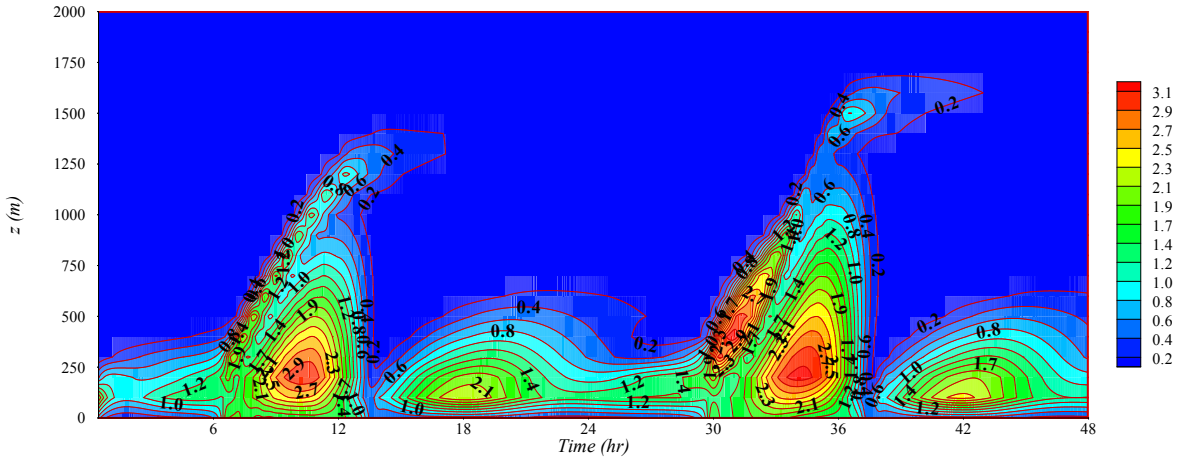

(e)

Fig. 6.4. Time-height contour plots of the diagnostic model a) potential temperature (K) and b) wind (ms^{-1}), and the *E-l* model c) potential temperature (K), d) wind (ms^{-1}), and e) turbulent kinetic energy (m^2s^{-2}) for 48-hour simulation of the second GABLS experiment day-night cycle using the proposed optimal scheme. The spatial resolution of $\Delta z = 100$ m was chosen for the model.

6.7 Conclusion

A three-stage third-order physically justified diagonally-implicit Runge-Kutta scheme was derived using the numerical stability analysis optimization. The optimization is designed to find a scheme which is close to the previously proposed ME BDF scheme (Nazari et al., 2013) in behaviour, while retains higher order accuracy. From the numerical test results, the new scheme with the optimal Err is more accurate than the mentioned ME BDF SDIRK scheme for high spatial resolutions with large time steps. Satisfactory accuracy of the new scheme is obtained for low spatial resolutions with the same time steps, additionally. The proposed optimal scheme is A-stable which makes it an appropriate choice for the solution of stiff problems to be able to capture the fast-varying solution component. Furthermore, another strength of this scheme is that the diffusion coefficient K needs to be computed in cheap partially implicit low

order schemes, which brings about more efficiency. Regarding the turbulence models, noteworthy results were obtained using the diagnostic closure model and the proposed optimal scheme for the simulation of atmospheric boundary layer with large time steps, while, at the same time, the mentioned optimal scheme works satisfactorily with other turbulence closure models i.e. *E-l*.

Acknowledgement

The research was supported by Environment Canada and Natural Sciences and Engineering Research Council of Canada.

7. High-Order Low-Dissipation Low-Dispersion Diagonally Implicit Runge-Kutta Schemes[4]

Abstract

Truly high-order low-dissipation low-dispersion diagonally implicit Runge-Kutta schemes are analyzed and introduced, based on the optimization of amplification and phase errors for wave propagation. Various optimized schemes can be obtained. The new scheme shows no dissipation. It is illustrated mathematically and numerically that the new scheme preserves fourth-order accuracy, while the recently developed diagonally implicit Runge-Kutta scheme does not. The numerical applications contain the wave equation with and without a stiff nonlinear source term and an oscillatory test. The new scheme is A-stable as desired for the solution of stiff problems.

Keywords: Low-dissipation low-dispersion; Optimal schemes; High-order accurate; Diagonally-implicit; Time integration; Runge-Kutta; Numerical wave propagation

7.1 Introduction

Multi-stage implicit Runge-Kutta schemes have been considered as an appropriate choice for the temporal integration of Navier-Stokes equations in computational fluid dynamics due to their low-storage requirements and large stability limits (Nazari et al., 2013). However, in wave propagation and computational acoustics, both dissipation and dispersion errors are of great concern and preserving the stability limits do not suffice to obtain the desirable results (Hu et al., 1996). As a result, Low-dissipative low-dispersive integration schemes have drawn attention in the simulation of these physical phenomena.

[4] This chapter has been published as Farshid Nazari, Abdolmajid Mohammadian, and Martin Charron, "High-Order Low-Dissipation Low-Dispersion Diagonally Implicit Runge-Kutta Schemes", Journal of **Computational Physics** 286 (2015) 38–48 http://dx.doi.org/10.1016/j.jcp.2015.01.020.

Spatial discretization techniques have first been under considerable investigation to have low-dissipation and low-dispersion errors. Some related studies consist of explicit DRP (Tam and Webb, 1993), compact (implicit) finite differences (Lele, 1992), and ENO schemes (Casper et al. 1994). Some efforts have also been done to introduce low-dissipative low-dispersive temporal integration schemes. Due to the benefits of Runge-Kutta schemes, Hu et al. (1996) developed low-dispersion and low-dissipation Runge–Kutta (LDDRK) schemes through the minimization of dissipation and dispersion errors. Optimized second-order single-step four-, five- and six-stage Runge-Kutta schemes in addition to optimized two-step schemes with different coefficients for the alternating steps were introduced. For the two-step methods and only six-stage single-step method, they could reach fourth-order accuracy. The study of low-dissipation low-dispersion schemes were then continued e.g. by Bogey and Bailly (2004) (second-order explicit multi-stage Runge-Kutta schemes) extended later by Berland et al. (2006) to introduce a low-storage, fourth-order accurate optimal scheme, or Stanescu and Habashi (1998) (fourth-order weakly stable six-stage explicit scheme). Finding an optimal scheme for a specific type of problem under study seems to be an appropriate and growing procedure in diverse fields of engineering; e.g. in atmospheric boundary layer (Nazari et al., 2014).

As is clear, all of the mentioned studies are related to explicit schemes. However, explicit schemes are well-known for the numerical stability concerns. To avoid instability, very small time steps may be required in some applications such as solid boundaries in flow field, which leads to high computational costs. Recently, Najafi-Yazdi and Mongeau (2013) developed a low-dissipative low-dispersive three-stage diagonally implicit Runge-Kutta scheme (ILDDRK4) which is stable and accurate for a wide range of variables. It is claimed that the scheme is fourth-order accurate. However, it can be proved mathematically and numerically that their proposed scheme cannot retain fourth-order accuracy for various problems; for instance, for the numerical approximation of systems of conservation laws with stiff nonlinear source terms, which is very common in CFD (Griffiths et al., 1992), or oscillatory problems

(Ixaru and Berghe, 2004). Therefore, in the present study, truly fourth-order low-dissipative low-dispersive three-stage *diagonally implicit Runge-Kutta* (DIRK) schemes are investigated and optimized through dissipation and dispersion analysis. The selected scheme along with ILDDRK4 scheme and fourth-order three-stage *singly-diagonally implicit Runge-Kutta* (SDIRK4) scheme are compared in terms of dissipation and dispersion, and then tested numerically by the mentioned numerical applications.

7.2 Dissipation and Dispersion Analysis of Runge-Kutta Methods

The following first-order ODE has been widely considered in the literature as an appropriate case for the numerical solution of initial value problems

$$\dot{y}(t) = f(t, y), \quad y(t_0) = y_0 \tag{7.1}$$

The numerical solution of the above ODE at the new time step is obtained by an s-stage Runge-Kutta method as follows

$$\begin{aligned} y_{n+1} &= y_n + h\sum_{i=1}^{s} b_i f(t_n + c_i h, Y_i) \\ Y_i &= y_n + h\sum_{j=1}^{s} a_{ij} f\left(t_n + c_j h, Y_j\right),\ i = 1, \dots, s \end{aligned} \tag{7.2}$$

which is denoted by the Butcher tableau of the scheme in a compact form (Butcher, 2008)

$$\begin{array}{c|c} \mathbf{c} & \mathbf{A} \\ \hline & \mathbf{b^T} \end{array} \tag{7.3}$$

where **A** is the matrix of $[a_{ij}]$ (i,j= 1, ..., s) and $\mathbf{b^T} = [b_1, ..., b_s]$ which are the weight coefficients. An explicit RK scheme gives an strictly lower triangular **A**, while for a diagonally implicit RK's (DIRK), **A** is a lower triangular with non-zero diagonal elements. **c** is the vector of c_i's which corresponds to the positions of stage values. This is an important debating point of this study. In fact, we will show in this study that for a multi-stage Runge-Kutta scheme to retain its order for different kinds of differential equations, **c** cannot be independent of **A**.

Stability and phase-lag analysis of a multi-stage DIRK scheme is based upon the test equation

$$y' = i\lambda y \tag{7.4}$$

For a multi-stage RK method, **Y** is a vector representing the stage solutions at time n+1

$$\mathbf{Y}^{\mathrm{T}} = [Y_1\ Y_2\ \ldots\ Y_s] \tag{7.5}$$

satisfies the equation

$$\mathbf{Y} = \mathbf{1}y_n + i\lambda\Delta t\mathbf{A}\mathbf{Y} = \mathbf{1}y_n + i\tau\mathbf{A}\mathbf{Y} \tag{7.6}$$

where $\tau = \lambda\Delta t$.

To obtain **Y**, rearranging Eq. (7.6) gives

$$\mathbf{Y} = (\mathbf{I} - i\tau\mathbf{A})^{-1}\mathbf{1}y_n \tag{7.7}$$

Then according to Eq. (7.2), y_{n+1} is obtained by

$$y_{n+1} = y_n + i\lambda\Delta t\mathbf{b}^T\mathbf{Y} = y_n + i\tau\mathbf{b}^T(\mathbf{I} - i\tau\mathbf{A})^{-1}\mathbf{1}y_n \tag{7.8}$$

For a numerical method, y_{n+1} can be related to y_n by an amplification factor $R(\tau)$ as

$$y_{n+1} = R(\tau)y_n \tag{7.9}$$

If $|R(\tau)| < 1$, then the numerical solution will be stable, which means it remains bounded when moving further away from the starting point. $R(\tau)$ is called *stability function* consequently and from Eq. (7.8) will be

$$R(\tau) = 1 + i\tau\mathbf{b}^T(\mathbf{I} - i\tau\mathbf{A})^{-1}\mathbf{1} \tag{7.10}$$

Knowing that the analytical amplification is

$$R_a = e^{i\tau} \tag{7.11}$$

the error function can be defined as the ratio of the numerical amplitude to the analytical one

$$E(\tau) = \frac{R(\tau)}{R_a} = |E(\tau)|e^{i\varphi} \tag{7.12}$$

The amplification (dissipation) and phase (dispersion) errors are represented in Eq. (7.12) by $|E(\tau)|$ and the phase difference angle, φ, respectively. A low-dissipation low-dispersion scheme is the one which maintains $|E(\tau)| = 1$ and $\varphi = 0$ up to reasonable

values of τ, inferring that a scheme which can retain these characteristics for larger values of τ is superior.

7.3 Fourth-Order Diagonally-Implicit Runge-Kutta Scheme

A low-dissipation low-dispersion Runge-Kutta scheme can be obtained by finding matrix (7.3) coefficients such that the error function (7.12) has its least value for an appropriate interval of τ, while the order conditions (7.14)-(7.17) are also satisfied for fourth-order accuracy. But, the main discussion here is on the dependency of c_i values on a_{ij}'s. In Najafi-Yazdi and Mongeau (2013), c_i's are treated as free parameters, which infers that there is no relation between c_i's and a_{ij}'s.

In the mathematical approach, the condition $c_i = \sum_{j=1}^{s} a_{ij}$ is something that is hard to avoid. A differential equation $\dot{\mathbf{Y}}(t) = \mathbf{F}(t, \mathbf{Y})$ can always be converted into another equation $\dot{\mathbf{Z}} = \mathbf{G}(\mathbf{Z})$ where $\mathbf{Z}$ is N+1 dimensional and the first N components are the same as $\mathbf{Y}$ and the last component has the same value as t. The first N components of the function $\mathbf{G}(\mathbf{Z})$ are the same as $\mathbf{F}(z_{N+1}, [z_1, \dots, z_N])$ and the last component always has the value 1. The results produced by an RK method applied to the two problems only give the same answer if $c_i = \sum_{j=1}^{s} a_{ij}$. Further explanation and mathematical justifications are presented in Appendix A. In the following sections, it will also be shown using numerical experiments in Section 7.4 that the optimized scheme in this study which satisfies this condition maintains fourth order accuracy, while the optimized scheme by Najafi-Yazdi and Mongeau (2013) does not.

The Butcher tableau of a 3-stage DIRK scheme considered for the optimization in this study is

$$\begin{array}{c|ccc} c_1 & a_{11} & 0 & 0 \\ c_2 & a_{21} & a_{22} & 0 \\ c_3 & a_{31} & a_{32} & a_{33} \\ \hline & b_1 & b_2 & b_3 \end{array} \tag{7.13}$$

As can be seen, matrix **A** is lower triangular for a DIRK scheme. The advantage of DIRK schemes with respect to fully implicit Runge-Kutta schemes is that the solutions at each stage is uncoupled from other stages, so each stage can be solved independently. This brings about computational efficiency and faster convergence in the iterative methods. If all diagonal elements are equal, furthermore, the DIRK scheme will be called *singly-diagonally-implicit Runge-Kutta* (SDIRK). We do not enforce this condition for the optimization to let more free parameters be involved.

The following conditions need to be satisfied for a Runge-Kutta scheme to be fourth order at least:

$$\sum_{i=1}^{s} b_i = 1 \tag{7.14}$$

for first order accuracy,

$$\sum_{i=1}^{s} b_i c_i = \frac{1}{2} \tag{7.15}$$

for second order accuracy,

$$\sum_{i=1}^{s} b_i {c_i}^2 = \frac{1}{3} \tag{7.16}$$

$$\sum_{i=1}^{s}\sum_{j=1}^{s} b_i a_{ij} c_j = \frac{1}{6}$$

for third order accuracy, and

$$\begin{aligned}
\sum_{i=1}^{s} b_i {c_i}^3 &= \frac{1}{4} \\
\sum_{i=1}^{s}\sum_{j=1}^{s} b_i c_i a_{ij} c_j &= \frac{1}{8} \\
\sum_{i=1}^{s}\sum_{j=1}^{s} b_i a_{ij} {c_j}^2 &= \frac{1}{12} \\
\sum_{i=1}^{s}\sum_{j=1}^{s}\sum_{l=1}^{s} b_i a_{ij} a_{jl} c_l &= \frac{1}{24}
\end{aligned} \tag{7.17}$$

for fourth order accuracy.

7.4 Low-Dissipation Low-Dispersion Fourth-Order Three-Stage DIRK Scheme

Optimal DIRK schemes have been studied and introduced for the solution of specific nonlinear diffusive systems by the authors (Nazari et al., 2014). There exist three fourth-order three-stage *SDIRK* methods (Ferracina and Spijker, 2008); however, three-stage *DIRK* schemes are considered here to relax the constraints for the optimization process and obtain more schemes. The two coefficients of a_{11} and a_{22} are chosen as the free parameters to be investigated for the minimization of dissipation and dispersion. To clarify the stability and phase behavior of a three-stage fourth-order

DIRK scheme, the components of the error function, $E(\tau)$, are plotted in Fig. 7.1.a with the axes representing the variable coefficients, a_{11} and a_{22}, and τ.

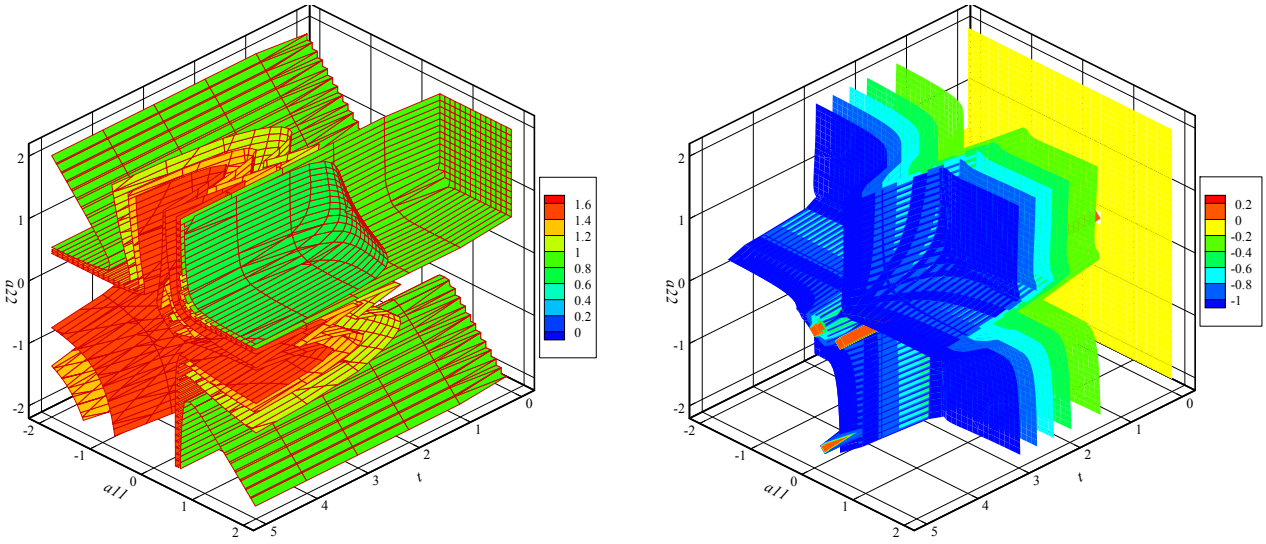

(a)

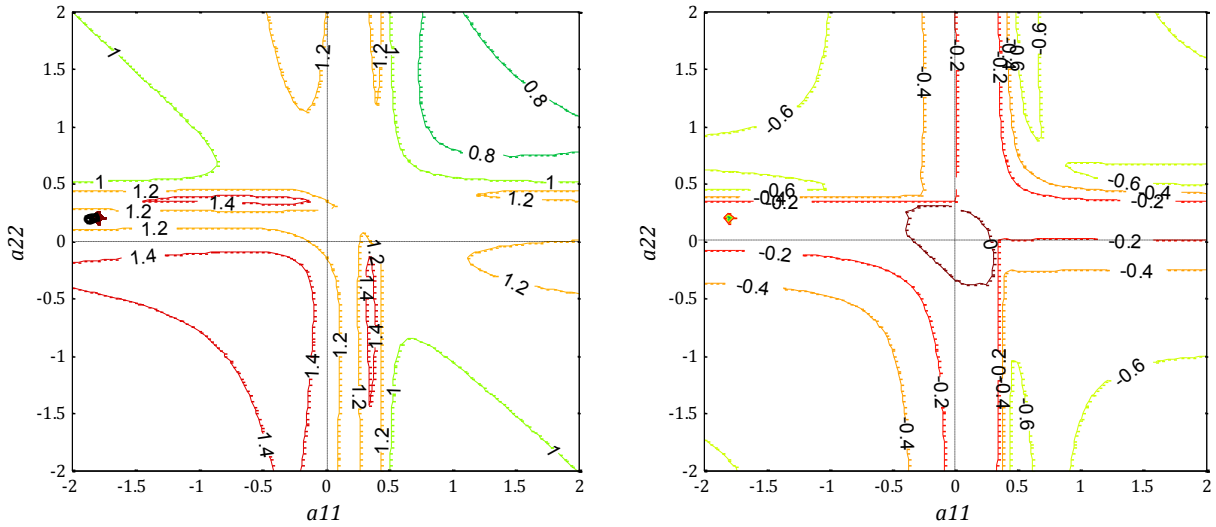

(b)

Fig. 7.1. The amplification factor and phase angle for three-stage fourth order DIRK schemes with variable a_{11} and a_{22} coefficients (a) for different τ's, and (b) at $\tau = 2.4$.

As can be seen, for a range of τ values, $|E(\tau)|$ in Fig. 7.1.a (left) remains constant for specific values of a_{11} and a_{22} except for the a_{11} and a_{22} values very close to zero and for a limited region in the first quarter (where both a_{11} and a_{22} are positive) for larger values of τ; but as far as $|E(\tau)| = 1$ is concerned (no dissipation error), the plane is always corresponding to the same values of a_{11} and a_{22} when τ is varying. Obviously from Fig. 7.1.a (right), the phase error is amplifying with increasing τ and is constant for a specific τ value for different values of a_{11} and a_{22}, except when a_{11} and a_{22} are very close to zero again. Hence, a slice of the planes are shown in Fig. 7.1.b for $\tau = 2.4$ to have a better image of the dissipation and dispersion errors. There exist the $|E(\tau)| = 1$ line in three quarters; in the quarter with both a_{11} and a_{22} negative, the absolute value of the $E(\tau)$ is greater than 1, so the scheme is always unstable in that quarter. The second and the fourth quarters look similar. They show that the values of a_{11} and a_{22} are interchangeable when one of them has the opposite sign. There exist a point where the slope changes for the line of interest, $|E(\tau)| = 1$, in these quarters. In the first quarter where both a_{11} and a_{22} are positive, the point of changing slope is almost the point of *singly-diagonally* scheme: a_{11}= a_{22}. To find the accurate coefficients for the desired scheme, we try optimization in all regions. After finding the coefficients, the stability and phase behaviours of obtained scheme as well as their performances on numerical tests are compared and the optimal scheme is selected.

As suggested by Hu et al. (1996), the coefficients are determined to minimize the error

$$Err(T) = \int_0^T \left|R(\tau) - e^{i\tau}\right|^2 d\tau \tag{7.18}$$

where T is determined according to the range of τ for which the scheme is optimized for. To search only for absolutely stable (A-stable) schemes, not to encounter instability problems, the constraint $|E(\tau)| \leq 1$ is applied in the optimization for all values of τ. As

a result, we have a constrained optimization problem with the objective function (7.18). A value of $T = 2$ is chosen for the optimization.

7.4.1 Dissipation and dispersion comparisons

The amplification factor, $|E(\tau)|$, and phase difference angle, φ, are plotted for the three different schemes of the new optimized scheme, ILDDRK4 scheme, and SDIRK4 (a three-stage fourth-order SDIRK) scheme in Fig. 7.2. It is interesting to know that we observed the exactly same behaviour for the amplification and phase for the optimized schemes in different regions (quarters 1, 2, and 4). It was expected that for quarters 2 and 4, we obtain the exchanged values for a_{11} and a_{22} for the optimized schemes since these regions are mirrors; but the same behaviour is also observed for the optimized scheme in the first quarter (positive a_{11} and a_{22}). Therefore, we just demonstrate one optimized scheme behaviour in Fig. 7.2, valid for the other two optimized schemes, and the selected optimized parameters are presented in Table 7.1. The noteworthy fact is that the optimized schemes show no dissipation since they are on the $|E(\tau)| = 1$ plane in Fig. 7.1.a (left) and the amplification factor does not change with respect to τ, consequently. Hence, there is no doubt that the optimized scheme has far better performance regarding the numerical dissipation than the ILDDRK4 and SDIRK4. The new optimized scheme is expected to be unconditionally stable since its amplification factor is less than or equal to unity for all values of $\mathrm{Re}(\tau) \in [0, \infty[$. According to Fig. 7.2.b (right), the new proposed optimized scheme suggests less dispersion error than the other two schemes for small values of τ. For large values of τ, similar behaviour to SDIRK4 (slightly less dispersion error) is observed for the new scheme, while ILDDRK4 scheme demonstrates less dispersion. Corresponding τ values to specific accuracy (dissipation and dispersion) limits are also cited in Table 7.2. It elaborates that the new optimized scheme never reaches the dissipation error mentioned in Table 7.2 as a consequence of its no dissipation property, while the ILDDRK4 reaches the dissipation limit at a τ approximately twice as large as the τ for SDIRK4. The τ for the dispersion

Table 7.1. The new optimal three-stage fourth-order low-dissipation low-dispersion DIRK scheme.

Parameter	Value
a_{11}	0.675592332328701
a_{21}	1.351242940337120
a_{22}	-0.851207182169909
a_{31}	1.351467284887694
a_{32}	-1.702697002012658
a_{33}	0.675614858562624
b_1	1.351467260320785
b_2	-1.702414526538024
b_3	1.350947266217122

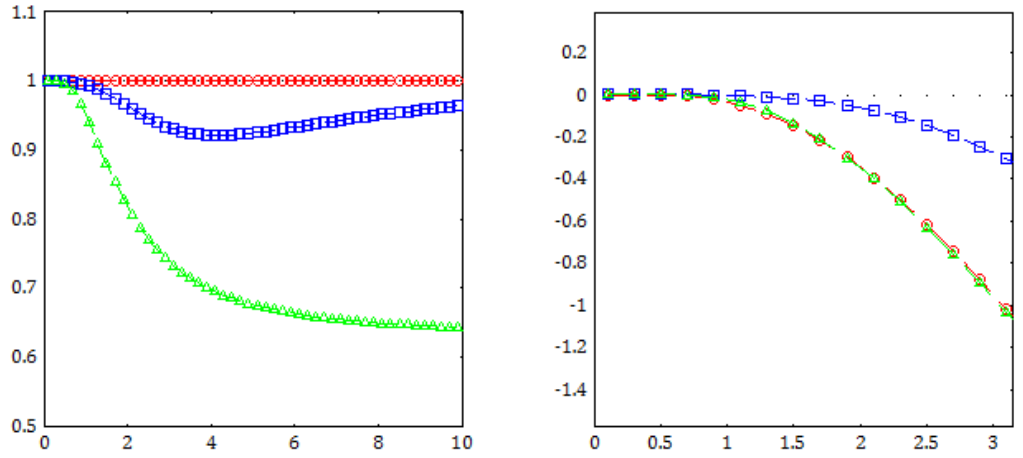

(a)

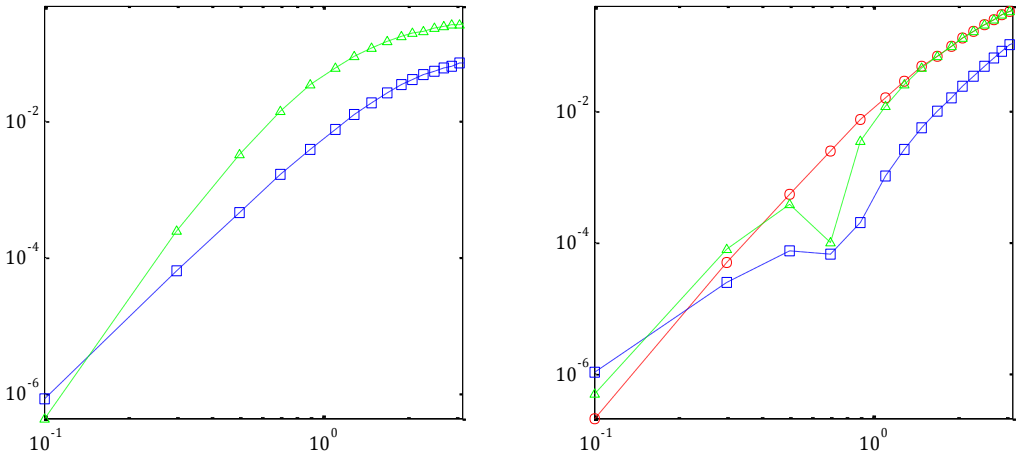

(b)

Fig. 7.2. (a) The amplification factor and phase difference, and (b) dissipation and dispersion errors in logarithmic scale, for the Runge-Kutta schemes; the new scheme (circle), ILDDRK4 (square), and SDIRK4 (triangle).

limit is slightly larger for the ILDDRK4 than for the new scheme. The smallest τ is for SDIRK4.

Table 7.2. The accuracy limits for the Runge-Kutta schemes in terms of τ. The values correspond to $1 - |E(\tau)| \leq 0.01$ for the dissipation error and $|\varphi(\tau)| \leq 5 \times 10^{-5}$ for the dispersion error.

τ values	ILDDRK4	New scheme	SDIRK4
τ for dissipation limit	1.198642042272213	∞	0.643199095003643
τ for dispersion limit	0.258456623142471	0.239797329869547	0.207553240787709

7.5 Numerical Experiments

To investigate the accuracy of the new proposed optimal scheme along with the ILDDRK4 and SDIRK4 schemes, two different numerical tests are implemented. In the first test, a periodic function is considered representing the periodical initial value problems (Ixaru and Berghe, 2004). The advection equation with a nonlinear source term is considered as the second test (Griffiths et al., 1992).

7.5.1 Periodic test

$$y'' = -\kappa^2 y + (\kappa^2 - \omega^2)\sin(\omega x), \quad x \geq 0, \quad y(0) = y_0, \quad y'(0) = y'_0 \tag{7.19}$$

with the analytical solution

$$y(x) = y_0 \cos(\kappa x) + \frac{(y'_0 - \omega)\sin(\kappa x)}{\kappa} + \sin(\omega x) \tag{7.20}$$

is considered to verify the performance of the schemes under study for oscillatory problems.

Two frequencies κ and ω are here involved. Assuming $y_0 = 0$ and $y'_0 = \omega$, the solution

is simply $y(x) = \sin(\omega x)$. The components with frequency κ are then eliminated from the whole solution. The values of $\omega = 10$ and $\kappa = 15$ are taken as the constant frequencies. The new optimized scheme and ILDDRK4 and SDIRK4 are used to numerically solve Eq. (7.19). To precisely compare the orders of accuracy of the two schemes, the x increment, Δx, is considered as 0.001 and then increased by the order of 2^n for the nth test. Table 7.3 shows the errors for the schemes under investigation. Since the test equation (7.19) is ODE, the error is simply considered as the difference between the numerical and the analytical solution at the point where the maximum of the function $y(x)$ occurs ($x \cong 0.785$). As plotted in Fig. 7.3 in logarithmic scale, the error is decreased by the order of 4 for the new optimized scheme, while the ILDDRK4 error is only reduced by the order of 2; which confirms that the order of accuracy of the new LDD DIRK scheme is truly 4, but the ILDDRK4 order of accuracy is 2. For more clarification, a decrease in Δx by a factor of 2, results in a reduction of the error by a factor of almost 16 for the new DIRK scheme, while the error of the ILDDRK4 is only reduced roughly by a factor of 4.

Table 7.3. Errors between the numerical and the analytical solution for the Runge-Kutta schemes.

Δx	ILDDRK4	New scheme	SDIRK4
0.001	2.0770e-006	6.6703e-009	1.4804e-008
0.002	8.0890e-006	1.0603e-007	2.3047e-007
0.004	3.1562e-005	1.7126e-006	3.5668e-006
0.008	1.1454e-004	2.7162e-005	5.0077e-005

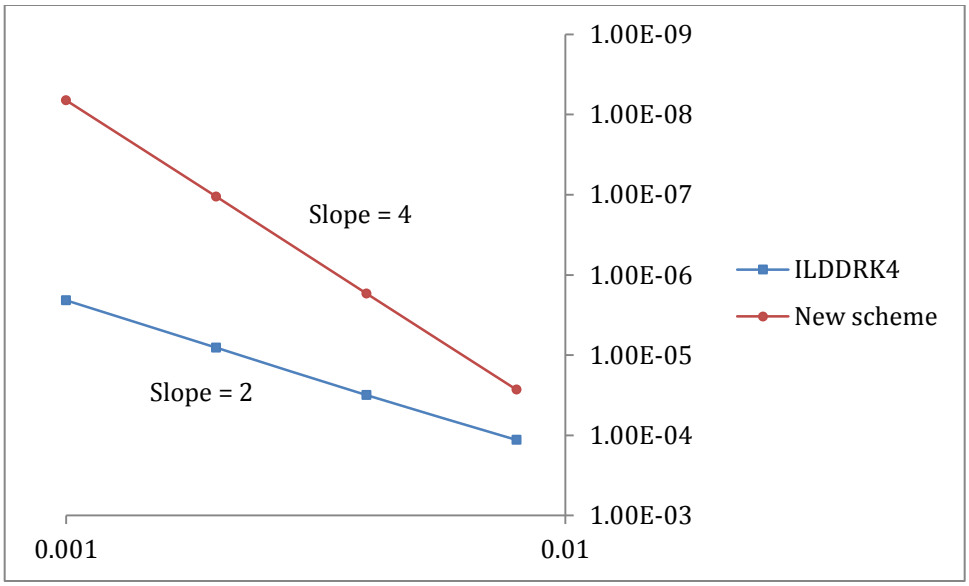

Fig. 7.3. Error between the numerical and the analytical solutions for the Runge-Kutta schemes in logarithmic scale. The slope shows the order of accuracy.

7.5.2 Advection equation with and without a nonlinear source term

The advection equation with and without a stiff nonlinear source term

$$u_t + u_x = f(u) \tag{7.21}$$

is considered. According to Griffiths et al. (1992), the function $f(u)$ is assumed to satisfy the following conditions:

I. $f(u) \in C^2([0,1], R)$;
II. $f(0) = f(1) = 0$ and $f(u) > 0$ for $u \in (0,1)$;
III. $f'(0) > 0, f'(1) < 0$.

A typical example of a nonlinear source term satisfying I-III is $f(u) = u - u^2$. Such systems arise, for instance, as models of nonequilibrium gas dynamics (Griffiths et al., 1992). A wave with the amplitude of $u(t = 0, 2 < x < 4) = 1$ is imposed as the initial condition. The new optimized three-stage fourth-order DIRK scheme and ILDDRK4 are used as the temporal integration schemes for the numerical solution of Eq. (7.21). Since we are only concerned about the order of accuracy of the temporal schemes, the upwind scheme is used as the spatial discretization. However, a fine mesh with $\Delta x \cong 0.05$ is used to make the spatial discretization error very small. Three CFL numbers of 0.1, 0.2, and 0.4 are then used to compare the errors and their rate of change for the schemes under study. The L_2 norm (Euclidean) of the error is defined as

$$L_2(e) = \left[\int_0^{x_{max}} \left(u_{reference} - u_{numerical}\right)^2\right]^{1/2} \tag{7.22}$$

where $u_{reference}$ is the computed u profile with CFL=0.01. A long-range wave propagation with $t = 100$ s is carried out for the linear advection test ($f(u) = 0$), which is widely applicable in computational acoustics. The corresponding L_2 norms of the errors for the schemes under investigation are shown in Table 7.4. A sample solution of Eq. (7.21) with the nonlinear source term is also shown in Fig. 7.4 for every 2 seconds using the new scheme. The numerical solution is obtained through iterations at each stage due to the implicit temporal scheme. The L_2 norms of the errors in Table 7.5 are computed and compared at $t \cong 1.4$ s for this test since the long-range results, as can be inferred from Fig. 7.4, are converging to the constant velocity ($u = 1$). As plotted in Fig. 7.5 in logarithmic scale, it can be seen again that decreasing the CFL number to the half leads to the reduction of the L_2 norm of the error by the order of 16 for the new optimized scheme, while the ILDDRK4 L_2 error is only reduced by the order of 4. It is worth noting that SDIRK4 becomes unstable for CFL=0.5.

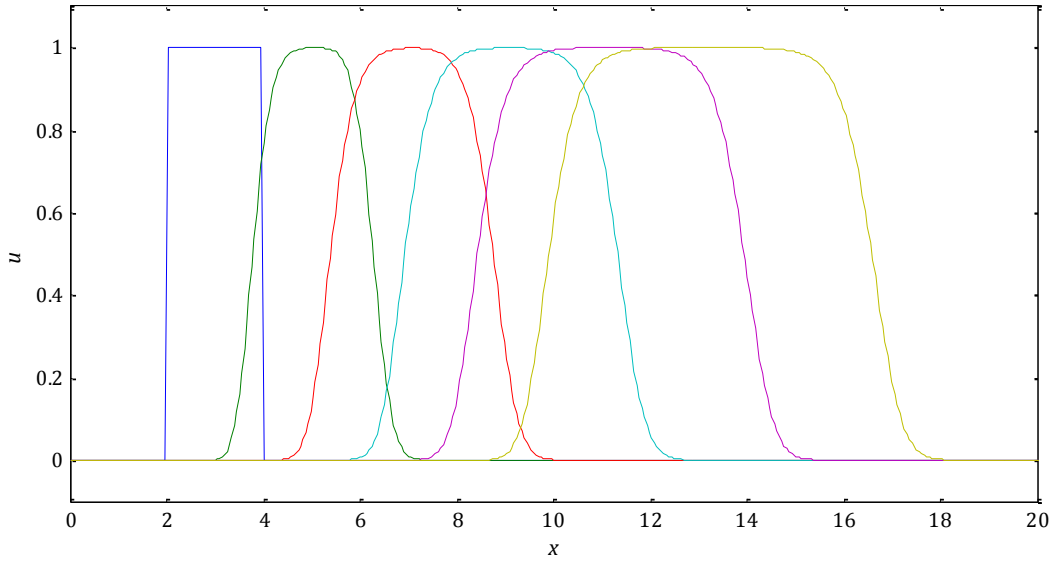

Fig. 7.4. Sample solution of Eq. (7.21) with the nonlinear source tem using the new optimized scheme with CFL=0.4 every 2 seconds.

Table 7.4. Errors between the numerical and the reference solution for the Runge-Kutta schemes for the linear advection test.

CFL	ILDDRK4	New scheme	SDIRK4
0.1	8.4461e-006	4.2618e-008	1.0564e-007
0.2	3.3711e-005	6.8234e-007	1.6788e-006
0.4	1.3444e-004	1.0882e-005	2.6449e-005

Table 7.5. Errors between the numerical and the reference solution for the Runge-Kutta schemes for the advection test with a nonlinear source term.

CFL	ILDDRK4	New scheme	SDIRK4
0.1	2.2926e-005	2.2485e-007	5.5557e-007
0.2	9.2824e-005	3.5808e-006	8.5600e-006
0.4	3.8106e-004	5.6079e-005	1.2807e-004

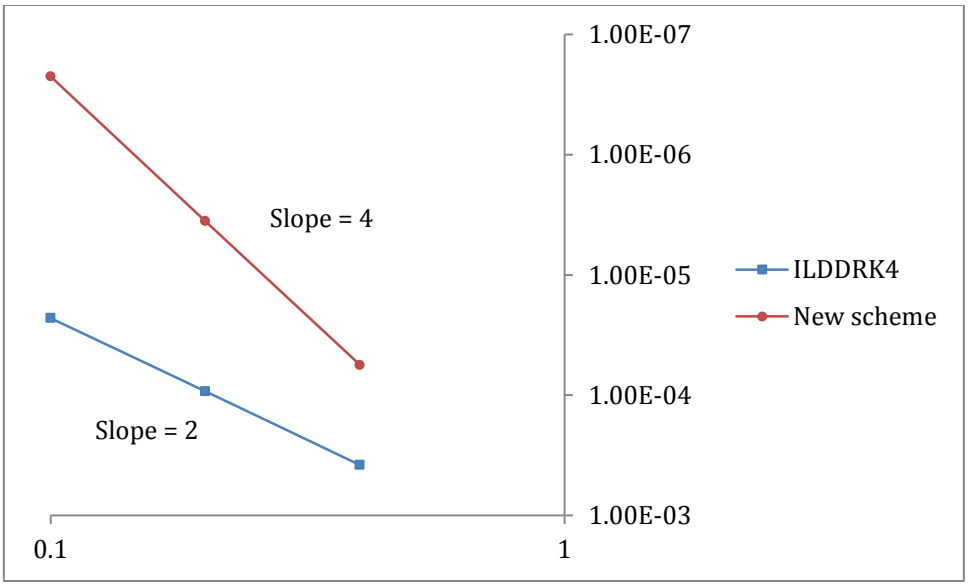

Fig. 7.5. Error between the numerical and the reference solutions for the Runge-Kutta schemes in logarithmic scale. The slope shows the order of accuracy.

7.6 Conclusion

A truly fourth-order low-dissipation low-dispersion three-stage DIRK scheme was introduced. A comprehensive analysis of stability and phase behaviours of three-stage fourth-order DIRK schemes was performed. It shows that it is possible to find different optimized DIRK schemes. The selected new scheme is A-stable and exhibits no dissipation. It was then applied to some numerical experiments i.e. a periodic function for oscillatory problems, and the advection equation with a stiff nonlinear source term. These tests prove that a Runge-Kutta scheme coefficients in its Butcher tableau should satisfy the condition $c_i = \sum_{j=1}^{s} a_{ij}$ other than the order conditions to preserve the order of accuracy. Furthermore, it was shown mathematically that for a Runge-Kutta scheme, the mentioned condition is hard to avoid. As a result, the new low-dissipation low-dispersion DIRK scheme maintains fourth-order accuracy for various problems, but the ILDDRK4 is not necessarily fourth-order for different problems.

Acknowledgements

The authors wish to thank Professor John C. Butcher for his invaluable comments. This research was supported by Environment Canada and Natural Sciences and Engineering Research Council of Canada.

7.7 Appendix A. Mathematical Justification

For further explanation of the importance of the condition $c_i = \sum_{j=1}^{s} a_{ij}$, consider the following differential equation

$$\dot{\mathbf{Y}}(t) = \mathbf{F}(t, \mathbf{Y}), \quad \mathbf{Y}(t_0) = \mathbf{Y}_0 \tag{7.23}$$

The differential equation can always be converted into another equation

$$\dot{\mathbf{Z}} = \mathbf{G}(\mathbf{Z}) \tag{7.24}$$

where $\mathbf{Z}$ is N+1 dimensional and the first N components are the same as $\mathbf{Y}$ and the last component has the same value as t

$$\mathbf{Z} = \begin{bmatrix} \mathbf{Y} \\ t \end{bmatrix} \tag{7.25}$$

The first N components of the function $\mathbf{G}(\mathbf{Z})$ are the same as $\mathbf{F}(z_{N+1}, [z_1, \ldots, z_N])$ and the last component always has the value 1. Hence

$$\mathbf{G}(\mathbf{Z}) = \begin{bmatrix} \mathbf{F}(\mathbf{Z}) \\ 1 \end{bmatrix} \tag{7.26}$$

The Runge-Kutta coefficients of rate of change ($\mathbf{K}_i$'s) are then obtained by

$$\mathbf{K}_i = \mathbf{G}\left(\mathbf{Z}_n + h\sum_{j=1}^{s} a_{ij}\mathbf{K}_j\right) = \begin{bmatrix}\mathbf{F}\left(\mathbf{Z}_n + h\sum_{j=1}^{s} a_{ij}\mathbf{K}_j\right)\\ 1\end{bmatrix}. \tag{7.27}$$

As mentioned in Eq. (7.2), the stage solutions can be written as

$$\mathbf{Z}_i = \mathbf{Z}_n + h\sum_{j=1}^{s} a_{ij}\mathbf{K}_j\,, \qquad i = 1, \dots, s \tag{7.28}$$

which can thus be written as

$$\begin{bmatrix}\mathbf{Y}_i\\ t_i\end{bmatrix} = \begin{bmatrix}\mathbf{Y}_n\\ t_n\end{bmatrix} + h\sum_{j=1}^{s} a_{ij}\begin{bmatrix}\mathbf{F}\left(\mathbf{Z}_n + h\sum_{p=1}^{s} a_{jp}\mathbf{K}_p\right)\\ 1\end{bmatrix} \tag{7.29}$$

according to Eqs. (7.25) and (7.27). On the other hand, by considering Eq. (7.23) before converting, the stage solutions according to Eq. (7.2) are simply

$$\mathbf{Y}_i = \mathbf{Y}_n + h\sum_{j=1}^{s} a_{ij}\mathbf{F}\left(t_n + c_j h, \mathbf{Y}_j\right), \qquad i = 1, \dots, s \tag{7.30}$$

The above equation shows that the t position of the i^{th} stage solution is $t_i = t_n + c_i h$ and Eq. (7.29) illustrates that $t_i = t_n + h\sum_{j=1}^{s} a_{ij}$. Thus, the two solutions will only be the same if

$$c_i = \sum_{j=1}^{s} a_{ij} \ . \tag{7.31}$$

7.8 Appendix B. Optimized Schemes

Table 7.6. Optimal three-stage fourth-order low-dissipation low-dispersion DIRK schemes in different regions of Fig. 7.1. The same dissipation and dispersion behaviour is observed as Fig. 7.2.

Parameter	Value
a_{11}	-0.851263454665540
a_{21}	0.221282760003727
a_{22}	0.675716813905398
a_{31}	-0.078577212831902
a_{32}	-0.272422066827441
a_{33}	0.675499639829671
b_1	0.006645466304608
b_2	0.320198061838696
b_3	0.673156471856696

Parameter	Value
a_{11}	0.678600761183237
a_{21}	-0.565323026062134
a_{22}	0.672651748784065
a_{31}	-8.40434658678138
a_{32}	11.1068590723148
a_{33}	-0.851256242766855
b_1	0.667655846089925
b_2	0.325888518017914
b_3	0.006455635892161

8. Summary and Concluding Remarks

The objective of this research study was to improve the stability, accuracy, and efficiency of the methods currently used by Environment Canada and other NWP research centres in their numerical models for weather and climate prediction, specifically for the ABL forecast. In the proposed numerical methods, new techniques are developed to ensure a large domain of stability. These new techniques also guarantee good qualities of the numerical solutions in ABL modeling in terms of accuracy, even for large time steps. The use of large time steps reduces the computational cost of the proposed schemes. This thesis demonstrates that the author's effort to improve the numerical performance of previously known numerical methods which have been implemented operationally at several weather and climate prediction centres has been successful.

The ME BDF scheme proposed in Chapter 4 is highly stable and efficient to apply. It maintains A- and B-stability properties and leads to negligible errors over a wide range of nonlinearity. The scheme was applied to commonly used nonlinear systems in the atmospheric boundary layers, and acceptable results were obtained. It greatly improves the stability and accuracy of the numerical results. Unlike previous schemes, it is highly non-sensitive to spatial and temporal resolutions, while being easy and efficient to implement.

Optimal SDIRK methods were studied in Chapter 5 from different aspects in order to evaluate the performance of such schemes for the solution of nonlinear stiff ODEs and PDEs. The numerical experiments consisted of damping and diffusion equations commonly applied in atmospheric boundary layer modeling, i.e., air-ground heat exchange and wind velocity distribution. Two ME BDF SDIRK schemes were also proposed which are computationally cheaper than the first ME BDF scheme proposed in Chapter 5, but they are still first-order.

Chapter 6 delineates our search to find a higher-order scheme that can be as powerful as (or more so than) the previously proposed ME BDF scheme in Chapter 4.

As a result, a three-stage third-order physically justified DIRK scheme was then derived through numerical stability analysis optimization. The optimization was designed in such a way that the new optimal scheme be close to the mentioned ME BDF scheme in behaviour while retaining higher-order accuracy. The numerical test results also show that for high spatial resolutions with large time steps, the new optimal scheme is more accurate than the ME BDF scheme. As well, satisfactory accuracy of the new scheme is obtained for low spatial resolutions with the same time steps. The proposed optimal scheme is necessarily A-stable, since the A-stability condition was imposed in the optimization process. Regarding the turbulence models, noteworthy results were obtained in this chapter using the diagnostic closure model and the proposed optimal scheme for the simulation of the ABL with large time steps, while at the same time the mentioned optimal scheme works satisfactorily with other turbulence closure models, i.e., *E*-*l*.

It is worth mentioning that in all the above chapters, the diffusion coefficient K may be computed in cheap, partially implicit low-order schemes, which brings about more computational efficiency. Computing K is often the most expensive part of a vertical diffusion solver in atmospheric models.

Finally, in Chapter 7, a fourth-order low-dissipation low-dispersion three-stage DIRK scheme was introduced. A comprehensive analysis of stability and phase behaviours of fourth-order three-stage DIRK schemes was performed, and non-dissipative schemes were obtained. The new scheme was then applied to some numerical experiments for oscillatory problems and advections with a stiff nonlinear source term, which arise, for instance, in models of non-equilibrium gas dynamics.

This thesis proves that there exists a vast variety of research possibilities in the field of numerical methods in atmospheric models. Specifically in this thesis, the focus was mostly on the atmospheric boundary layer, which possesses a high degree of nonlinearity and stiffness, which is the source of many subsequent numerical problems. The author approached the problem from various aspects and obtained

satisfactory results which greatly improve the existing numerical methods for simulation of the atmospheric boundary layer in NWP models.

8.1 Future Studies

Many other aspects still exist for further research into the numerical methods. As an example, our focus was on temporal integration schemes, whereas much research can be carried out on spatial discretization schemes. Furthermore, as demonstrated in Chapter 7, one is able to expand this research on different optimal schemes for the solution of nonlinear advection, advection-diffusion, and advection-diffusion-reaction problems, all very common in different fields of computational fluid dynamics. To elaborate, *implicit-explicit* (IMEX) methods can be recast in the general framework of multi-rate methods (Gunther et al., 2001) where the operators are partitioned into fast- and slow-moving processes. The author with his collaborators is working on optimal IMEX schemes which show low-dissipation low-dispersion behaviours and thus can be widely applicable in CFD problems. For instance, the IMEX methods used in numerical approaches in atmospheric models approximating the full compressible equations treat sound waves in a stable but inaccurate manner, while faithfully estimating the behaviour of the slower-moving waves (Durran and Blossey, 2012).

References

André, J. C., De Moor, G., Lacarrere, P., & Du Vachat, R. (1978). Modeling the 24-hour evolution of the mean and turbulent structures of the planetary boundary layer. *Journal of the Atmospheric Sciences*, *35*(10), 1861-1883.

Atkinson, K. E., Han, W., & Stewart, D. E. Numerical Solution of Ordinary Differential Equations. 2009.

Beare, R. J., Macvean, M. K., Holtslag, A. A., Cuxart, J., Esau, I., Golaz, J. C., ... & Sullivan, P. (2006). An intercomparison of large-eddy simulations of the stable boundary layer. *Boundary-Layer Meteorology*, *118*(2), 247-272.

Beljaars, A. C. M. (1991, September). Numerical schemes for parametrizations. In *Proc. ECMWF Seminar on Numerical Methods in Atmospheric Models* (Vol. 2, pp. 1-42).

Bénard, P., Marki, A., Neytchev, P. N., & Prtenjak, M. T. (2000). Stabilization of nonlinear vertical diffusion schemes in the context of NWP models. *Monthly Weather Review*, *128*(6), 1937-1948.

Berland, J., Bogey, C., & Bailly, C. (2006). Low-dissipation and low-dispersion fourth-order Runge–Kutta algorithm. *Computers & Fluids*, *35*(10), 1459-1463.

Blackadar, A. K. (1962). The vertical distribution of wind and turbulent exchange in a neutral atmosphere. *Journal of Geophysical Research*, *67*(8), 3095-3102.

Bogey, C., & Bailly, C. (2004). A family of low dispersive and low dissipative explicit schemes for flow and noise computations. *Journal of Computational Physics*, *194*(1), 194-214.

Burrage, K., & Butcher, J. C. (1979). Stability criteria for implicit Runge-Kutta methods. *SIAM Journal on Numerical Analysis*, *16*(1), 46-57.

Businger, J. A. (1982). Equations and concepts. In *Atmospheric Turbulence and Air Pollution Modelling* (pp. 1-36). Springer Netherlands.

Butcher, J. C. (1987). *The numerical analysis of ordinary differential equations: Runge-Kutta and general linear methods*. Wiley-Interscience.

Butcher, J. C. (2008). *Numerical methods for ordinary differential equations*. John Wiley & Sons.

Cash, J. R. (1980). On the integration of stiff systems of ODEs using extended backward differentiation formulae. *Numerische Mathematik*, *34*(3), 235-246.

Cash, J. R. (1983). The integration of stiff initial value problems in ODEs using modified extended backward differentiation formulae. *Computers & mathematics with applications*, *9*(5), 645-657.

Cash, J. R. (1984). Two new finite difference schemes for parabolic equations.*SIAM journal on numerical analysis*, *21*(3), 433-446.

Casper, J., Shu, C. W., & Atkins, H. (1994). Comparison of two formulations for high-order accurate essentially nonoscillatory schemes. *AIAA journal*, *32*(10), 1970-1977.

Cuxart, J., Holtslag, A. A., Beare, R. J., Bazile, E., Beljaars, A., Cheng, A., L. Conangla, M. Ek, F. Freedman, R. Hamdi, H. Kerstein, A. Kitagawa, G. Lenderink, D. Lewellen, J. Mailhot, T. Mauritsen, V. Perov, G. Schayes, G.-J. Steeneveld, G. Svensson, P. Taylor, W. Weng, S. Wunsch, & Xu, K. M. (2006). Single-column model intercomparison for a stably stratified atmospheric boundary layer. *Boundary-Layer Meteorology*, *118*(2), 273-303.

Diamantakis, M., Wood, N., & Davies, T. (2006). An improved implicit predictor–corrector scheme for boundary layer vertical diffusion. *Quarterly Journal of the Royal Meteorological Society*, *132*(616), 959-978.

Dunbar, T. M., Hanert, E., & Hogan, R. J. (2008). A one-dimensional finite-element boundary-layer model with a vertical adaptive grid. *Boundary-layer meteorology*, *128*(3), 459-472.

Durran, D. R., & Blossey, P. N. (2012). Implicit-explicit multistep methods for fast-wave-slow-wave problems. *Monthly Weather Review*, *140*(4), 1307-1325.

Ferracina, L., & Spijker, M. N. (2008). Strong stability of singly-diagonally-implicit Runge–Kutta methods. *Applied Numerical Mathematics*, *58*(11), 1675-1686.

Franco, J. M., Gómez, I., & Rández, L. (2001). Four-stage symplectic and P-stable SDIRKN methods with dispersion of high order. *Numerical Algorithms*,*26*(4), 347-363.

Galperin, B., Kantha, L. H., Hassid, S., & Rosati, A. (1988). A quasi-equilibrium turbulent energy model for geophysical flows. *Journal of the Atmospheric Sciences*, *45*(1), 55-62.

Garratt, J. R. (1994). *The atmospheric boundary layer*. Cambridge university press.

Girard, C., & Delage, Y. (1990). Stable schemes for nonlinear vertical diffusion in atmospheric circulation models. *Monthly Weather Review*, *118*(3), 737-745.

Gottlieb, S., Ketcheson, D. I., & Shu, C. W. (2009). High order strong stability preserving time discretizations. *Journal of Scientific Computing*, *38*(3), 251-289.

Gourlay, A. R., & Morris, J. L. (1980). The extrapolation of first order methods for parabolic partial differential equations, II. *SIAM Journal on Numerical Analysis*, *17*(5), 641-655. Gourlay, A. R., & Morris, J. L. (1980). The extrapolation of first order methods for parabolic partial differential equations, II. *SIAM Journal on Numerical Analysis*, *17*(5), 641-655.

Griffiths, D. F., Stuart, A. M., & Yee, H. C. (1992). Numerical wave propagation in an advection equation with a nonlinear source term. *SIAM journal on numerical analysis*, *29*(5), 1244-1260.

Günther, M., Kvaernø, A., & Rentrop, P. (2001). Multirate partitioned Runge-Kutta methods. *BIT Numerical Mathematics*, *41*(3), 504-514.

Hairer, E., Nørsett, S. P., & Wanner, G. (1987). *Solving ordinary differential equations I. Nonstiff problems*. Springer-Verlag, Berlin.

Higueras, I. (2005). Representations of Runge--Kutta Methods and Strong Stability Preserving Methods. *SIAM journal on numerical analysis*, *43*(3), 924-948.

Hu, F. Q., Hussaini, M. Y., & Manthey, J. L. (1996). Low-dissipation and low-dispersion Runge–Kutta schemes for computational acoustics. *Journal of Computational Physics*, *124*(1), 177-191.

Hundsdorfer, W., & Verwer, J. G. (2003). *Numerical solution of time-dependent advection-diffusion-reaction equations* (Vol. 33). Springer.

Ixaru, L. G. (2012). Runge–Kutta method with equation dependent coefficients. *Computer Physics Communications*, *183*(1), 63-69.

Ixaru, L. G., & Berghe, G. V. (Eds.). (2004). *Exponential fitting* (Vol. 1). Springer.

Janisková, M., Thépaut, J. N., & Geleyn, J. F. (1999). Simplified and regular physical parameterizations for incremental four-dimensional variational assimilation. *Monthly weather review*, *127*(1), 26-45.

Kalnay, E., & Kanamitsu, M. (1988). Time schemes for strongly nonlinear damping equations. *Monthly weather review*, *116*(10), 1945-1958.

Kosovic, B., & Curry, J. A. (2000). A large eddy simulation study of a quasi-steady, stably stratified atmospheric boundary layer. *Journal of the atmospheric sciences*, *57*(8), 1052-1068.

Lele, S. K. (1992). Compact finite difference schemes with spectral-like resolution. *Journal of computational physics*, *103*(1), 16-42.

LeVeque, R. J. (2002). *Finite volume methods for hyperbolic problems* (Vol. 31). Cambridge university press.

Liu, C. H., & Leung, D. Y. C. (1998). Evaluation of an atmospheric boundary layer model used for air pollution studies. *Journal Of Applied Meteorology*,*37*(12), 1561-1576.

Mellor, G. L., & Yamada, T. (1974). A hierarchy of turbulence closure models for planetary boundary layers. *Journal of the Atmospheric Sciences*, *31*(7), 1791-1806.

Murray J. D. (1993). *Mathematical Biology*. Springer, p. 776.

Najafi-Yazdi, A., & Mongeau, L. (2013). A low-dispersion and low-dissipation implicit Runge–Kutta scheme. *Journal of computational physics*, *233*, 315-323.

Nazari, F., Mohammadian, A., & Charron, M. (2014). High-order low-dissipation low-dispersion implicit Runge-Kutta schemes. *Journal of computational physics*, Accepted.

Nazari, F., Mohammadian, A., Charron, M., & Zadra, A. (2014). Strongly stable schemes for nonlinear systems in atmospheric boundary layer, *Boundary-layer meteorology*, Under Review.

Nazari, F., Mohammadian, A., Zadra, A., & Charron, M. (2013). A stable and accurate scheme for nonlinear diffusion equations: Application to atmospheric boundary layer. *Journal of Computational Physics*, *236*, 271-288.

Nazari, F., Mohammadian, A., Charron, M., & Zadra, A. (2014). Optimal high-order diagonally-implicit Runge–Kutta schemes for nonlinear diffusive systems on atmospheric boundary layer. *Journal of Computational Physics*, *271*, 118-130.

Oran, E. S., & Boris, J. P. (2005). *Numerical simulation of reactive flow*. Cambridge University Press.

Pielke Sr, R. A. (2013). *Mesoscale meteorological modeling* (Vol. 98). Academic press.

Potter, D. Computational Physics, 1973, p. 300.

Poulos, G. S., Blumen, W., Fritts, D. C., Lundquist, J. K., Sun, J., Burns, S. P., ... & Jensen, M. (2002). CASES-99: A comprehensive investigation of the stable nocturnal boundary layer. *Bulletin of the American Meteorological Society*,*83*(4), 555-581.

Shu, C. W., & Osher, S. (1988). Efficient implementation of essentially non-oscillatory shock-capturing schemes. *Journal of Computational Physics*, *77*(2), 439-471.

Siebesma, A. P., Soares, P. M., & Teixeira, J. (2007). A combined eddy-diffusivity mass-flux approach for the convective boundary layer. *Journal of the atmospheric sciences*, *64*(4), 1230-1248.

Stanescu, D., & Habashi, W. G. (1998). 2N-Storage Low Dissipation and Dispersion Runge-Kutta Schemes for Computational Acoustics. *Journal of Computational Physics*, *143*(2), 674-681.

Staniforth, A., & Wood, N. (2008). Aspects of the dynamical core of a nonhydrostatic, deep-atmosphere, unified weather and climate-prediction model. *Journal of Computational Physics*, *227*(7), 3445-3464.

Steeneveld, G. J., Van de Wiel, B. J. H., & Holtslag, A. A. M. (2006). Modeling the evolution of the atmospheric boundary layer coupled to the land surface for three contrasting nights in CASES-99. *Journal of the atmospheric sciences*,*63*(3), 920-935.

Steeneveld, G. J. (2007). *Understanding and prediction of stable atmospheric boundary layers over land*. Wageningen Universiteit.

Stull, R. B. (1999). *An introduction to boundary layer meteorology* (Vol. 13). Springer.

Tam, C. K., & Webb, J. C. (1993). Dispersion-relation-preserving finite difference schemes for computational acoustics. *Journal of computational physics*, *107*(2), 262-281.

Teixeira, J., Reynolds, C. A., & Judd, K. (2007). Time step sensitivity of nonlinear atmospheric models: numerical convergence, truncation error growth, and ensemble design. *Journal of the atmospheric sciences*, *64*(1), 175-189.

Teixeira, J. (1999). Stable schemes for partial differential equations: the one-dimensional diffusion equation. *Journal of Computational Physics*, *153*(2), 403-417.

Verwer, J. G. (1996). Explicit Runge-Kutta methods for parabolic partial differential equations. *Applied Numerical Mathematics*, *22*(1), 359-379.

Williamson, D. L. (1996). Application of semi-lagrangian methods to climate simulation. *Proceedings on Semi-Lagrangian Methods, ECMWF, Reading, UK*, 167.

Wood, N., Diamantakis, M., & Staniforth, A. (2007). A monotonically-damping second-order-accurate unconditionally-stable numerical scheme for diffusion.*Quarterly Journal of the Royal Meteorological Society*, *133*(627), 1559-1573.